

TECHNISCHE UNIVERSITÄT MÜNCHEN
Lehrstuhl für Computation in Engineering

Full Waveform Inversion for Ultrasonic Nondestructive Testing

Robert Seidl

Vollständiger Abdruck der von der Ingenieurfacultät Bau Geo Umwelt der Technischen Universität München zur Erlangung des akademischen Grades eines

Doktors der Naturwissenschaften (Dr. rer. nat.)

genehmigten Dissertation.

Vorsitzender: Prof. Dr.-Ing. Kai-Uwe Bletzinger

Prüfer der Dissertation:

1. Prof. Dr. rer. nat. Ernst Rank
2. Prof. Dr. rer. nat. habil. Hans-Joachim Bungartz

Die Dissertation wurde am 26.09.2017 bei der Technischen Universität München eingereicht und durch die Ingenieurfacultät Bau Geo Umwelt am 18.12.2017 angenommen.

Abstract

In the field of ultrasonic nondestructive testing (US NDT), ultrasonic impulses are used to detect flaws in the quality of components without causing any damage. Based on performing experiments alone, it is possible to infer the state of the component – but recent methods usually provide only limited details on its interior damage and inhomogeneities concerning position, dimensions, form, or orientation. Furthermore, the number of sensors that can be applied to record the signals is restricted to merely a few due to the shape and dimensions of a typical specimen. In seismology, a wave-based technique, the so-called “full waveform inversion”, has been shown to generate high-resolution imaging of the earth’s interior from earthquake measurements. The fundamental idea of this dissertation is to combine field data from lab experiments with a wave speed model of an intact workpiece and to adapt the model in order to generate these experimental, sensory measurements. Formally, this is a nonlinear optimization problem, so the wave speed model is adapted in such a way that the discrepancy between the experimental measurements and the prognoses of the model output is minimized using gradient-based iterative optimization. Here, full wave equation modeling is performed at each iteration, while the adjoint sensitivity state method is used to efficiently calculate the gradient of the high-dimensional objective. To adapt the method to US NDT and to further enhance the imaging resolution, the actuator-sensor mode of common piezoelectric sensors is employed. The important question of this paper is: Can full waveform inversion be adapted to provide more information on the position, dimensions, and orientation of flaws in typical NDT settings? Furthermore, and more generally, can the imaging resolution be enhanced by putting more emphasis on the simulation model using full waveform inversion, as full wave equation modeling is performed at each iteration? In comparison to commonly employed methods, a simulation of the complete wave propagation in the workpiece is rather costly. This thesis shows that full waveform inversion naturally extends model-based US NDT methods, such as time reversal, and identifies them as an integral part of a mathematically rigorously formulated nonlinear optimization problem. The applicability of the method for US NDT is verified for the inspection of flawed structures, and is based on several examples. First, a flawed emulated aluminum plate will be investigated. Due to only a small number of sources and receivers available in typical US NDT applications, the number of sensors and sources needed for a successful identification of different flaws will be analyzed. Second, the visualization of reinforcement in concrete will be considered as an application in which an interior view of a solid is made possible by employing full waveform inversion. Third, the position, form, and depth of a drill into an aluminum plate with a manufactured defect will be reconstructed using guided ultrasonic waves, and thus the suitability of this method validated.

Zusammenfassung

Die zerstörungsfreie Prüfung (ZfP) mit Ultraschall erlaubt die Qualität eines Werkstücks zu testen, ohne es zu beschädigen. Sie ermöglicht die Untersuchung auf Schädigungen und Inhomogenitäten aller Art und dient dem Nachweis von Fehlern sowie der Bestimmung deren Lage, Form und Größe. Letzteres ist mit aktuellen Methoden nur bedingt möglich, weil beispielsweise die typischen Ausmaße von Proben oft nur eine geringe Anzahl an Sensoren zulassen. Um dieses Problem zu lösen, bietet es sich an auf ein bildgebendes Verfahren aus der Seismologie zurückzugreifen: die Full Waveform Inversion. Diese ist dazu in der Lage, anhand von Erdbebenmessungen hochauflösende Bilder des Inneren der Erde zu generieren. Die zugrundeliegende Idee ist es nun, dieses Verfahren auf die ZfP im Labor zu übertragen und auf diese Weise ein Simulationsmodell des intakten Werkstücks iterativ so anzupassen, sodass es möglich ist, die experimentellen Sensordaten zu rekonstruieren. Formal kann dies als nichtlineares Optimierungsproblem formuliert werden, in dem die Wellengeschwindigkeit im Simulationsmodell so korrigiert wird, dass der Unterschied zwischen dessen Prognosen und den experimentellen Messungen minimiert wird. Zur Lösung wird mit dem L-BFGS Verfahren ein iteratives gradienten-basiertes Verfahren verwendet, wobei in jeder Iteration der Gradient der hochdimensionalen Zielfunktion mittels der Methode des adjungierten Zustands durch zwei Vorwärtssimulationen bestimmt wird. Die vorliegende Dissertation untersucht, inwiefern die Methode der "Full Waveform Inversion" für den Einsatz in der ZfP mit Ultraschall angepasst werden muss, um die Bestimmung der Lage, Form und Größe von Schädigungen in Werkstücken zu erlauben. Im Vergleich zu bestehenden Methoden bleibt zu berücksichtigen, dass hierfür eine kostspielige Simulation der vollständigen Wellenausbreitung im Werkstück benötigt wird. In der Arbeit wird gezeigt, dass Full Waveform Inversion auf natürliche Weise modellbasierte ZfP-Methoden wie Time Reversal erweitert, indem sie diese als integralen Teil eines mathematisch sauber formulierten nichtlinearen Optimierungsproblems identifiziert. Ihre Anwendbarkeit für die ZfP wird an drei Fallbeispielen illustriert. Zuerst wird anhand einer beschädigten emulierten Aluminiumplatte analysiert, ob die typischerweise geringe Anzahl an Sensoren in der ZfP ausreicht, um die Lage, Form und Größe von unterschiedlichen Schädigungen zu bestimmen. Das zweite Beispiel widmet sich der Bewehrungsortung in Stahlbeton und damit dem Fall einer dreidimensionalen Inversion. Anschließend wird die Methode für den Einsatz in der ZfP prototypisch validiert, indem gezeigt wird, dass sie es erlaubt, die Lage, Form und Tiefe einer Bohrung in einer Aluminiumplatte mittels der ZfP mit geführten Wellen zu rekonstruieren.

Acknowledgments

First and foremost, I would like to thank my doctoral supervisor Prof. Ernst Rank for his continuous support, guidance and belief in my project. I also want to thank Prof. Hans-Joachim Bungartz for evaluating the thesis and being my second examiner as well as Prof. Kai-Uwe Bletzinger for chairing the exam of my doctoral thesis.

Many thanks go to all my colleagues at the Chair for Computation in Engineering and the Chair for Computational Modeling and Simulation.

This thesis would not exist without Hagen Wille, who started to examine Time Reversal for the detection of micro cracks in bones. The presentation of his first results and his enthusiasm motivated Prof. Rank and me to follow this direction of research. Furthermore, he also provided his FDTD code that was used as the starting point of our own investigations.

As this thesis turned out to be very interdisciplinary, I have to express deep gratitude to Prof. Christian Grosse and Katja Pinkert from the Chair for Non-destructive Testing for their interest in the topic and their close collaboration.

I am deeply grateful to Prof. Andreas Fichtner, who invited me to stay with his exceptional research group in Zurich and whom I always could turn to for help. I would also like to thank Christian Böhm, who dramatically improved my understanding of the method and supported me ever since. I can not stress enough how thankful I am to both of them and how important they were for the success of the thesis.

Furthermore, I was very fortunate to meet Prof. Zheng Fan and Jing Rao from Nanyang Technological University in Singapore at a NDT conference where they showed the first successful application of full waveform inversion for US NDT. I am very grateful that they agreed to share their lab data so that I could validate our Full Waveform Inversion code. My deep gratitude also goes to Jing Rao, who took a lot of time to describe their experiment in such detail that I could use their data for my validation.

Last, but definitely not least, I would like to thank my family for their ongoing support and belief in me.

Contents

1	Introduction	1
2	Model-based Ultrasonic Nondestructive Testing	11
2.1	The Acoustic Wave Equation	12
2.2	Numerical Solution	14
2.3	Time Reversal	18
2.4	Sensitivity kernel method	22
2.5	Summary	28
3	Full Waveform Inversion	31
3.1	Description as model-based NDT system	31
3.2	Nonlinear Optimization	33
3.2.1	Descent Methods	36
3.2.2	Summary	45
3.3	Efficient Computations - The Adjoint State Method	45
3.3.1	Adjoint state method	47
3.3.2	Adjoint sensitivity state method	55
3.3.3	Summary	59
3.4	Summary of the algorithm	60
4	Applications	63
4.1	Aluminumplate: Studies	63
4.1.1	Number of sensors	64
4.1.2	Number of sources	67
4.1.3	Source frequency	69
4.1.4	Source signal	70
4.1.5	Noisy flaw inference	71
4.1.6	Summary	72
4.2	Full Waveform Inversion for Solids	72
4.2.1	Numerical example	73
4.2.2	Reconstruction results	74
4.2.3	Summary	76
4.3	Validation experiments	77
4.3.1	Description of experiment	80
4.3.2	Reconstruction results	84
4.4	Summary	86

5 Conclusion and Outlook	87
5.1 Conclusion	87
5.2 Outlook	89
A Lagrangian Formulation	93
Bibliography	95

Chapter 1

Introduction

One aim of scientific computing is the simulation of functions that describe physical systems, such as the propagation of sound, heat, seismic or electromagnetic waves, or the deformation of a structure under loading. Here, media properties like density, wave speed, or heat and electrical conductivity as well as the initial state of the process under study are known. Problems of this type are called *direct* or *forward problems*. They start with the knowledge of causal factors of a physical system and then calculate its unique effects.

But not all problems are straightforward. On the contrary, often it is precisely the media properties that are unknown, and the goal is to obtain this information about the physical system from measurements only indirectly related to these quantities, i.e., by recording sound or measuring temperature or displacement at certain positions. These are *inverse problems* as they begin with the observation of a physical quantity (in an experiment) and try to find its causes. Therefore, it is the inverse of the classical direct problem as illustrated in Fig. 1.1. A famous example is Newton's determination of gravitation with Kepler's laws by describing the trajectories of planets. Here, the forward problem is concerned with the computation of the bodies' trajectories from the knowledge of forces, while the inverse problem focuses on determining these forces by observing the trajectories.

Other examples can be found in almost all scientific disciplines, and in particular, in optics, acoustics, medical imaging, computer vision, geophysics, astronomy, and nondestructive testing. More specific examples include the use of sonar or radar for the detection of objects, computed tomography (CT) scans, imaging of the Earth's subsurface from seismic measurements, and the

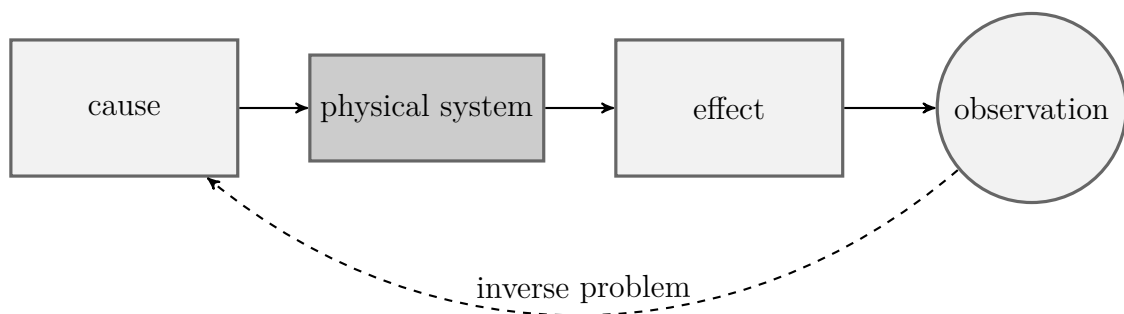


Figure 1.1: Principle of inverse problem

Physical system	Governing equations	Physical quantity	Observable data
Gravitational field	Newton's law of gravity	Density	Gravitational field
Temperature field	Heat equation	Heat conductivity	Temperature
Magnetic field	Maxwell's equations	Magnetic conductivity	Magnetic field
Seismic/Ultrasonic waves	Elastic wave equation	P- and S- wave speed ¹	Particle velocity
Seismic/Ultrasonic waves	Acoustic wave equation	P-wave speed ²	Pressure field

Table 1.1: Examples of inverse problems

design of light-weight structures. Table 1.1 displays examples of physical systems, governing equations, the physical quantity of interest and the observable data.

Most inverse problems cannot be solved analytically, and thus, iterative computational methods are essential for their solutions. The simulation of inverse problems has undergone a rapid growth due to an increase in computing power as well as progress in numerical modeling.

Adjoint methods are often used as a synonym for the solution of inverse problems because they are a necessary part of many iterative inversion schemes. Recently, there has been great interest in tackling inverse problems throughout all disciplines in Computational Science, Engineering and Finance (CSEF), which is well-documented in the increasing number of talks at scientific conferences. In the summary of a Dagstuhl seminar on *Adjoint Methods in Computational Science, Engineering and Finance* in 2014, the current status was described aptly³:

The human desire for meaningful numerical simulation of physical, chemical, biological, economical, financial (etc.) phenomena in CSEF has been increasing with the growing performance of the continuously improving computer systems. As a result of this development we are (and will always be) faced with a large (and growing) number of highly complex numerical simulation codes that run at the limit of the available high performance computing (HPC) resources. These codes often result from the discretization of systems of PDE. Their run time correlates with the spatial and temporal resolution which often needs to be very high in order to capture the real behavior of the underlying system. There is no doubt that the available hardware will always be used to the extreme. Improvements in the run time of the simulations need to be sought through research in numerical algorithms and their efficient implementation on HPC architectures. Problem sizes are often in the billions of unknowns; and with emerging large-scale computing systems,

¹speed of pressure and shear waves

²pressure wave speed

³<http://www.dagstuhl.de/de/programm/kalender/semhp/?semnr=14371>

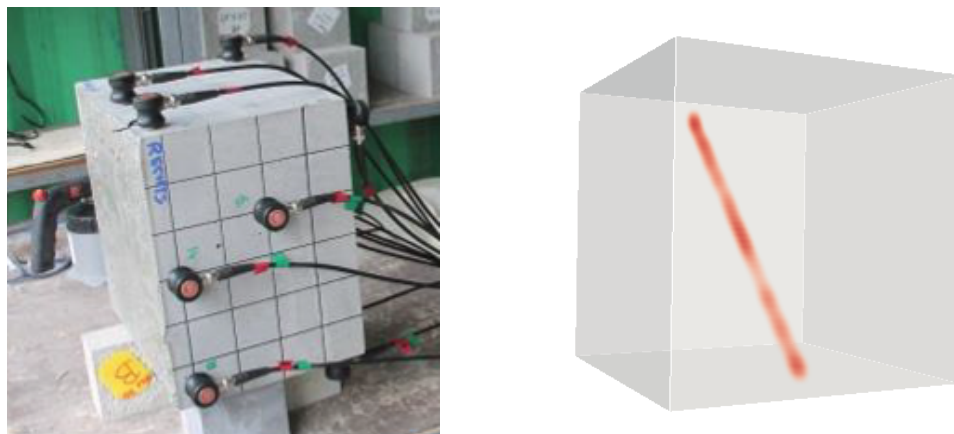


Figure 1.2: Illustration of US experiment in lab and result applying FWI

this size is expected to increase by a factor of thousand over the next five years. Moreover, simulations are increasingly used in design optimization and parameter identification which is even more complex and requires the highest possible computational performance and fundamental enabling algorithmic technology. [...]

In *all* scientific disciplines in CSEF there is a trend to tackle *large-scale inverse problems* because they arise naturally and their solution is of great value. The method proposed in this thesis – *full waveform inversion (FWI)* – also aims to solve a specific inverse problem. In the area of Nondestructive Testing (NDT), ultrasonic waves are used to inspect the interior of a structure for flaws or inclusions. Mechanical waves in the kHz to MHz range are employed to test mechanical structures for flaw sizes of mm to cm. NDT with ultrasound allows the inspection of simple structures like plates or blocks as well as more complex ones like pipes or airplane wings for internal damage without altering their physical properties. Fig. 1.2⁴ illustrates a typical NDT setup for US inspection in the lab. The goal is to generate a 3D model of the flawed interior of the block as shown on the right. The displacement of the block due to an applied ultrasonic source on the top is recorded with only a few sensors. These receiver signals carry information on the interior structure because the velocity of the traveling waves depends on the material, and reflections occur at the flaws and inclusions. The problem of reconstructing the material structure (or similarly, the wave speed) of the block from these measurements is formulated as an optimization problem. Here, the US wave propagation is described by a partial differential equation whereby the unknown material parameters are assumed to be spatially heterogeneous. For this test, the wave propagation is simulated on a computer. Depending on how fine the discretization of the material in the simulation model is tuned, this approach may lead to thousands or even millions of material parameters. For example, one for each grid point on a very fine three-dimensional grid, which has to be adapted simultaneously to solve the inverse problem. This seems to be a very audacious goal at first glance. The question is how is it possible to invert for thousands to billions of parameters simultaneously? How optimize a function in this very high-dimensional space efficiently? As it turns out, our inverse problem is formulated in a way that allows an efficient iterative solution. Instead of trying to solve it in one step, we will try to find a solution following small

⁴US experiment setup for block of concrete, Centre for Building Materials (cbm), Pasing, Munich

improvements. In fact, the iterative inversion approach tries to solve this problem step by step by decreasing the difference between the actual observations at the sensors from the lab and the predicted observations of our simulation model of the block.

$$J(m) = \frac{1}{2} \int_{\Omega} \int_0^T \sum_{i=1}^{N_s} [u(m; x, t) - u_0(x, t)]^2 \cdot \delta(x - x_i^r) dt dx,$$

where $u_0(x_i^r, t)$ is the observed ultrasonic signal for sensor at position x_i over the time period $[0, T]$, written using the Kronecker-Delta δ and $u(m; x, t)$ is the solution of the acoustic wave equation for a given material model $m(x) := v_p^2(x)$, $v_p(x)$ being the wavespeed at location x . The goal is to try to minimize the misfit $J(m)$ by adapting $m(x)$ in the simulation model. This way the model gets closer and closer to the desired output. The important factor is the gradient of the cost function. It tells us how we have to update the material model in the simulation to push the results of our model in the right direction.

That this simple iterative approach leads to the desired result is astonishing and not obvious at all. The key building block is the availability of the very high-dimensional gradient of our nonlinear objective function with respect to the material parameters for our large-scale optimization problem. This is made possible with what Andreas Griewank, the inventor of the “reverse mode” in computer science (Griewank, 2012), calls the **cheap gradient principle**. The renowned optimizer Phil Wolfe noted already in (Wolfe, 1982):

There is a common misconception that calculating a function of n variables and its gradient is about $(n + 1)$ times as expensive as just calculating the function. This will only be true if the gradient is evaluated by differencing function values or by some other emergency procedure. If care is taken in handling quantities, which are common to the function and its derivatives, the ratio is usually 1.5, not $(n + 1)$, whether the quantities are defined explicitly or implicitly, for example, the solutions of differential equations [...]

If the problem is formulated in the right way, gradient information is available at low cost. Of course, this does not hold in general, but a large number of interesting problems, such as the US inspection of specimen, can be formulated in such a manner that this principle is fulfilled. This is completely counterintuitive because a simple approximation of the cost function using finite differences would need at least $n + 1$ function evaluations. The cheap gradient principle leads to what Griewank effusively called the **holy grail of large-scale optimization** (Griewank, 2012):

If everything is organized correctly, the cheap gradient principle generalizes to what one might call the holy grail of large scale optimization, namely

$$\frac{\text{Cost}(\text{Optimization})}{\text{Cost}(\text{Simulation})} \approx \mathcal{O}(1)$$

By this we mean that the transition from merely simulating a complex system (by evaluating an appropriate numerical model) to optimizing a user specified objective (on the basis of the given model) does not lead to an increase in computational cost by orders of magnitude. Obviously, this is more a rule of thumb than a rigorous mathematical statement.

This principle allows us to tackle the material reconstruction problem in US NDT, although the costs of solving the wave propagation problem may be high. Interestingly, historical trends of solution methods for specific inverse problems can be traced back to various disciplines at the same time, such as computational fluid dynamics, shape optimization (Bletzinger et al., 2010; Bletzinger and Maute, 1997; Bletzinger and Ramm, 2014; Bletzinger et al., 2005; Gauger, 2002; Giles and Pierce, 1997; Newman III et al., 1999; Othmer, 2014; Pironneau, 1974), machine learning, seismology (Fichtner, 2011; Tarantola, 1984; Virieux and Operto, 2009), and predominantly the training of deep neural networks (Bishop, 2006; Martens, 2010; Pearlmutter, 1994; Rumelhart et al., 1986; Schraudolph, 2002).

The theoretical framework was already derived in the mid-80s of the last century, but could only be employed to solve unrealistic, simple toy problems. Nowadays, the increased computing power and storage as well as advances in numerical modeling permit tackling realistic inverse problems. An important research field is general computational imaging techniques, which have played an extensive role in many fields of science and engineering over the past decades. Just to name a few areas of application, modern medicine would not be imaginable without the tremendous progress in computed tomography systems; seismology gained important insight into the structure of the Earth thanks to computational imaging techniques; and nondestructive testing can process different types of signals with suitable reconstruction techniques to improve the quality control of materials and structures. The fields of application are as diverse as the computational methods developed over more than forty years. Some of the most important ones will be briefly discussed before turning to the more specific preliminary work in the field of nondestructive testing.

The technological evolution of imaging instrumentation and computerized signal analysis as well as image processing for medical purposes have increased the patient's chances of healing with early disease diagnosis and treatment evaluation (Brooks and Chiro, 1976; Dhawan, 2011). Continuous development of imaging instrumentation has, in turn, triggered a gradual transition towards automated scanning systems and multichannel sensor arrays to enable scanning and focused usage. The first medical computed tomography (CT), invented by Hounsfield in 1972 (Hounsfield, 1973), reconstructed three-dimensional tissue properties from two-dimensional measurements based on the filtered-backprojection of linearly propagated X-rays. Today, ongoing development of reconstruction algorithms for medical tomographic imaging is heading towards an iterative reconstruction that provides solutions for incomplete data set evaluation and minimizes artifacts (Buzug, 2008; Kunze, 2008). The overall advantages of these technological enhancements are the acceleration of the examination process — resulting in a reduction of the radiation dose for the human body — as well as the increase in spatial resolution and reduction of artifacts during image reconstruction. Two methods of examination are applied in medical, ray-based computed tomography (CT). Emission CT images the metabolism processes for functional diagnosis, determining the density of radioisotopes injected into the bloodstream beforehand. X-ray transmission CT, on the other hand, which serves to determine the distribution of attenuation coefficients and density of matters, images tissue morphology with high resolution (Brooks and Chiro, 1976; Dhawan, 2011). Previous to the evolution of imaging techniques for medical applications during the past century, the analysis of the Earth's structure was conducted by seismic tomography, based on the evaluation of seismic rays (mechanical waves). Stimulated by an excitation source, these rays are assumed to travel through a medium along straight lines. Structural

features were reconstructed by the filtered backprojection (based on the Radon transform), approximating high examination frequencies for poor scattering materials (Chapman, 1987). Numerous mathematical approaches have been taken and refined for seismic tomographic evaluation (Aki et al., 1977; Chen et al., 2007; Courboux et al., 1996; Dessa and Pascal, 2003; Husen and Kissling, 2001; Loris et al., 2007; Meier et al., 2007; van der Hilst and de Hoop, 2005). However, due to ray scattering at materials' inhomogeneities, highly nonlinear inverse problems (Dimri, 1992) have to be solved to reduce artifacts and, hence, to significantly improve the spatial resolution of structure evaluation. During the past two decades, full waveform inversion has gained a lot of interest in the field of seismology. It has been applied very successfully to identify the internal (material) structure of the Earth up to a degree that was not possible before (Afanasiev et al., 2016; Bunks et al., 1995; Fichtner, 2011; Virieux and Operto, 2009).

Since the late 1930s, the necessity of quality assurance, maintenance and process monitoring in civil and mechanical engineering has led to a focus on the development of nondestructive testing techniques for industrial applications (Burrascano et al., 2015; Karbhari, 2013; Meyendorf et al., 2004; Nakahata et al., 2015; Taffe et al., 2008; Zelenyak et al., 2016). NDT determines structural features (the material's composition and geometric characteristics) of the tested object without altering any of its physical and chemical properties. It offers a wide field of possible examination methods (Schiebold, 2015). The physicochemical properties of test materials determine the specific interaction of constructive structures with energies (response to initiating rays, waves or fields). Evaluating the NDT results requires a suitable analysis and presentation of the measured signals in order to quantify the material's composition and geometric characteristics of structures (Burrascano et al., 2015). Driven by the effectiveness and profitability of modern, lightweight structures that are comprised of complex, porous, layered and fiber-reinforced materials, a great demand for high-resolution 3D NDT imaging systems has emerged to ensure high quality during the production process as well as regarding service and maintenance (Karbhari, 2013; Meyendorf et al., 2004). In the field of NDT, it is necessary to improve these techniques to be able to image these physical systems.

Compared to high-resolution radiological NDT imaging (X-ray Transmission CT), ultrasonic (US) NDT imaging, which uses elastic waves, enables an adequate evaluation of structural features on a full scale and with regard to real constructions without the need for complex radiation protection, and serves as a basis for cheap and fast inspection processes. In order to develop new US NDT imaging systems for solid structures, the methodological progress gained in the field of seismology to solve inverse problems will be transferred and adapted accordingly. As FWI has proven to be a vital tool to inspect the composition of the Earth in seismology (Fichtner, 2011; Pratt et al., 1998; Virieux and Operto, 2009), we propose adapting the methodology of FWI on a smaller scale in a lab environment.

Most recently, there have been significant advances in applying FWI to both medical imaging and US NDT. In the former, Sandhu et al. use FWI for breast cancer imaging (Sandhu et al., 2015, 2016). They invert for wave speed, density and damping simultaneously. To model wave propagation, a 2D acoustic approximation was applied in the frequency domain and recently extended to 3D (Sandhu et al., 2017). This simple model is suitable for medical imaging of human tissue where the difference in wave speed between tissue and cancer cells is usually minimal. From a methodological point, a simple steepest descent method is applied for the

optimization.

As concerns US NDT, Rao et al. were possibly the first who successfully applied FWI to a problem in US NDT and validated their results with real data from their own lab experiments (Rao et al., 2016a,b, 2017). Similar to Sandhu, the wave equation is solved in frequency domain using a multiscale inversion and a 2D acoustic approximation that performs a large number of experiments.

The work in this thesis is different to both approaches in the following ways: 1) We do not use an approximation in frequency domain, but rather solve the wave equation directly in time domain by applying an explicit time stepping scheme of the finite-difference equations. The method to use is clearly problem dependent (Vigh and Starr, 2008). In general, using a single frequency, and therefore the frequency domain approach for the inversion, is equivalent to applying a sinusoidal source in time domain, and thus the time domain approach is the more general one. When a range of frequencies is used, the frequency domain method is equivalent to that of the time domain when using the same range of frequencies. The frequency domain approach is more efficient when many experiments with different source positions have to be performed. In the frequency domain approach, the acoustic wave equation is transformed into the Helmholtz equation for one frequency. Discretization leads to a large sparse linear equation system that can be solved cheaply for a large number of experiments after a LU decomposition has been computed. For 3D problems, this approach will possibly lead to huge memory requirements and preconditioned iterative solvers will have to be employed (Warner et al., 2008), too.

The general time domain approach uses all of the ‘wiggles’ in the data available for the reconstruction of the flaws, has significantly smaller memory requirements, and can be applied to 3D problems. One disadvantage is a significant computation time for the forward modelling, especially if the time increment of the explicit time-stepping scheme has to remain small. The cost for a simulation is approximately the same in every experiment, but this approach allows a simple, coarse-grain parallelism by distributing multiple experiments on multiple processors and then summing the results.

As described previously, the goal of this work is to investigate whether FWI is well-suited for imaging of flaws in US NDT applications, especially when only few sensor measurements are available. Therefore, we decided to model the wave propagation in time domain. Another important difference to both applications is that with L-BFGS, we use a very efficient, state-of-the-art gradient-based optimization scheme. This leads to far fewer function and gradient evaluations (and therefore, less expensive solutions of the wave equation) and faster convergence than simple steepest descent.

In addition, as our research did not start with FWI, our approach is also conceptually different. As illustrated in Fig. 1.3, we started by investigating the simple concept of experimental time reversal as introduced by Fink and Prada to locate flaws in structures. Inspired by the work of Leutenegger, Kocur and Givoli, we saw the potential to apply simulation methods for wave propagation for US NDT applications. The complexity of our approach was only increased when it was really necessary. As we were not able to automatically find the position and time of the waves’ scattering in time-reversed wavefields, we next investigated adjoint methods and

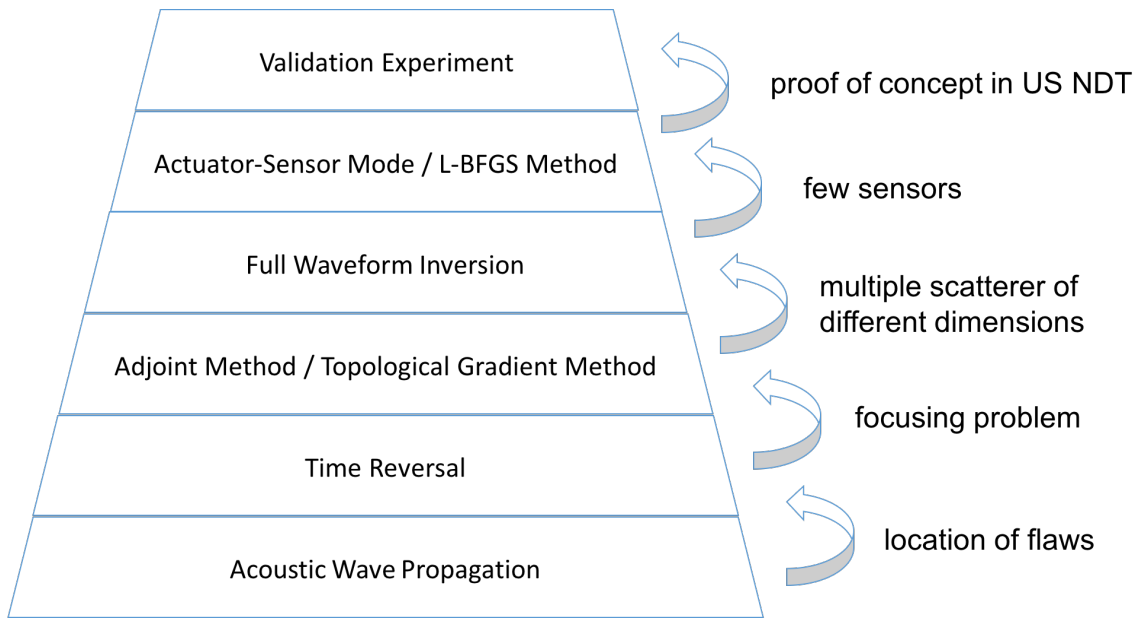


Figure 1.3: Conceptual overview

the topological energy method in US NDT. So, the lack of detecting multiple flaws of different dimensions led us to full waveform inversion. Unable to generate good results with only one experiment then caused us to exploit the actuator-sensor mode of piezo-electric sensors, while the rather slow convergence of the optimization resulted in an extension of simple gradient descent with the L-BFGS method. This finally allowed us to verify the applicability of the method for plate and solids as described in Sec. 4.1 and 4.2. The validation results of Rao et al. (Rao et al., 2016a), who used guided waves to derive the dimensions and depth of a drilled hole in an aluminum plate using only every fourth sensor measurement and experiment, were thereby extended.

The method proposed in this thesis has various advantages over other NDT systems as it

- evaluates the full ultrasonic wave signal and, thus, the maximal information available
- delivers a tomographic image and, as flaws are generally treated as deterioration of material parameters, allows for nondestructive testing
 - by identifying position, orientation and shape of flaws
 - by simultaneous detection of multiple flaws of different sizes
 - without prior knowledge of flaw occurrence or its specific characteristics
- is model-based, enabling easy incorporation of data from multiple NDT experiments, e.g. by
 - improving image quality by additional experiments
 - allowing measurements at different points in time without an enforcing a positioning of sensors at identical spatial coordinates.

The general complexity of the proposed approach is justified by the potential to fully automate the imaging of complex structures using US NDT, a major milestone for the quality assurance in civil and mechanical engineering.

In this thesis, full waveform inversion is proposed as a novel, model-based US NDT method that is based on a full numerical simulation of ultrasonic wave propagation. This method, which is extensively employed in exploration geophysics, should be adapted to the needs of US NDT. As full waveform inversion analyzes the entire signal, it may be able to provide more details about the shape and orientation of flaws and inclusions than common NDT methods. These details may then be used as input for procedures to predict an early failure of a structural component or to schedule necessary maintenance.

The goal of this thesis is to provide a first, prototypical implementation of full waveform inversion for US NDT. Importantly, after our concept has been proved and validated for US NDT, the method can be extended to a broader spectrum of NDT problems by considering the elastic wave equation as done previously in seismology.

The following research questions will be answered.

(1) Can full waveform inversion be employed to provide more information on the position, dimensions, and orientation of flaws than common, model-based US NDT methods by putting stronger emphasis on the simulation when full wave equation modeling is performed at each iteration? (2) Can the resolution of the imaging be enhanced by adapting the method to a typical NDT setup? (3) Can the method be validated for US NDT using experimental data?

The present work is organized as follows: this section, namely Chapter 1, **'Introduction'**, presents the topic of this thesis and outlines the major questions concerning US NDT methods. Chapter 2, **"Model-based Ultrasonic Nondestructive testing"**, provides an introduction to this testing technology. Classical ultrasonic NDT methods utilize only parts of the measured signals to decide if a specimen is flawed. In contrast, employing model-based NDT methods allows an exploitation of the entire signal information by performing a full numerical simulation of the wave propagation to reconstruct position, dimensions, and orientation of the flaws inside a specimen. Wave propagation is modeled by the acoustic wave equation. It is derived mathematically, and its numerical solution will be presented employing finite-differences. In order to do so, an explicit finite-difference time-domain method (which is fourth-order accurate in space and second-order accurate in time) will be formulated. Moreover, the conditional stability of the explicit time stepping scheme on the CFL condition will be discussed.

In the central part of this chapter, the Time Reversal Method will be presented as a well-known, model-based US NDT method that determines the origin of measured waves by playing them backward. Computational time reversal, where the backpropagation of measurements is performed numerically, suffers from the fact that the area and time of refocusing of the backplayed wavefield cannot be easily determined. As one possible solution, the sensitivity kernel method will be introduced. It solves the problem of refocusing with a clever combination of the time reversal wave field and the simulated forward wave field of the unflawed specimen.

In Chapter 3, **"Full Waveform Inversion for Ultrasonic Nondestructive Testing"**, full waveform inversion is presented as a novel, model-based NDT method. It exploits the complete waveform to iteratively reconstruct the velocity model of the flawed specimen. Mathematically,

the problem is posed as a nonlinear optimization of the least-squares misfit of experimental and simulated data with the acoustic wave equation as the constraint. A gradient-based optimization is applied to solve this problem iteratively. To provide the gradient information of the high-dimensional objective, the adjoint sensitivity state method will be taken into account. The basics necessary for nonlinear optimization will be summarized, the L-BFGS method described for the iterative minimization, and full waveform inversion formulated for US NDT.

Chapter 4, "**Applications**", verifies the applicability of full waveform inversion for two- and three-dimensional problems of a simulated aluminum plate and reinforced concrete. A study on the influence of the positioning and the necessary number of sensors and source characteristics of the attainable resolution will be performed. Finally, a first successful validation of full waveform inversion for US NDT using experimental data will be accomplished by reconstructing the thickness of an aluminum plate with a drilled hole.

Chapter 5, "**Conclusion And Outlook**", summarizes the results of this thesis and presents some possible improvements and further possibilities for research.

Chapter 2

Model-based Ultrasonic Nondestructive Testing

Nondestructive testing (NDT) consists of a wide range of analysis techniques that evaluate properties of material or structural components without altering the inspected specimen. They are routinely applied in industries where a failure of a component would cause severe damage. Here, damage is defined as a change in either material or geometric properties of the specimen and the goal is the extraction of damage-sensitive features from measurements. Application areas are weld verification, radiography in medicine or structural mechanics. In the latter a controlled pulse is applied to a structure and displacements or accelerations are measured at different sensor locations. Then, the observed output is compared to the expected output of a healthy structure. Thus, differences in outputs may indicate an inappropriate model or failed component. In general, a wide range of methods from different fields are employed including radiological, electrical, magnetic, and ultrasonic methods. Typical examples are X-ray tomography, thermography, eddy current or ultrasonic testing. An overview of different methods is given in (Blitz and Simpson, 1996; Drinkwater and Wilcox, 2006; Liu et al., 2008). Test specimen can range from homogeneous to strongly inhomogeneous structures consisting of carbon-fiber-reinforced polymer (CRFP) or fiber composites.

The most widely used testing method is ultrasonic NDT. It is based on the propagation of low amplitude waves through the material, measuring travel time and intensity of the waves at specific sensors. In principle, flaws and other discontinuities hidden in the structure produce reflective interfaces and can thus be detected using ultrasonic NDT. It is often utilized to inspect steel, metal or alloy components and, less often, to investigate wood, concrete or composites (Carlson and Johnson, 1992; Kumar et al., 2003; Prassianakis and Prassianakis, 2004; Sandoz et al., 2000). Commonly used frequencies of applied pulses range from 0.1 - 20 MHz resulting in wavelengths of centimeter to millimeter. The main advantage of US NDT is that it is suitable to detect flaws deep inside the specimen. Further, it serves to estimate the size, orientation and shape of defects.

The conventional analysis of NDT results is comprised of specific US wave signal parameters extracted from transmitted or reflected wave signals to plot point, line or area scan results (A-scan, B-scan, C-scan) (Krautkrämer and Krautkrämer, 1983).

Testing of a general volume (3D) will yield projected 2D results and the manual comparison of signal parameters to reference measurements of a "flawless specimen" is employed to detect flaws as illustrated in Fig. 2.1.

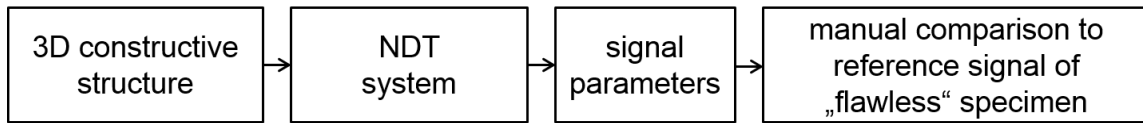


Figure 2.1: Conventional US NDT result (manual signal comparison)

To quantify the dimension and geometry of internal flaws and therefore evaluate US-NDT results a numerical comparison of signal characteristics of measured and simulated signals is made. We refer to this as simulation-model-based or simply model-based NDT. Assuming that the wavelength of the source is much smaller than the anomaly or defect, the propagation of waves through a medium can be approximated as propagation of wave packets along definite paths called "rays" similar to light rays in geometrical optics. Ray theory is based on the high frequency assumption that the propagating wave is a spike (Bleistein et al., 2001). In this case, neglecting amplitude and phase information, only arrival times of US waves are considered to construct a velocity estimate for the specimen. Well known model-based NDT methods like SIRT and ART are popular examples of ray-based methods (Liu et al., 2008; Ohtsu, 2016; Oliveira et al., 2011).

In the common NDT setting where only a few sensor measurements are available, neglecting amplitude and phase information severely limits the accuracy of the inspection. More importantly, the description of wave propagation as rays is no longer valid when some velocity features behave more like scatterers than a simple refracting surface element which is true in many NDT applications. When the wavelength of the source is similar to the anomaly that should be detected, small scatterers produce secondary wave fields and a simple description of the propagation as rays is not valid any more. In these situations using the full wavefront is necessary.

This amounts to a full numerical simulation of the wave propagation in the medium which is described by the elastic or acoustic wave equation. Its numerical solution for realistic problems only became possible recently due to improved performance of computer systems. The acoustic wave equation and its numerical solution are described next.

2.1 The Acoustic Wave Equation

The propagation of sound through an elastic medium is described by the elastic wave equation. Ultrasound can be used to explore the physical condition of an object made of linear elastic material. All sorts of waves can be used to inspect objects but longitudinal waves are most important from an NDT point of view because they are the only waves propagating in gas and liquids and are the fastest propagating waves in elastic media (Krautkrämer and Krautkrämer, 1983). Here, oscillations occur only in longitudinal direction, that is the direction of propagation. They are also called compression, pressure or P-waves. For determining the propagation of pressure waves in an elastic medium, the simpler acoustic wave equation can be used as approximation. Even though, in general, it only describes the phenomenon of mechanical vibrations and their propagation in liquid and gaseous materials, it is appropriate

for elastic solids when the data is restricted to the first-arriving P-waves. Consequences of this simplification are the absence of waves that travel along the surface of solids, known as Raleigh waves, in the model which are frequently used in NDT for detecting defects. Additionally, when a P-wave hits an interface, e.g. between solid and liquid, it can be reflected as a S-wave. This P-to-S conversion is ignored in the simple model. Despite these issues, seismologists have modeled the earth as fluid medium with variable parameters instead of an elastic medium to reduce computational cost (Bleistein et al., 2001) for a long time. As the acoustic wave equation is a scalar equation it leads to less memory requirements and runtime than the elastic wave equation, which is a vector equation.

Following (Claerbout, 1985) the acoustic wave equation is derived from Newton's law of momentum conservation.

Newton's law of momentum conservation states that a small volume within a fluid will accelerate if there is an applied force. The force arises from pressure differences at opposite sides of the small volume. Exemplary considering only one dimension, this yields:

$$\rho \frac{\partial u}{\partial t} = -\frac{\partial P}{\partial x}. \quad (2.1)$$

Here, ρ describes the density of the fluid, u the velocity flow of the fluid in the x -direction and P its pressure. If the small volume between x and $x + \Delta x$ is expanding it must lead to a pressure drop. The amount of the pressure drop is in proportion to the incompressibility K of the fluid. In one dimension the equation is

$$-\frac{\partial P}{\partial t} = K \frac{\partial u}{\partial x}. \quad (2.2)$$

In multiple dimensions $\frac{\partial u}{\partial x}$ is replaced by the divergence $\nabla \cdot u$.

Deriving Eq. 2.1 with respect to x yields:

$$\frac{\partial}{\partial x} \frac{\partial}{\partial t} u = -\frac{\partial}{\partial x} \frac{1}{\rho} \frac{\partial P}{\partial x}. \quad (2.3)$$

Deriving Eq. 2.2 with respect to t gives:

$$\frac{\partial^2 P}{\partial^2 t} = -K \frac{\partial}{\partial t} \frac{\partial}{\partial x} u. \quad (2.4)$$

Inserting Eq. 2.3 into 2.4 yields the scalar acoustic wave equation:

$$\frac{\partial^2 P}{\partial^2 t} = K \frac{\partial}{\partial x} \frac{1}{\rho} \frac{\partial P}{\partial x}. \quad (2.5)$$

Now, assuming that ρ varies much more slowly than the pressure field P , this expression can be further simplified to

$$\frac{\partial^2 P}{\partial^2 t} = \frac{K}{\rho} \left(\frac{\partial^2 P}{\partial^2 x} \right). \quad (2.6)$$

In three dimensions, a similar derivation shows:

$$\frac{\partial^2 P}{\partial^2 t} = \frac{K}{\rho} \Delta P, \quad (2.7)$$

or

$$\frac{\partial^2 P}{\partial t^2} = v_p^2 \Delta P, \quad (2.8)$$

where $v_p = \sqrt{\frac{K}{\rho}}$ is the wave speed of the pressure wave. This shows that wave motion in fluids can be described by a scalar field P . The acoustic wave equation is extended by initial and boundary conditions and an inhomogeneous source term $f_s(x, t)$. Furthermore, the variable u is used to describe the pressure field P to be concise with literature, where u is identified as general state variable.

To summarize, the acoustic wave equation is used to model the propagation of compression waves in the medium with a spatially variable wave speed $v_p(x)$.

$$u_{tt}(x, t) - v_p^2(x) \Delta u(x, t) = f_s(x, t) \text{ for } x \in \Omega \subset \mathbb{R}^2 \text{ or } \mathbb{R}^3, t \in [0, T] \quad (2.9a)$$

$$u(x, 0) = u_t(x, 0) = 0, \text{ on } \Omega \quad (2.9b)$$

$$u = 0 \text{ on } \partial\Omega \quad (2.9c)$$

Equation 2.9 describes the pressure field u induced by an applied ultrasonic impulse f_s in a two- or three-dimensional domain Ω for a time span of T microseconds. All boundaries are assumed to be rigid. Impulse f_s is modeled as a point source, $f_s = A(t) \cdot \delta(x - x_s)$, where x_s is the source position and $A(t)$ the time-varying excitation.

As analytical solutions to the acoustic wave equation exist only for simple models, numerical methods have to be employed for the simulation of wave propagation. The simplest method is based on finite-differences and is introduced next.

2.2 Numerical Solution

The commonly applied numerical methods can be divided into finite-difference, finite element and finite volume methods. The finite-difference method is the most frequently used method for the numerical simulation of wave propagation in geophysics (Fichtner, 2011). This is due to the ease of its implementation and its easy understanding. It is often utilized for a prototypical implementation. As already discussed in Sec.1, we follow this approach in this thesis. However, it is important to note that finite-differences are clearly not limited to simple problems as they are also applied to solve demanding large-scale 3D wave propagation problems (Etgen and O'Brien, 2007).

The principle of finite-difference approximations is presented first following (LeVeque, 2007) and then applied to the scalar wave equation to derive the finite-difference time-domain (FDTD) method. For the mathematical treatment of finite-differences see (Durrant, 1999). A good introduction into finite-difference modeling of earthquakes can be found in (Moczo et al., 2014).

Spatial discretization

The finite-difference method solves a PDE by approximating its solution on a finite set of grid points. For this, derivatives in the differential equation are discretized by finite-difference equations that depend on the knowledge of function values at neighboring grid points. We

restrict ourselves to a uniform partition in both, space and time. As example, a one-dimensional domain in space is discretized using a spatial x_0, \dots, x_I and temporal mesh t_0, \dots, t_N , where

$$x_i = x_0 + i \cdot h, \quad i = 0, \dots, I \quad (2.10)$$

$$t_n = t_0 + n \cdot k, \quad n = 0, \dots, N \quad (2.11)$$

Thus, x_{i-1} and x_{i+1} denote the left and right neighbor of grid point x_i , respectively. The numerical approximation of the solution at grid points is represented by

$$u_i^n := u(x_i, t_n). \quad (2.12)$$

Assuming that the solution u of the one-dimensional wave equation is sufficiently smooth, and disregarding its temporal dependence for the moment, a Taylor series expansion about a point x leads to:

$$u_{i+1} = u_i + h \frac{\partial u}{\partial x} + \frac{h^2}{2} \frac{\partial^2 u}{\partial x^2} + \frac{h^3}{6} \frac{\partial^3 u}{\partial x^3} + O(h^4), \quad (2.13)$$

and

$$u_{i-1} = u_i - h \frac{\partial u}{\partial x} + \frac{h^2}{2} \frac{\partial^2 u}{\partial x^2} - \frac{h^3}{6} \frac{\partial^3 u}{\partial x^3} + O(h^4). \quad (2.14)$$

Using Eq. 2.13 and 2.14, the second derivative of u is approximated by

$$\left(\frac{d^2 u}{dx^2} \right)_i^{\text{central},2} = \frac{u_{i+1} - 2u_i + u_{i-1}}{h^2}, \quad (2.15)$$

with accuracy up to $O(h^2)$. The subindex i indicates that the derivative is evaluated at position x_i and the superscript indicates that it is approximated with central differences of order $O(h^2)$. Especially in the case of wave propagation problems where smooth pulses with small support are propagated, it is important to have an accurate spatial approximation. An important high-order approximation of the second derivative is

$$\left(\frac{d^2 u}{dx^2} \right)_i^{\text{central},4} = \frac{-u_{i+2} + 16u_{i+1} - 30u_i + 16u_{i-1} - u_{i-2}}{12h^2}. \quad (2.16)$$

Here, the difference equation incorporates not only information of the neighboring grid points but also of grid points further away to increase the approximation order to $O(h^4)$. Finite difference formulas of arbitrary approximation order can be created employing the method of undetermined variables (LeVeque, 2007).

The extension of finite differences to two and three dimensions is straight-forward. If the function value u at grid position (x_i, x_j, x_k) in 3D is denoted by $u_{i,j,k}$ then the discrete finite-difference approximation in direction j at position i, j, k can be written for an equidistant grid as

$$\left(\frac{d^2 u}{dx_j^2} \right)_{i,j,k}^{\text{central},4} = \frac{-u_{i,j+2,k} + 16u_{i,j+1,k} - 30u_{i,j,k} + 16u_{i,j-1,k} - u_{i,j-2,k}}{12h^2}. \quad (2.17)$$

Therefore, approximating the Laplacian Δu in Eq. 2.9 yields

$$\frac{\partial^2 u}{\partial t^2} - v_{i,j,k}^2 \cdot \left[\left(\frac{d^2 u}{dx_i^2} \right)_{i,j,k}^{\text{central},4} + \left(\frac{d^2 u}{dx_j^2} \right)_{i,j,k}^{\text{central},4} + \left(\frac{d^2 u}{dx_k^2} \right)_{i,j,k}^{\text{central},4} \right] = f_{i,j,k}. \quad (2.18)$$

The next step is a temporal discretization of the acoustic wave equation.

Time discretization

The application of any space discretization method to the semi-discretized wave equation 2.18 results in a system of ordinary differential equations (ODEs) that can be formulated compactly as

$$\mathbf{M} \frac{d^2 \mathbf{u}(t)}{dt^2} + \mathbf{K} \mathbf{u}(t) = \mathbf{f}(t), \quad (2.19)$$

where \mathbf{M} and \mathbf{K} are the mass and stiffness matrix, respectively. The vectors \mathbf{u} and \mathbf{f} are composed of all coefficients $u_{i,j,k}$ and $f_{i,j,k}$, respectively.

It is of tremendous importance for an efficient solution that \mathbf{M} is easily invertible. For the explicit finite-difference discretization 2.18, \mathbf{M} is the identity matrix. Furthermore, note that both matrices are not set up in actual codes as only their matrix-vector products are needed when applying explicit methods. Dropping the explicit dependence on time t ,

$$\frac{d^2 \mathbf{u}}{dt^2} = \mathbf{M}^{-1} [\mathbf{f} - \mathbf{K} \mathbf{u}]. \quad (2.20)$$

A straight-forward approach is to also apply second-order central differences for the time discretization. This leads to

$$\frac{\mathbf{u}^{n+1} - 2\mathbf{u}^n + \mathbf{u}^{n-1}}{k^2} = \mathbf{M}^{-1} [\mathbf{f} - \mathbf{K} \mathbf{u}^n]. \quad (2.21)$$

Thus, the final dynamic evolution equation is given by

$$\mathbf{u}^{n+1} = 2\mathbf{u}^n - \mathbf{u}^{n-1} + k^2 \mathbf{M}^{-1} [\mathbf{f} - \mathbf{K} \mathbf{u}^n]. \quad (2.22)$$

Here, the wave field at time $t + k$ depends only on information at prior time steps. If the solution is initialized at consecutive time steps $\mathbf{u}^0, \mathbf{u}^{-1}$, this information is used to compute the wave field for the next time step \mathbf{u}^1 . This process is iterated until the desired final time T is reached.

Alternatively, other well known low-order time integration schemes like Newmark or the leap-frog scheme are often employed, especially for spectral or finite elements (Peter et al., 2011; Tromp et al., 2008).

Stability

For every numerical method for transient problems it is important to investigate how errors made at one time step in the calculation affect the numerical solution. In the end, the asymptotic behavior of the numerical and analytical solution should agree. For this a *von Neumann analysis* (VonNeumann and Richtmyer, 1950) of the finite difference scheme is performed. For the analysis we follow (Igel, 2016) and investigate the one-dimensional acoustic wave equation with a second-order central finite-difference approximation in space and time. Extending the method to more general finite-difference schemes and higher dimensions is straight-forward.

We start by recalling the one-dimensional source-free acoustic wave equation with constant wave speed v_p :

$$u_{tt} - v_p^2 \cdot u_{xx} = 0. \quad (2.23)$$

Using a spatial mesh $0, \dots, x_I$ and temporal mesh $0, \dots, t_N$, where

$$x_i = i \cdot dx, \quad i = 0, \dots, I \quad (2.24)$$

$$t_n = n \cdot dt, \quad n = 0, \dots, N \quad (2.25)$$

let us formulate the finite-difference solution at grid points by

$$u_i^n := u(x_i, t_n). \quad (2.26)$$

Applying second-order central finite-differences in space and time leads to

$$u_i^{n+1} - 2u_i^n + u_i^{n-1} = v_p^2 \frac{dt^2}{dx^2} [u_{i+1}^n - 2u_i^n + u_{i-1}^n]. \quad (2.27)$$

The analytical solution of the source-free acoustic wave equation is given by a plane harmonic wave for pressure u propagating in x -direction with wavenumber k and angular frequency ω

$$u(x, t) = e^{j(kx - \omega t)}. \quad (2.28)$$

Here, $j = \sqrt{-1}$ is the imaginary unit. Plugging in the analytical solution in the finite-difference approximation 2.27, we will use:

$$u_i^n = e^{j(kix - \omega ndt)}, \quad (2.29)$$

$$u_{i+1}^n = e^{j(k(i+1)dx - \omega ndt)}, \quad (2.30)$$

$$= e^{jkdx} u_i^n, \quad (2.31)$$

$$u_i^{n+1} = e^{-j\omega dt} u_i^n. \quad (2.32)$$

$$(2.33)$$

Replacing all terms in Eq. 2.27 by above formulas and dividing by u_i^n on both sides yields

$$e^{j\omega dt} + e^{-j\omega dt} - 2 = v_p^2 \frac{dt^2}{dx^2} (e^{jkdx} - e^{-jkdx} - 2). \quad (2.34)$$

Applying the expression for $\cos x$ in terms of exponential functions

$$\cos x = \frac{1}{2}(e^{jx} + e^{-jx}) \quad (2.35)$$

results in

$$\cos(\omega dt) - 1 = v_p^2 \frac{dt^2}{dx^2} (\cos(kdx) - 1). \quad (2.36)$$

Finally, applying

$$\sin \frac{x}{2} = \pm \sqrt{\frac{1 - \cos x}{2}} \quad (2.37)$$

yields

$$\sin\left(\omega \frac{dt}{2}\right) = v_p \frac{dt}{dx} \sin\left(k \frac{dx}{2}\right). \quad (2.38)$$

The equation has only real solutions when

$$\epsilon = v_p \frac{dt}{dx} \leq 1. \quad (2.39)$$

where $0 < \epsilon < 1$ is called the CFL¹ number. It depends on both, the numerical scheme and the spatial dimension of the problem. Solving for the timestep size yields the CFL condition.

$$dt \leq \epsilon \cdot \frac{dx}{v_p}, \quad (2.40)$$

It limits the maximal time step for a stable numerical simulation, and therefore the efficiency of any explicit method. As consequence the space-time discretization can not be arbitrarily chosen but depends on the medium properties. The space discretization is often chosen by the smallest wave speed in the medium. The CFL condition determines the time step dt and therefore the number of time steps necessary to achieve a certain simulation length.

A second important requirement simulating the propagation of waves is that the number of grid points per shortest wavelength is large enough to achieve accurate solutions. The exact number is problem dependent but often in a range of 10 – 20 points per dominant wave length (Igel, 2016). For small US pulses this results in a fine spatial discretization and consequently also in a fine time discretization.

As mentioned in (Fichtner, 2011), it is remarkable that explicit low-order time integration schemes work so well for wave propagation problems and commonly no high-order and implicit schemes like Runge-Kutta or predictor corrector methods are employed for seismic simulations. It has been shown empirically that this is due to the numerical error being dominated by the spatial discretization error and not the time integration.

The next section describes how a full numerical simulation of wave propagation employing the acoustic wave equation can be used to inspect workpieces.

2.3 Time Reversal

As discussed before, simple ray-theoretical models only use the arrival times of the recorded waves to estimate the velocity inside a specimen. Clearly, there exists a lot more information about the geometry in a waveform signal than in its arrival time and using the full waveform to inspect the specimen is desirable. For this, a numerical solution of the wave equation is necessary.

Mathias Fink, a pioneer in time-reversed acoustics, showed that US waves can be used to locate US sources by measuring waves and sending them back to their origin as if time has been reversed (Fink, 1992, 1997, 1999; Fink et al., 2000). This is possible due to the time reversal invariance of the wave equation that describes the propagation of waves in a medium. As illustration, suppose one excites an US source and measures the pressure field $p(r_s, t)$ on a surface around it. When the time-reversed signals $p(r_s, T - t)$ are re-emitted on the surface in a first-in last-out fashion, the emitted waves seem to propagate backwards in time and the resulting wave field converges back to its initial source. This focusing occurs on a spot whose dimensions are on the order of the smallest wavelength of the source. The procedure, called *time reversal* (TR), can be used to detect active sources as well as passive sources like scatterers.

¹named after Richard Courant, Kurt Friedrichs and Hans Lewy (Courant et al., 1928)

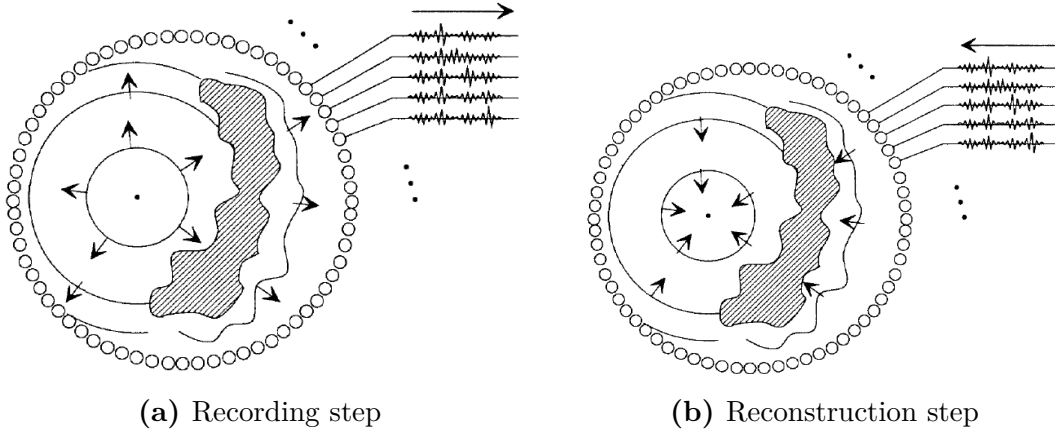


Figure 2.2: Two step process of time reversal method, from Fink (1992)

From a mathematical point of view being able to backpropagate waves is possible because the wave equation contains only second-order derivatives in time and therefore is time reversal invariant. To see this, recall the finite-difference approximation of the acoustic wave equation in Eq. 2.27 for advancing one step in time $t_n \rightarrow t_n + dt$:

$$u_i(t_n + dt) = 2u_i(t_n) - u_i(t_n - dt) + v_p^2 dt^2 \Delta_h u_i(t_n), \quad (2.41)$$

where $\Delta_h u_i(t_n) = \frac{u_{i+1}(t_n) - 2u_i(t_n) + u_{i-1}(t_n)}{dx^2}$ is an approximation of the Laplacian $\Delta u_i(t_n)$. Now, instead of advancing one time step, consider going back one step in time from t_n to $t_n - dt$. Then,

$$u_i(t_n + (-dt)) = 2u_i(t_n + (-dt)) - u_i(t_n - (-dt)) + v_p^2 \frac{(-dt)^2}{dx^2} \Delta_h u_i(t_n) \quad (2.42)$$

$$= 2u_i(t_n - dt) - u_i(t_n + dt) + v_p^2 \frac{dt^2}{dx^2} \Delta_h u_i(t_n). \quad (2.43)$$

Comparing this equation to Eq. 2.41, this shows that the same dynamic equation can be used to propagate acoustic waves forward and backward in time. (Assuming that the medium is non-dissipative). A more rigorous proof involves the self-adjointness of the acoustic wave equation operator as discussed in Sec. 3.3.1

There exist extensive application areas where this concept can be applied including source detection, scatterers and obstacle identification, damage identification in structures, undersurface geophysical structure identification and pulse-echo detection, where the goal is to detect and image passive reflective targets, (Ammari et al., 2013; Chen et al., 2013; Deneuve et al., 2010; Tromp et al., 2004).

In acoustics, piezo-electric transducers combine the function of microphone and loudspeaker and can therefore be used in TR. Some recent applications in NDT are time reversal employing Lamb waves, the inspection of composite plates, structural concrete and reinforced concrete beams (Kocur, 2012; Kocur et al., 2015; Park et al., 2007; Xu and Giurgiutiu, 2007).

Ultrasonic time reversal is a two-step process:

1. *Recording step.* An ultrasonic source emits a wave front that propagates through the medium, is possibly distorted, and transducers detect the arriving waves.

2. *Reconstruction step.* Each measurement point acts as point source with corresponding excitation signal. All transducers excite the structure simultaneously, playing back the signals in reverse, in a first-in last-out fashion. The original wave is recreated traveling backward.

Following this approach, the reversibility property of wave propagation allows to determine the origin of a wave front. The process is illustrated in Fig. 2.2 from (Fink, 1992). In the recording step, a point-like source generates a wave front that is distorted by heterogeneities. The pressure field is recorded at the receivers indicated by circles. In the reconstruction step, the recorded signals are time-reversed and re-emitted at the sensor locations. The time-reversed pressure field propagates back in the medium and refocusing occurs at the time and location where the wave field was excited.

The process can be utilized not only to detect active sources like explosions or earthquakes but also to detect unknown scatterers. This is possible because scatterers act as secondary sources. If a wave field reaches a scattering object part of the wave will be reflected. If these reflected waves are recorded at some sensors time reversal can be applied to find the positions of the scatterers.

The work of Fink focuses on *experimental time reversal*. The time-reversed waves are re-emitted back into the experimental structure in the lab. One problem with this approach is that one has to have already a good idea where and when the focusing occurs. With no prior information the complete structure has to be scanned to determine the peak amplitude position. This can be a very tedious task or even impossible when the focusing occurs inside a 3D solid.

As the reversibility of waves is not limited to physical experiments, the TR method was recently adapted by substituting the wave backpropagation in the experiment with a simulation model. This approach, called *computational time reversal* (CTR), is used in mechanics as a computational tool for scatterers detection (Amitt et al., 2014; Givoli, 2014; Givoli and Turkel, 2012) and in seismology for source identification (Kremers et al., 2011; Larmat et al., 2010). One advantage of CTR over experimental TR is that the backpropagated wave field is known not only at certain sensor locations but everywhere in the domain and therefore it is possible to find the spot of refocusing even inside a 3D specimen.

Leutenegger was possibly the first who used CTR in NDT to determine the presence of a defect and its exact position in a cylindrical structure (Leutenegger and Dual, 2002). He showed that it is possible to simulate the reverse wave propagation numerically. This is possible if the simulated structure has the same geometry, material parameters and boundary conditions as the sample used in the experiment. Additionally, the physics of the wave propagation have to be described appropriately by the simulation. Signals from the physical experiment are recorded by transducers and numerically re-emitted as source in a time-reversed manner.

In the case of acoustic waves, the time reversal problem is described by the following PDE:

$$u_{tt}^{\text{TR}}(x, t) - v_p^2(x)\Delta u^{\text{TR}}(x, t) = \sum_{i=1}^N u_0(x_i^r, T - t) \text{ for } x \in \Omega, t \in [0, T] \quad (2.44a)$$

$$u^{\text{TR}}(x, 0) = u_t^{\text{TR}}(x, 0) = 0, \text{ on } \Omega \quad (2.44b)$$

$$u^{\text{TR}} = 0 \text{ on } \partial\Omega \quad (2.44c)$$

Here, u^{TR} describes the back-propagation of the US impulses in the domain $\Omega \subset \mathbb{R}^3$ and v_p is the speed of the pressure waves in the material. The US source is built as a superposition

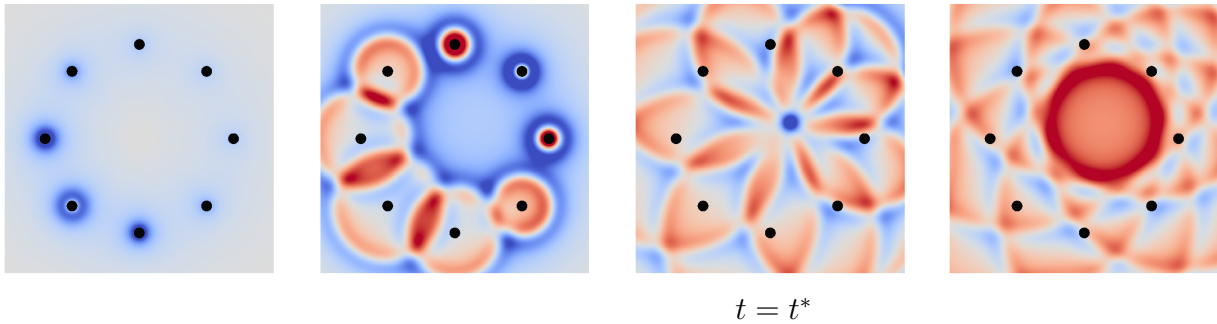


Figure 2.3: Example of propagation of time-reversed waves back into homogeneous medium. The US source is depicted by a circle and sensors as boxes.

of sources that act at single points, the sensor positions, and its time function consists of the time-reversed measured data $u_0(x_i^r, T - t)$.

To verify the applicability of time reversal for NDT a numerical experiment is considered next. This allows to check the concept and test the accuracy. Furthermore, the following uncertainties and errors that might be present between experiment and simulation are eliminated in the verification process:

- the material parameters and geometry of the defective structure are known,
- the recording and retransmission positions agree exactly,
- the excitation of a purely axis-symmetric wave mode is possible,
- the recordings are free from noise.

For the numerical verification, a 10 mm thick aluminum plate of dimensions $1000 \times 1000 \text{ mm}^2$ is inspected. A short US impulse with frequency 35 kHz is applied in the middle of the plate exciting flexural waves that propagate through the medium and are recorded at eight sensors positioned on a circle around the center. In this setup the propagation of flexural waves can be described by a 2D acoustic model neglecting the thickness of the plate (Huthwaite and Simonetti, 2013). The plate is discretized by finite differences of fourth and second order in space and time respectively on a grid with a spacing of 2.5 mm in both directions. The physical domain is extended by a small layer to avoid reflections from the boundary.

In real applications these data are generated in a lab or field experiment. Fig. 2.3 illustrates the computational time reversal simulation. The recorded signals at the sensors are time-reversed and played back into the structure. The sensors are now acting as sources. Snapshots of the backpropagating wave field are shown. At some, generally unknown time t^* , the waves focus on its origin and then diverge again. In the method, the maximal absolute displacement at the time of the wave field is used to infer the original position of the source. The position where the maximal amplitude of the wave field occurs can be determined by observing the pressure field during the simulation. The numerical experiment confirmed that time reversal can be applied to NDT applications, at least in simulations.

Time-reversal, whether experimental or computational, suffers from the fact that it is solely based on the refocusing property of wave propagation. This means that refocusing will occur

in a region of the size of the wavelength close to the original source position. Dealing with multiple flaws (and the separate focusing) or extended inclusions and flaws that are larger than the wavelength poses serious problems. Furthermore, due to the limited number of sensors the recreated waveform only approximates the original one and often the largest amplitude of this wave field does not necessarily coincide with the origin of the waves. Therefore, some more evolved measures have been developed to correctly identify the right peak (Amitt et al., 2014; Givoli, 2014; Givoli and Turkel, 2012). These include a combination of the following measures:

- the distance of the numerical peak from the true source,
- the ratio of height to width (variance) of the peak,
- the location of the refocusing spike in the wave field,
- the sharpness of the refocusing spike in the wave field,
- the weakness of the wave field outside of source origin,
- the total variation of the wave field: a lower value indicates a flatter wave field outside of source origin,
- the maximum total energy density.

Which of these measures to use and how to weight them correctly for a successful detection is problem dependent and needs a lot of experience. A mathematically more concise approach to solve the focusing problem is investigated next.

2.4 Sensitivity kernel method

The temporal and spatial refocusing problem of time reversal can be solved to some extent if a simulation model for the healthy reference structure is available additionally to the measurements from the flawed structure. In our case the simulation model is described by the acoustic wave equation:

$$u_{tt}(x, t) - v_p^2(x)\Delta u(x, t) = f_s(x, t) \text{ for } x \in \Omega \subset \mathbb{R}^2 \text{ or } \mathbb{R}^3, t \in [0, T] \quad (2.45a)$$

$$u(x, 0) = u_t(x, 0) = 0, \text{ on } \Omega \quad (2.45b)$$

$$u = 0 \text{ on } \partial\Omega \quad (2.45c)$$

Equation 2.45 describes the pressure field u induced by an applied ultrasonic impulse f_s in a two- or three-dimensional domain Ω for a time span of T (micro) seconds. All boundaries are assumed to be rigid. Here, v_p is the speed of the pressure waves in the material. Impulse f_s is commonly modeled as a point source, $f_s = A(t) \cdot \delta(x - x_s)$, where x_s is the source position and $A(t)$ is the time-varying amplitude of the source.

The forward wave field can be used as *photographic developer* (Dominguez and Gibiat, 2010) for the time-reversed field and therefore solves the refocusing problem of time reversal in an elegant way. In photography a developer is a chemical that converts the latent image to a visible image. It only acts on those particles of silver halides that have been exposed to light. As will be shown later, in a similar way the forward wave field highlights areas where a scattering of the

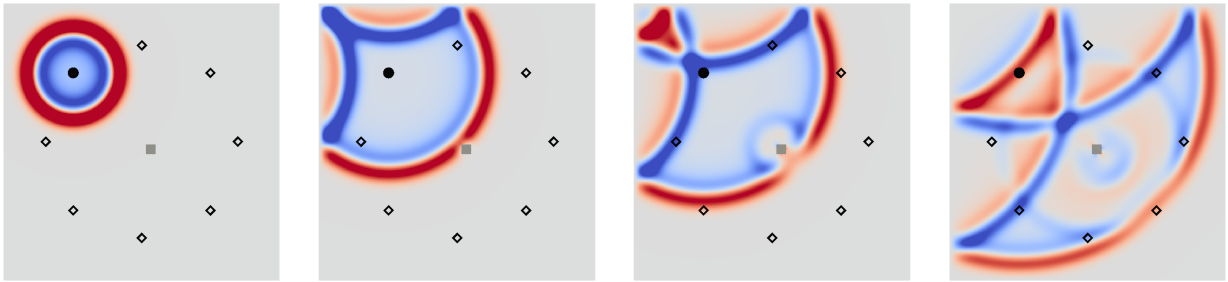


Figure 2.4: Example of propagating wave in homogeneous medium with a point-like scatterer. The US source is depicted by a circle and sensors as diamonds.

wavefield occurred and suppresses most of the noise introduced by the partial measurements of the wavefield.

If an unknown medium of the same type as the reference which possibly contains defects is inspected, the idea is to formulate a *cost function* which evaluates the difference between measurements from the unknown and reference medium. For N_s sensors that record the wave field, the cost function is formulated as the following scalar least-squares functional:

$$J(m) = \frac{1}{2} \int_{\Omega} \int_0^T \sum_{i=1}^{N_s} [u(m; x, t) - u_0(x, t)]^2 \cdot \delta(x - x_i^r) dt dx,$$

where $u(m; x_i^r, t)$ is the simulated and $u_0(x_i^r, t)$ the observed ultrasonic signal for sensor at position x_i , written using the Kronecker-Delta δ . If the measurements in the inspected medium and the reference medium agree then the cost is zero; otherwise it measures the misfit between the signals. As model parameters $m(x) := v_p^2(x)$, the squared propagation speed in the domain of the reference medium is chosen. Very interestingly, the sensitivity of this cost function to changes in these parameters can be used to visualize the interior of the unknown specimen. It can be computed efficiently by a combination of the solution of the forward problem for the reference medium and the computational time-reversal solution where the source is given by the residual between simulated and experimentally measured signals. By considering the residual, only the waves that are contributed to the scatterers acting as secondary source are backpropagated as illustrated in Fig. 2.4

To illustrate this, Fig. 2.4 shows how a point-like scatterer is acting as secondary source. The scatterer is modeled as a small region where the wave propagation speed is smaller than the speed for the background. When the wave field passes through the scatterers a new elementary wave front is created according to Huygens principle. Starting from the reference model a sensitivity analysis of this cost function is performed. A high sensitivity in a certain area indicates that the misfit and therefore the difference in the signals is strongly affected by changes in the wave speed at this position.

The gradient with respect to changes in the wave speed is given by

$$\frac{\partial J}{\partial m} = - \int_0^T \Delta u(m; x, t) \cdot v(x, t) dt, \quad (2.46)$$

where $u(m; x, t)$ is the solution of the forward problem in the reference medium and $v(x, t)$ is the solution to the following adjoint problem (Seidl and Rank, 2016).

$$v_{tt}(x, t) - v_p^2(x)\Delta v(x, t) = g_s(x, t) \text{ for } x \in \Omega \subset \mathbb{R}^2 \text{ or } \mathbb{R}^3, t \in [0, T] \quad (2.47a)$$

$$v(x, T) = v_t(x, T) = 0, \text{ on } \Omega \quad (2.47b)$$

$$v = 0 \text{ on } \partial\Omega \quad (2.47c)$$

where

$$g_s(x, t) := \sum_{i=1}^{N_s} [u(m; x, t) - u_0(x, t)]\delta(x - x_i^r).$$

The derivation will be shown in detail in Sec. 3.3. Spatial boundary conditions carry over one-to-one, but temporal conditions change from initial to terminal conditions at time $t = T$. These can be handled by solving the equation *backward in time* from T to 0.

$$u_{tt}^{\text{TR}}(x, t) - v_p^2(x)\Delta u^{\text{TR}}(x, t) = g_s(x, T - t) \text{ for } x \in \Omega, t \in [0, T] \quad (2.48a)$$

$$u^{\text{TR}}(x, 0) = u_t^{\text{TR}}(x, 0) = 0, \text{ on } \Omega \quad (2.48b)$$

$$u^{\text{TR}} = 0 \text{ on } \partial\Omega \quad (2.48c)$$

where

$$g_s(x, T - t) = \sum_{i=1}^{N_s} [u(m; x, T - t) - u_0(x, T - t)]\delta(x - x_i^r).$$

This way, the adjoint problem can be solved with the same solver as the forward problem, provided that the source term is time-reversed as shown in Eq. 2.48. Because of the somewhat unusual terminal conditions, solving the adjoint problem can be interpreted as a propagation of residuals backward in time from T to 0. This is similar to the time reversal problem 2.44, where the adjoint source is built as a superposition of sources that act at single points, the sensor positions, and its time function consists of the residual between experimental and simulated data. The time reversal problem is identical to the forward problem, except that the time travels in the opposite direction. The adjoint solution is then given by $v(x, t) = u^{\text{TR}}(x, T - t)$, $\forall t \in [0, T]$. The approach of using the interaction between the simulated wave field in a reference medium and the time-reversal solution as indicated in Eq. 2.46 is very general and is utilized in different methods. In seismology, this concept is extensively used in reverse time migration (Baysal et al., 1983; Yoon et al., 2004; Zhang and Sun, 2009) and in NDT in the topological gradient and topological energy method (Dominguez and Gibiat, 2010; Dominguez et al., 2005). It also forms the basis of full waveform inversion (Fichtner, 2011; Tarantola, 1984; Virieux and Operto, 2009).

The general procedure is as follows

- (i) *Measurement.* An US experiment on the inspected medium is performed, which leads to measurements at some sensors: $u_0(x_r, t)$, $i = 1, \dots, N_s$.

- (ii) *Reference simulation.* A simulation model of the unflawed reference structure is used to generate comparable measurements at the position of the sensors and the wave field (or some quantity of it, depending on the choice of model parameters) is available for the complete domain: $u(m; x_r, t), \Delta u(m; x, t)$
- (iii) *Time-reversal.* A computational time reversal simulation is done in the reference medium using the time-reversed residuals $u(m; x_r, T - t) - u_0(x_r, T - t)$ as source array. The adjoint solution is $v(x, t) = u^{\text{TR}}(x, T - t)$.
- (iv) *Sensitivity kernel.* The cumulative interaction $\int_0^T \Delta u(m; x, t) \cdot v(x, t) dt$ offers an image of the inspected medium.

Although the mathematical derivation of the sensitivity kernel will be shown in detail in Sec. 3.3 a short explanation is in order. As shown in Eq. 2.46, the sensitivity kernel corresponds to the gradient of the least-squares objective. It tells us how strongly the value of the objective function changes when a parameter m_i is varied. As the objective function measures the misfit between experimental and simulated measurements at the sensors, a large negative value for parameter m_i indicates that decreasing this parameter (and therefore the wave speed at this position) will lead to a smaller misfit and thus a simulated signal that is closer to the experimental measurement.

The numerical verification example for time reversal is extended to demonstrate the computation of the cumulative interaction of forward and adjoint field. It is often called *sensitivity kernel* as it provides the sensitivity of the cost function to perturbations in the model parameters, hence we call the method *sensitivity kernel method*. All boundaries are considered rigid.

Fig. 2.5 shows snapshots of forward and adjoint field. The unknown flaw is only shown for reference in all the images. The time reversal solution is discovered inspecting the adjoint wave field in the second column in reverse order. The sensitivity kernel is constructed by the cumulative interaction of the forward and adjoint field. The interaction of both fields at a certain time step is zero in most of the domain. Importantly, both fields overlap exactly at the time when the forward wave field is scattered in the unknown physical experiment at the defect location at time t_3 (as indicated in the leftmost column). At this time, the adjoint field focuses on the location of the defect (its secondary source) and the forward solution passes through it leading to a strong interaction of both wave fields at the scatterer location as most energy is focused on one spot in the adjoint field. The largest amplitude of the interaction wave field will be smaller at all other times as one of both fields diverges. Therefore, the time integration shown in the last column leads to large values at the defect location. Thus, the forward field acts very similar to a *photographic developer* of the time reversal solution (Dominguez and Gibiat, 2010). It highlights areas where a scattering of the wavefield occurred and suppresses most of the noise introduced by the partial measurements of the wavefield.

In the end, the energy of the forward field is further distributed and the energy of the adjoint field focuses back on the sensor locations to fulfill the termination condition. It is important to note that the interaction of both wave fields will not be maximal at the scatterer location (the secondary source location) but at the primary source location as the amplitude of the primary source is considerably larger than the amplitude of the secondary source (the scattering at the flaw) due to geometrical spreading. Following a similar argument, there is also a large contribution at the sensor locations because of the formulated terminal conditions for the adjoint problem. The computed sensitivity kernel is shown on the bottom right of Fig. 2.5. It

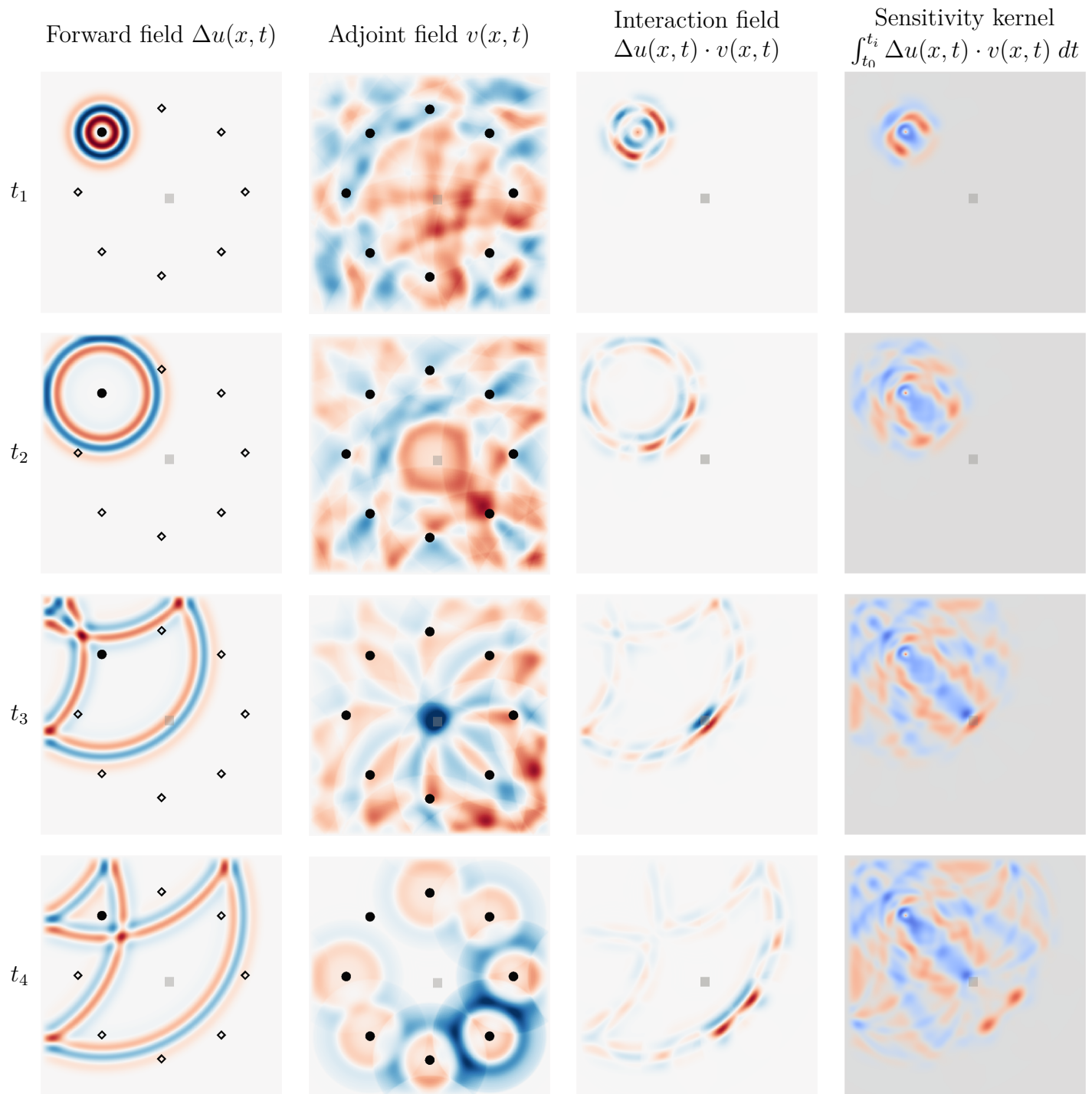
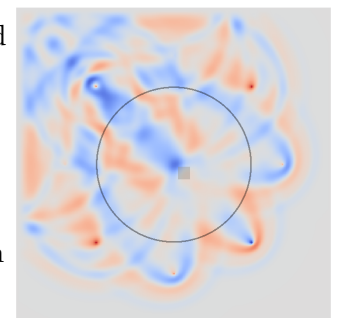


Figure 2.5: Interaction between forward wavefield of reference simulation and adjoint wavefield. The columns show snapshots of the forward wavefield, adjoint wavefield and the interaction of both fields respectively. The forward wavefield acts as photographic developer for the adjoint field. The cumulative summation of the interaction wavefield is a migrated image of the structure. The cumulative interaction yields the final sensitivity kernel shown on the bottom right.



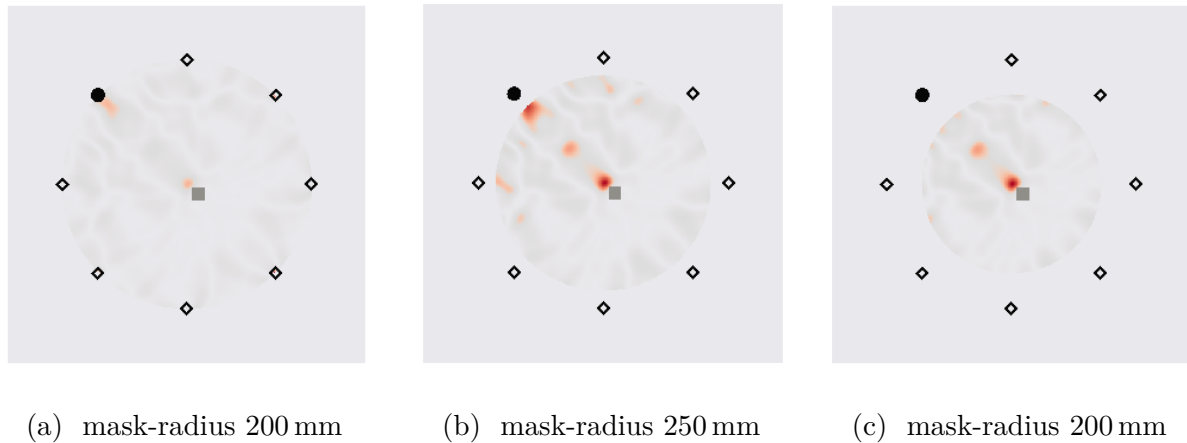


Figure 2.6: Sensitivity kernels for point-like scatterer with different masks. The US source is depicted by a circle and sensors as diamonds. As reference, the unknown flaw is shown as grey box. All kernels are normalized.

has large values at the positions of the source and the sensors and the position and shape of the unknown scatterer can not be easily spotted.

In the case of NDT it is reasonable to assume that the source and sensor positions and small areas around them are flawless and can be excluded in the investigation. Therefore, all entries in the sensitivity kernel in areas that are close to the sensors and source or outside the sensor array can be masked by setting their contribution to zero. A circular region interesting for the inspection which does not contain sensors and sources is highlighted with a circle in the sensitivity kernel on the bottom right. This results in a clearer focus on the scatterer. This is investigated next.

Fig. 2.6 displays the masked (and normalized) sensitivity kernel applying circular masks with different radii. The position of the unknown flaw can be inferred if the mask excludes the sensor and source positions.

It is important to note that the number and positioning of US sensors has a strong influence on the flaw detection. The more sensors are used, the stronger is the refocusing on the scatterers in the time-reversal solution and the larger the contribution in the sensitivity kernel.

To investigate this, Fig. 2.7 studies the masked normalized sensitivity kernel for an increasing amount of sensors. Even though using eight sensors allows to spot the unknown defect close to the center, it is not sufficient to conclude that there is only one scatterer as illustrated in Fig. 2.7a.

Successively increasing the number of sensors (and therefore the amplitude of the refocusing at the scatterers location) results in a clearer image of the scatterer as shown in Figs. 2.7b and 2.7c, where the number of sensors is increased from 7 to 15 and 31 sensors.

In practice, there is a limit for the maximal amount of sensors in most NDT application because of the shape and the dimensions of a typical specimen and considerations such as costs, additional mass and structural integrity. In this case, another possibility to increase the resolution of the kernel is to combine the sensitivity kernels for multiple experiments.

Fig. 2.8 illustrates the combined sensitivity kernels of four experiments where each sensor acted as source once and all other sensors recorded the waves. The flaw is shown only as reference. Here, less sensors suffice to capture the boundaries of the flaw.

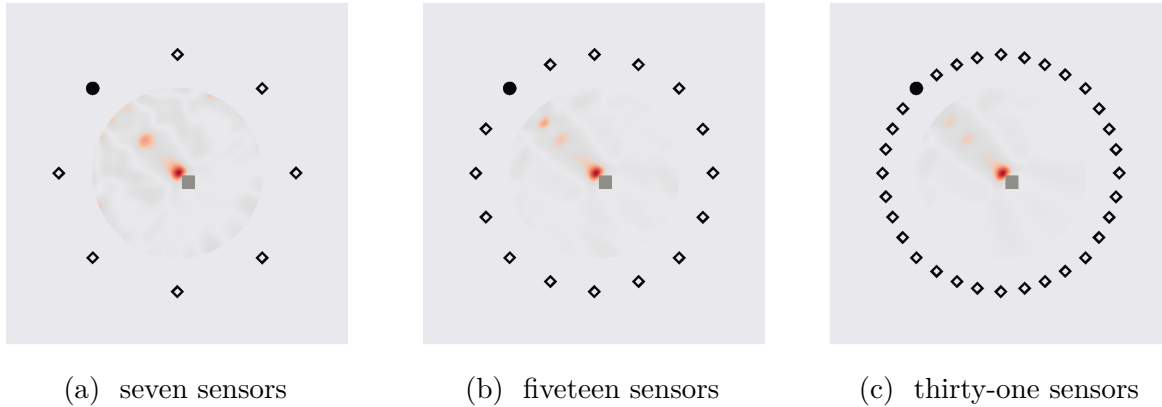


Figure 2.7: Sensitivity kernels for point-like scatterer with different number of sensors. The US source is depicted by a circle and sensors as diamonds. All kernels are normalized

2.5 Summary

Time reversal, a model-based NDT technique, was shown to be able to identify small scatterers. It is based on the invariance of the wave equation to time reversal, meaning that waves can be played forward or backward using the same equation. In time reversal sensors become sources and the measurement signals are backpropagated in a first-in last-out fashion. As only recorded signals at the sensor positions are available, the wave field is only partially known and the quality of the refocusing depends strongly on the number of sensors and their distance to the original source location.

The problem to detect the time and location of refocusing can be solved by introducing the forward wave field of the corresponding healthy structure. A time integration of the interaction between forward and adjoint wave field yields a clearer image of the scatterers location. Therefore, this approach can be interpreted as extension of time reversal. But, only point-like scatterers can be inferred, and as it is summarized in (Givoli and Turkel, 2012):

“Other tools have to be combined with TR to identify larger scatterers which can not be regarded as point-like and to identify other parameters of the scatterers such as its size or shape.” As we will see, in full waveform inversion, time reversal and the sensitivity kernel method are naturally derived as integral parts for the computation of the gradient of a misfit functional with help of the adjoint method.

This puts both methods in perspective in a mathematically sound formulation of an inverse acoustic parameter estimation problem that allows to detect multiple scatterers of different dimensions and orientation (Fichtner et al., 2009; Tromp et al., 2008). Therefore, the principles of full waveform inversion are described next.

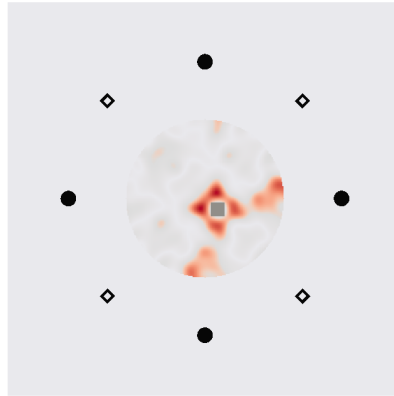


Figure 2.8: Sensitivity kernel for point-like scatterer combining multiple experiments. The source positions are depicted by circles. The unknown flaw is only shown as reference. The kernel is normalized.

Chapter 3

Full Waveform Inversion

Full waveform inversion is introduced next. It is shown how it can be interpreted as adaptive model-based NDT device, where a numerical comparison of signal characteristics between simulated and measured signals allows an iterative correction of a velocity model. The required theory in nonlinear optimization is presented and the adjoint method, which enables the calculation of the high-dimensional gradient necessary for the iterative minimization, is discussed in detail. In the end, the overall algorithm is formulated.

3.1 Description as model-based NDT system

As explained previously, based on experiments alone it is possible to infer the state of a component but this usually provides only limited details about the interior damage such as its position, dimensions, and orientation. Furthermore, the number of sensors that can be used to record the signals is restricted to only a few because of the shape and the dimensions of a typical specimen.

To overcome the constraint of separate consideration of potential flaw features, as well as the approximation of full reflectivity of waves at internal flaws, full waveform inversion can be employed to automatically approximate the structure estimate for high-resolution imaging in US NDT. Starting with a rough velocity model, high resolution imaging of complex structures, including the automatic detailed mapping of internal flaws, is realized by the following model-based NDT system shown in Fig. 3.1.

Compared to the classical NDT system, the experimental measurement process is augmented by a simulated measurement process that allows a numerical comparison of signal characteristics at the sensors. Initially, the simulated measurements are performed utilizing a velocity model of the flawless structure. Flaws and other discontinuities hidden in the experimental structure produce reflective interfaces that are captured in the experimental signals and are not present in the simulated ones. The idea is to employ this difference between observed and simulated signals to adapt the initial velocity model step by step such that the simulated signals are as close as possible to the experimental ones. Flaws are generally treated as deterioration of material parameters. As the only difference in the model and the experiment is the presence of flaws, it is expected that the adapted velocity model contains valuable information about the flaws, like position, orientation, and dimensions. Analyzing the complete wave signal to build a detailed updated velocity model has been approved for seismological and geophysical

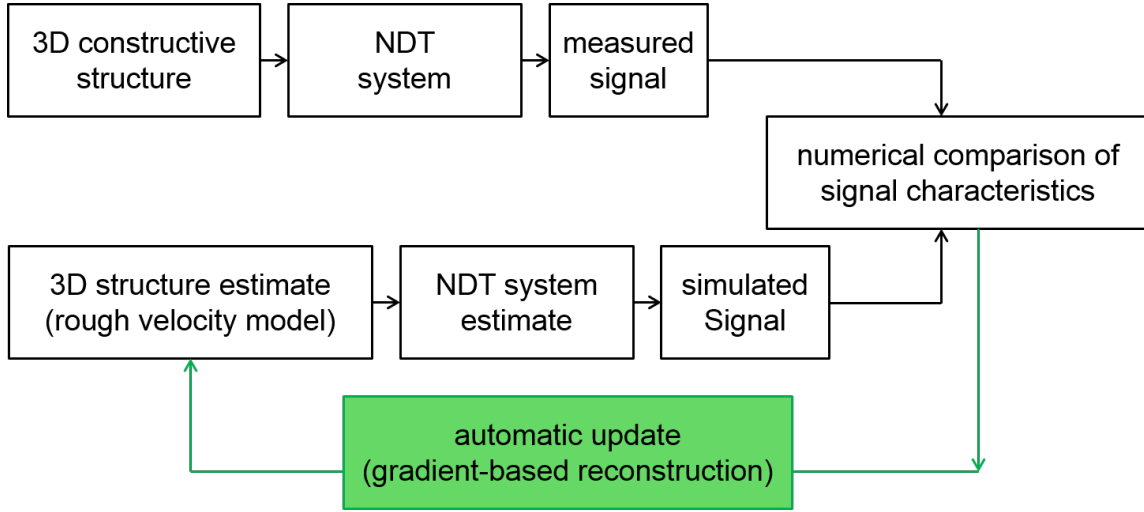


Figure 3.1: Adaptive model-based NDT device

high-resolution imaging Fichtner (2011); Tarantola (1984); Virieux and Operto (2009). As the result of full waveform inversion is a velocity field of the flawed structure, a visual inspection for NDT is easily possible.

It should be stressed that this methodology is not limited to the acoustic case. It can also be applied to US NDT problems that are based on the propagation of surface or body waves. In this case the elastic wave equation has to be used instead. In case of strong inhomogeneous materials, an accurate model of the healthy structure might be obtained from an initial CT scan. If the structure includes complex features like rivets or stringers the geometry can be derived from a CAD model.

The question to be answered is a calibration problem: *How do we need to change the wave speed model in the simulation to generate signals at the sensors that are similar to the ones observed in the experiment?*

Formally, the problem is posed as a nonlinear optimization, and the wave speed model is updated iteratively such that the discrepancy between the experimental measurements and the model output is minimized. If an unknown medium of the same type as the reference medium which possibly contains defects is inspected, the idea is to formulate a *cost function* which quantifies the difference between measurements from the unknown and reference medium. For N sensors that record the wave field, the cost function is formulated as the following scalar least-squares functional:

$$J(m) = \frac{1}{2} \int_{\Omega} \int_0^T \sum_{i=1}^{N_s} [u(m; x, t) - u_0(x, t)]^2 \cdot \delta(x - x_i^r) dt dx,$$

where $u_0(x_i^r, t)$ is the observed ultrasonic signal for sensor at position x_i over the time period $[0, T]$, written using the Kronecker-Delta δ and $u(m; x, t)$ is the solution of the acoustic wave equation for a given material model $m(x) := v_p^2(x)$. If the measurements in the inspected medium and the reference medium agree then the cost is zero; otherwise it measures the misfit

between the signals. The goal is to try to minimize the misfit $J(m)$ by adapting $m(x)$ in the simulation model. When formulating the problem this way, it does not rely on prior knowledge of the dimension and the location of flaws. This is an important advantage over most NDT methods that allows the simultaneous detection of multiple flaws of different dimensions.

This inverse problem can, in principle, be tackled using non-linear optimization methods. For a comprehensive overview on theory and methods see e.g. Fletcher (2008); Nocedal and Wright (1999); Polak (1997); Quarteroni et al. (2000). The nonlinear cost function is very high-dimensional and global optimization methods are not applicable. The only viable option is a local iterative optimization. As inverse problems are per definition ill-posed and because of the typically very limited number of measurements, an exact reconstruction of the flawed structure cannot be expected, but assuming that the initial model is accurate enough, a local minimum might already provide valuable insight about position, dimensions, and orientation of possible flaws.

Therefore, the fundamentals of nonlinear optimization are discussed next.

3.2 Nonlinear Optimization

This chapter deals with the analysis and general numerical treatment of nonlinear optimization problems. Many important engineering problems can be treated as optimization problem where a continuous *objective function* has to be either maximized or minimized with respect to some *design variables* m . Additionally, a *state variable* u is also depending on m .

$$\begin{aligned} \min_{m \in \mathbb{R}^N} J(m, u(m)) \\ \text{s.t. } h(u(m)) = 0 \end{aligned} \tag{3.1}$$

Both, the objective function J and state equation h are considered to be smooth and sufficiently often differentiable to apply the optimization methods that are presented in this chapter. The objective J is assumed to be nonlinear throughout this work. The content of the chapter follows introductions to nonlinear optimization in (Nocedal and Wright, 1999), (Christensen and Klarbring, 2009), (Fichtner, 2011) and (Ulbrich and Ulbrich, 2012), especially extending the given definitions in (Christensen and Klarbring, 2009) to the problems studied in this thesis. The following functions and variables are always present in the kind of optimization problems that are considered in this thesis.

- *Objective function (J):* A function used to classify designs using a reasonable performance measure. J returns a value which indicates the quality of the design. Usually J is chosen such that a small value is better than a large value (a minimization problem). For example in structural optimization J might measure weight, displacement in a given direction, effective stress or even cost of production. In our US NDT problem it measures the discrepancy between the generated signals of our simulation model (pressure or displacement) at the sensors and the desired signals from the US experiment.
- *Design variable (m):* A function or vector which describes the design and can be changed during optimization. It may represent geometry or choice of material. In our case it represents the speed of pressure waves inside the object and is often referred to as speed model or simply model instead of design.

- *State variable (u):* For a given design m , u is a function or vector that represents the response of the structure. For a mechanical structure, response means , e.g., displacement, reaction force, strain or stress. In our case it represents the pressure field induced by an ultrasonic impulse.
- *State equation (h):* A function that describes the state or equilibrium of a physical system. It can also be seen as a dynamic constraint. For instance, for discrete structural optimization this might be a linear equilibrium constraint like

$$K(m)u = F(m) \quad (3.2)$$

with $K(m)$ being the stiffness matrix of the structure, which is a function of the design m , u is the displacement vector and $F(m)$ is the force vector which may also depend on the design m . In a continuum problem as it is considered in this thesis this will typically be a partial differential equation like the acoustic wave equation

$$u_{tt}(m; x, t) - v_p^2(x)\Delta u(m; x, t) = f_s(x, t) \text{ for } x \in \Omega \subset \mathbb{R}^2 \text{ or } \mathbb{R}^3, t \in [0, T] \quad (3.3a)$$

$$u(m; x, 0) = u_t(m; x, 0) = 0, \text{ on } \Omega \quad (3.3b)$$

$$u = 0 \text{ on } \partial\Omega, \quad (3.3c)$$

where its solution $u(m; x, t)$ is the induced pressure field by the ultrasonic impulse f_s and $m := v_p^2(x)$. Optimization problems occur in almost all engineering disciplines as well as in physics, chemistry, economics, astronomy, data mining and geophysics. Examples include the computation of minimal surfaces or portfolio optimization. Broader areas are optimal control problems where one might want to minimize the necessary fuel to put a space ship to a certain orbit or different applications in robotics. Another larger area of optimization is in the form of regression / fitting. Here, you try to fit the modeled system responses of a physical, technical or economic system with measurements as good as possible. This is often done in a least-squares sense. Examples in the area of mechanics are topology and structural optimization. Also full waveform inversion as described in Chapter 3 can be viewed as nonlinear least-squares problem.

The value of the objective function J can be either scalar or vector valued. In the latter case this leads to multi-criteria optimization. We restrict ourselves to the simpler case of scalar objectives.

Design parameters m and state variable u can be either discrete, i.e. n tuples of real numbers or continuous fields that can be thought of to have an infinite number of degrees-of-freedom. In the latter case one speaks about distributed parameter systems. They need to be discretized first before they can be tackled by a computer. An example of such a field is the continuous wave speed inside a domain that needs to be discretized on a grid.

Given that the nonlinear objective function is sufficiently smooth, it is well known from basic calculus that the gradient vanishes at a local minimum m^* :

$$\nabla J(m^*) = 0.$$

A nonlinear function can have multiple local and global minima but the value of the objective is only minimal in a global minimum. This is illustrated in Fig. 3.2.

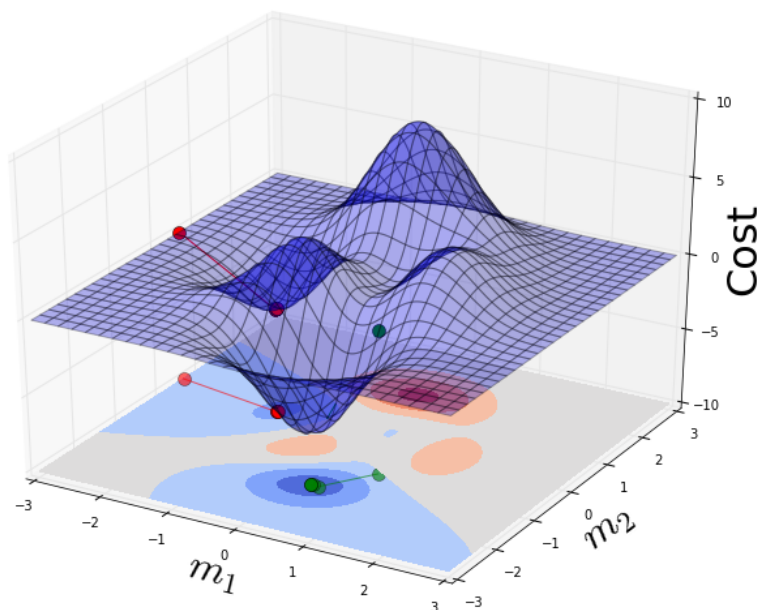


Figure 3.2: Local and global minima of a nonlinear function

In most cases there exist no analytical solution to problem 3.1 and one is forced to apply numerical methods to solve the problem. The solution algorithms can be divided into two classes which follow different strategies. *Global optimization algorithms* find the global minimum of the objective by a clever sampling of the design space. They are very user friendly as they only need a routine to evaluate the objective. But they often need a large number of evaluations for as few as ten design parameters. The exponential increase of the number of samples with the dimension of the design space limits their applicability to problems where the product of the number of design parameters and the computational cost for the evaluation of the objective is not too large, as described in (van Laarhoven and Aarts, 1992). Examples are grid search, simulated annealing or genetic algorithms. *Local algorithms* use additional information on the shape of the graph of the objective by additional function evaluations (Conn et al., 2009) or by incorporating derivative information. They converge only to a *local* stationary point but need much less iterations. Using derivative information makes the methods applicable to large scale problems with possibly thousands to millions of design parameters. But this comes at the cost of being less user-friendly as the user needs to provide an additional routine for the evaluation of the derivative of the objective function and this often requires delicate calculations and coding.

Figure 3.3 illustrates the different approaches for a nonlinear objective function. The plotted lines represent the contours of constant objective values. In Figure 3.3a a global optimization method like grid search evaluates the objective on different positions marked by red circles and chooses the position with the smallest value, marked by a square as minimum. In contrast, Fig. 3.3b shows a local minimization method. It starts with an initial guess and then follows the objective downhill to decrease its value. This way a lot less function evaluations are needed to find a local minimum. In this example, starting with an initial guess far away from the minimum on the top left, the sequence only converges to a local minimum. Only if the initial

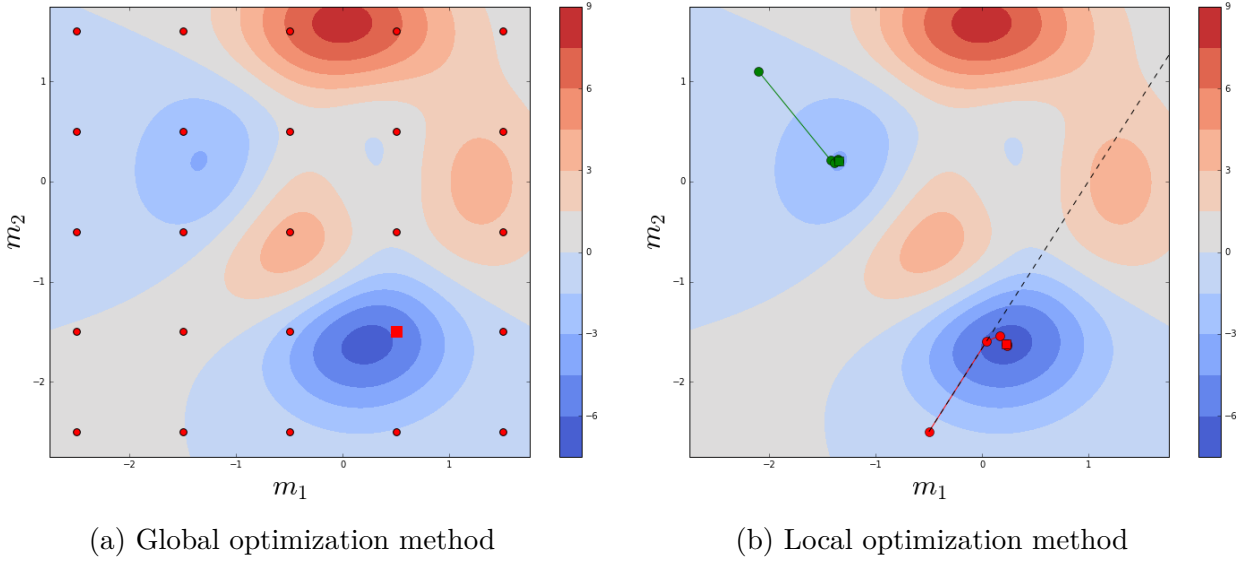


Figure 3.3: Illustration of global and local optimization methods.

guess is good enough, the global minimum is found. The dashed line indicates the direction of the negative gradient. The next section presents the basic iterative local optimization methods that are used to tackle large scale problems.

3.2.1 Descent Methods

3.2.1.1 General formulation

The idea of descent methods is to solve the nonlinear optimization problem 3.4 iteratively.

$$\begin{aligned} \min_{m \in \mathbb{R}^N} J(m, u(m)) \\ \text{s.t. } h(u(m)) = 0 \end{aligned} \quad (3.4)$$

For simplicity, the implicit dependence of the objective on the state $u(m)$ and the state equation $h(u(m))$ is dropped for the presentation of general numerical methods. But it is important to keep in mind that evaluating J means to generate a solution to $h(u(m))$ first which may be very costly.

Starting with an initial guess m_0 , descent methods generate a sequence of iterates $\{m_k\}_{k=1}^{\infty}$ using information about the objective at the actual iterate m_k such that the value of the objective function is decreasing step by step.

$$J(m_0) > J(m_1) > \dots > J(m_N) \quad (3.5)$$

Algorithm 1 summarizes the steps for a general local minimization method. After the initialization a *descent direction* has to be determined along which the objective function is guaranteed to decrease. Different possibilities how to determine a suitable step size to decrease the objective function are presented in Sec. 3.2.1.3. This process is repeated until the objective function is not changing much anymore and the iterates are close to a local minimum. The next sections present the details about strategies for step size selection and for choices of descent directions.

Algorithm 1 Descent Method

Initialize $m_0, k = 0$
repeat
 1. Define descent direction p_k
 2. *Line search.* Choose step size γ such that $J(m_k + \gamma_k p_k) < J(m_k)$
 3. *Update design parameter.* $m_{k+1} = m_k + \gamma_k p_k$
until stopping criterion is satisfied.

3.2.1.2 Descent directions

The central idea of local minimization methods is the usage of descent directions to explore the design space. A direction p is a descent direction of the objective function J at the current point m in design space, if the slope of J in direction p is negative:

$$\nabla J(m)^T p < 0. \quad (3.6)$$

There are different possibilities to calculate a descent direction. The simplest one is steepest descent which is introduced next.

Steepest Descent

As $\nabla J(m_k)$, the gradient of the objective J at point m_k , is pointing in the direction of greatest ascent of J , the most intuitive choice for a descent direction is to use $p = -\nabla J(m_k)$ as it is pointing in the direction of steepest descent at point m_k . From all possible directions we are choosing the one that decreases the objective J the most. Clearly, p is a descent direction, as can be shown by

$$\nabla J(m)^T p = -\nabla J(m)^T \nabla J(m) < 0.$$

Algorithm 2 shows the steepest descent method. The most delicate part in it is the computation of the gradient $\nabla J(m)$, which can under suitable conditions be done efficiently using the adjoint method. This is the topic of Sec. 3.3.

Even though the negative gradient guarantees the largest decrease of the objective *locally* in a small area around the current solution, it generally is not the optimal choice *globally*. This may lead to a large number of iterations being necessary to converge to a local minimum. For example, steepest descent is largely affected by the scaling of the underlying problem. Consider the following two quadratic problems:

$$\begin{aligned} J_1(m_1, m_2) &= m_1^2 + 2m_2^2, & (m_1^0, m_2^0) &= (-4, 2) \\ J_2(m_1, m_2) &= m_1^2 + 10m_2^2, & (m_1^0, m_2^0) &= (-4, 2) \end{aligned}$$

The contours of constant objective values and the sequence of iterates for steepest descent are shown for the scaled and stretched quadratic function in Figure 3.4a and 3.4b. In the problem with elongated contours the typical overshooting ("zigzagging") of the iterates is observed and a large number of iterations is needed to reach the minimum.

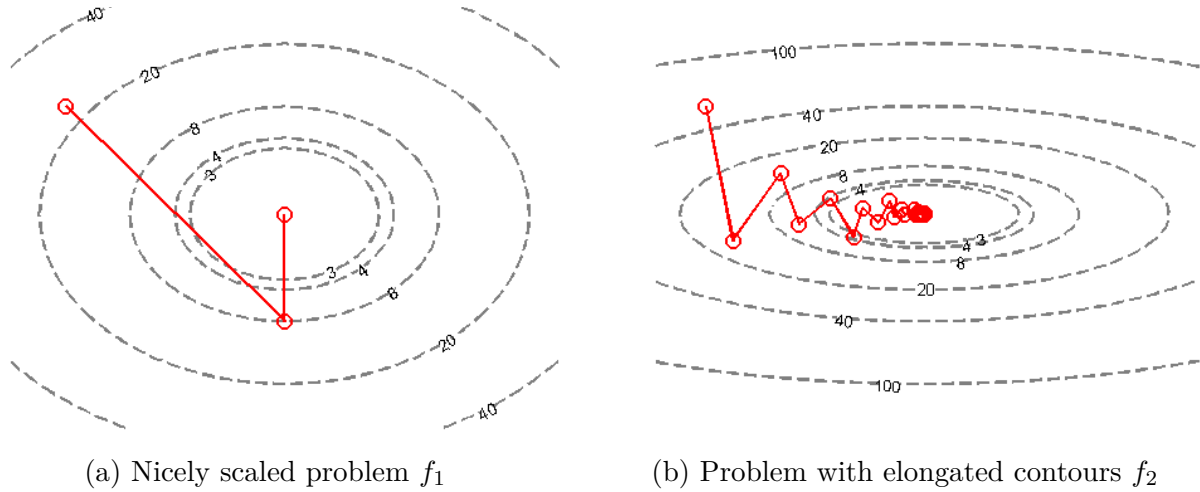


Figure 3.4: Convergence of steepest descent

Algorithm 2 Steepest Descent Method

Initialize $m_0, k = 0$

repeat

1. Compute gradient $\nabla J(m_k)$
2. Define descent direction $p_k = -\nabla J(m_k) / \|\nabla J(m_k)\|$.
3. *Line search.* Choose step size γ_k as described in Sec. 3.2.1.3
4. *Update design parameter.* $m_{k+1} = m_k + \gamma_k p_k$

until stopping criterion is satisfied.

Newton's Method

An improvement to gradient-based optimization is to use information about the curvature of the objective at the current iterate. Given that the objective function is two times differentiable, Newton's method estimates it at the current iterate m^k by a quadratic approximation $q_k(p)$ that is derived by Taylor expansion. A detailed derivation can be found in (Nocedal and Wright, 1999; Ulbrich and Ulbrich, 2012)

$$J(m_k + p) \approx J(m_k) + p^T \nabla J(m_k) + \frac{1}{2} p^T \nabla^2 J(m_k) p =: q_k(p) \quad (3.7)$$

The quadratic model is reliable if the difference between it and the true function $J(m_k + p)$ is not too large. Its minimizer is found by

$$\nabla q_k(p) = 0. \quad (3.8)$$

This leads to the Newton equations

$$\nabla^2 J_k p_k = -\nabla J_k. \quad (3.9)$$

The steepest descent direction is corrected according to curvature information available by the Hessian. It can be used together with a line search as indicated in Algorithm 3. A severe limitation is that in every iteration step the Hessian has to be computed and a linear equation

system solved for the new search direction. It can be shown that this leads to a quadratic convergence rate in the vicinity of the solution (under the condition that the Hessian is positive definite). Additionally, it can be shown that the algorithm is scale-invariant. This means that the initial step size $\gamma = 1$ is almost always accepted in the vicinity of the solution. This results not only in fast convergence but also in a minimal number of needed function evaluations for the line search. This is particularly important when one deals with large-scale problems involving PDEs. But it comes at the cost of the need to calculate and store the Hessian for each iteration. This is clearly infeasible considering the typically large number of design parameters. Possible remedies are inexact Newton methods like Newton-CG or quasi-Newton methods. Inexact Newton methods solve the Newton equation only approximately using an iterative solver like CG with the advantage that only matrix-vector products with the Hessian are needed and storing the Hessian can be avoided.

Algorithm 3 Newton's Method

Initialize $m_0, k = 0$

repeat

1. Compute gradient $\nabla J(m_k)$ and Hessian $\nabla_m^2 J(m_k)$
2. Solve Newton equation $\nabla^2 J(m_k)p_k = -\nabla J(m_k)$
2. *Line search.* Choose step size γ_k as described in Sec. 3.2.1.3.
3. *Update design parameter.* $m_{k+1} = m_k + \gamma_k p_k$

until stopping criterion is satisfied.

Quasi-Newton methods are another attractive alternative that avoid the explicit calculation of the Hessian. They are considered next.

Quasi-Newton Method

Newton's method and its variants suffer from the fact that the Hessian has to be computed and possibly stored each iteration. For large-scale PDE-constraint optimization problems as considered in this thesis the Hessian is not available. The adjoint method as described in Sec. 3.3 can be used to efficiently compute the gradient and Hessian-vector products. Furthermore, the Newton equation, a possibly large linear equation system, has to be solved. All these problems are serious drawbacks. Quasi-Newton methods and especially its variant, the BFGS method, prove to be a very attractive alternative. As in Newton's method, the computation of a descent direction is based on a quadratic approximation of the objective at the current iterate, but the Hessian matrix is replaced by a positive definite approximation B_k , that is:

$$J(m_k + p) \approx J(m_k) + p^T \nabla J(m_k) + \frac{1}{2} p^T B_k p \quad (3.10)$$

Calculating the gradient

$$\nabla J(m_k + p) \approx \nabla J(m_k) + B_k p, \quad (3.11)$$

and setting it to zero provides the new descent direction

$$p = -B_k^{-1} \nabla J(m_k). \quad (3.12)$$

The positive definite Hessian approximation B_k is updated each iteration to incorporate the curvature information gained through $\nabla J(m_k)$ and $\nabla J(m_{k+1})$ in the current iteration. Precisely, it is chosen such that the secant equation is satisfied for the new approximation of the Hessian B_{k+1} :

$$\nabla J(m_k + p) = \nabla J(m_k) + B_{k+1}p, \quad (3.13)$$

which is often written more compactly as

$$B_{k+1}s_k = y_k, \quad (3.14)$$

where

$$s_k = m_{k+1} - m_k, \quad y_k = \nabla J(m_{k+1}) - \nabla J(m_k). \quad (3.15)$$

Furthermore, it has to satisfy the curvature condition $s_k^T y_k > 0$ to ensure its positive definiteness. The most widely used quasi-Newton method is the BFGS method, which was suggested independently by Broyden, Fletcher, Goldfarb and Shanno in 1970 (Broyden, 1970). The update of the Hessian approximation is corrected after each iteration to incorporate the new information by

$$B_{k+1} = B_k - \frac{B_k s_k s_k^T B_k}{s_k^T B_k s_k} + \frac{y_k y_k^T}{y_k^T s_k}, \quad (3.16)$$

which clearly satisfies the secant equation 3.14. It can be shown that the method converges faster to a local optimum than steepest descent in most applications (Fletcher, 2008). Furthermore, it retains the scale-invariance of the Newton method and the Hessian approximation is guaranteed to be positive definite. The main advantage of quasi-Newton methods is that they can also be used to approximate the *inverse of the Hessian* instead of the Hessian itself. This way no system of linear equations has to be solved at each iteration; only a matrix-vector product is needed. Therefore, practical implementations update the inverse of B_k instead by applying an equivalent formula for the inverse approximation $H_k = B_k^{-1}$ that has to satisfy $H_{k+1}y_k = s_k$ instead. This leads to the following update formula: (Nocedal and Wright, 1999)

$$H_{k+1} = (I - \rho_k s_k y_k^T) H_k (I - \rho_k y_k s_k^T) + \rho_k s_k s_k^T, \quad \rho_k = \frac{1}{y_k^T s_k} \quad (3.17)$$

Algorithm 4 shows an efficient implementation of the BFGS method. The descent direction is computed by a cheap matrix-vector product with the approximation of the inverse Hessian. For the line search the Wolfe conditions as described in Sec. 3.2.1.3 are used to ensure global convergence and the design parameter is updated. After each step the current approximation of the inverse Hessian incorporates the newly available curvature information. Only one problem remains, the approximation to the inverse Hessian is typically dense and has to be stored. If the number of design parameters is large then this is infeasible. Fortunately, it is possible to modify the BFGS algorithm to work with an approximation of the inverse Hessian using only curvature information from most recent iterations instead. The method, called limited memory BFGS or L-BFGS is the topic of the next section.

Algorithm 4 BFGS Method

Initialize m_0 , $k = 0$ and H_0 initial positive definite approximation to inverse Hessian

repeat

1. Compute gradient $\nabla J(m_k)$
2. Compute search direction $p_k = -H_k \nabla J(m_k)$
3. *Line search.* Choose step size γ_k as described in Sec. 3.2.1.3
4. *Update design parameter.* $m_{k+1} = m_k + \gamma_k p_k$
5. Compute new approximation of inverse Hessian H_{k+1}

$$H_{k+1} = V_k^T H_k V_k + \rho_k s_k s_k^T$$

where

$$\rho_k = \frac{1}{y_k^T s_k}, \quad V_k = I - \rho_k y_k s_k, \quad s_k = m_{k+1} - m_k, \quad y_k = \nabla J(m_{k+1}) - \nabla J(m_k)$$

until stopping criterion is satisfied.

L-BFGS

For large-scale optimization problems the explicit storage and update of the approximate Hessian is infeasible. The BFGS method obtains H_{k+1} by using the old approximation H_k and the pair $\{s_k, y_k\}$. This matrix is typically dense but a *compact approximation* of it can be assembled by storing $\{s_k, y_k\}$ from most recent iterations. This adapted method is called *limited-memory BFGS* or *L-BFGS method*. The main idea is that only curvature information from recent iterations is likely to be relevant to the actual behavior of the Hessian at the current iterate and curvature information from older iterations can therefore be discarded. The BFGS update formula is given by (Nocedal and Wright, 1999)

$$H_{k+1} = V_k^T H_k V_k + \rho_k s_k s_k^T, \tag{3.18}$$

where

$$\rho_k = \frac{1}{y_k^T s_k}, \quad V_k = I - \rho_k y_k s_k, \quad s_k = x_{k+1} - x_k, \quad y_k = \nabla J(m_{k+1}) - \nabla J(m_k).$$

The approximation can be recovered by repeated application of the BFGS formula from the last r vector pairs $\{s_i, y_i\}$, $i = k - r, \dots, k - 1$, where typically $r \approx 3 - 15$. Additionally, an initial positive definite Hessian H_k^0 is chosen that might vary from iteration to iteration. The current estimate of H_k can be reconstructed by repeated application of formula 3.18

$$\begin{aligned} H_k &= (V_{k-1}^T \dots V_{k-r}^T) H_k^0 (V_{k-r} \dots V_{k-1}) \\ &\quad + \rho_{k-r} (V_{k-1}^T \dots V_{k-r+1}^T) s_{k-r} s_{k-r}^T (V_{k-r+1} \dots V_{k-1}) \\ &\quad + \rho_{k-r+1} (V_{k-1}^T \dots V_{k-r+2}^T) s_{k-r+1} s_{k-r+1}^T (V_{k-r+2} \dots V_{k-1}) \\ &\quad + \dots \\ &\quad + \rho_{k-1} s_{k-1} s_{k-1}^T. \end{aligned} \tag{3.19}$$

Algorithm 5 L-BFGS two-loop recursion

```

Set  $q := \nabla J(m_i)$ 
for  $k = i - 1, i - 2, \dots, i - r$  do
   $\alpha_k := \rho_k s_k^T q$ 
   $q := q - \alpha_k \gamma_k$ 
end for
Set  $t := H_k^0 q$ 
for  $k = i - r, i - 2, \dots, i - r$  do
   $\beta := \rho_k y_k^T t$ 
   $t := t + s_k(\alpha_k - \beta)$ 
end for
return  $H_i \nabla J(m_i) = t$ .

```

This leads to a recursive procedure to calculate the matrix-vector product $H_k \nabla J(m_k)$ efficiently. This two-loop recursion is shown in Algorithm 5. An important detail is the choice of the initial approximation H_k^0 , an effective choice is $H_k = \sigma_k I$, where

$$\sigma_k = \frac{s_{k-1}^T y_{k-1}}{y_{k-1}^T y_{k-1}}. \quad (3.20)$$

This choice helps to ensure that the search direction is well scaled, and as a result the step size $\gamma_k = 1$ is accepted in most iterations. This minimizes the amount of function evaluations for the step size selection which is very important when function evaluations are very costly. The final algorithm agrees with algorithm 4 in most parts. It only differs in the computation of the descent direction by employing the two-loop recursion shown in algorithm 5 to calculate $-H_k \nabla J_k$ and it has to store the last r vectors s_i and y_i for the next iteration.

After finding a descent direction, the next step is to compute a step size along it. Different approaches are considered next.

3.2.1.3 Step size selection

If p_k is a descent direction, then the value of the objective J can be reduced along the direction p_k . There is a trade off, as this is a one-dimensional nonlinear optimization problem on its own that can be very costly to solve and might need a lot additional evaluations of the cost function. As a compromise, we want to choose a step size that leads to a substantial reduction in the value of the objective using as few function and gradient evaluations as possible. Therefore, most of the described methods accept a value of γ that leads to a large enough reduction in the objective. In the following different methods that find the optimal step size or a reasonable estimate are presented.

Exact solution

Ideally, we would want to choose the step size along the direction such that the value of the objective is minimal. For this we would need to perform a minimization of a nonlinear univariate function

$$\phi(\gamma) := J(m_k + \gamma p_k), \quad \gamma > 0. \quad (3.21)$$

Finding the global or even only a local minimum will need a possibly large number of additional function evaluations and it can be shown that it is neither necessary nor efficient to calculate the global minimum at all. Therefore most methods content themselves with finding only an approximate solution.

Curve fitting

A first possibility is to replace the objective function by a simple approximation that can easily be optimized like a quadratic or cubic polynomial. By evaluating $\phi(\gamma)$ at three points γ_1, γ_2 and γ_3 we can determine a quadratic approximation

$$q(\gamma) = a\gamma^2 + b\gamma + c, \quad (3.22)$$

which agrees with $\phi(\gamma)$ at γ_1, γ_2 and γ_3 . The new step size is then found analytically using the global minimizer of the quadratic approximation. Usually, one wants to find a step size as efficiently as possible using a minimal number of function evaluations. Therefore, it is reasonable to use values of $\phi(\gamma)$ that are already available. As $\phi(0) = J(m_k)$ and $\phi'(0) = \nabla J(m_k)^T p_k$ have already been computed in the previous step, they are already available without any new evaluation of the objective, it is possible to interpolate a quadratic polynomial using these points and an initial guess γ_0 . The quadratic approximation is then given by the following formula:

$$g(\gamma) = \left(\frac{\phi(\gamma_0) - \phi(0) - \gamma_0 \phi'(0)}{\gamma_0^2} + \phi'(0)\gamma + \phi(0) \right), \quad (3.23)$$

and its explicit minimizer γ^* is given by the expression

$$\gamma^* = -\frac{\phi'(0)\gamma_0^2}{2[\phi(\gamma_0) - \phi'(0)\gamma_0 - \phi(0)]}. \quad (3.24)$$

In Newton and quasi-Newton methods the step size $\gamma_0 = 1$ should always be tried first, as it is almost always accepted. In contrast, for methods that are not scale-invariant as steepest descent and conjugate gradients, one popular strategy is to assume that the first-order change in the objective at iterate m_k will be similar to the one obtained at the previous step. Therefore, the initial guess γ_0 is chosen such that $\gamma_0 \nabla J(m_k)^T p_k = \gamma_{k-1} \nabla J(m_{k-1})^T p_{k-1}$. Thus,

$$\gamma_0 = \alpha_{k-1} \frac{\nabla J(m_{k-1})^T p_{k-1}}{\nabla J(m_k)^T p_k}. \quad (3.25)$$

A different approach fits a quadratic polynomial using the points $J(m_{k-1}), J(m_k)$ and $\phi'(0) = \nabla J(m_k)^T p_k$ and to define γ^* to be the minimizer

$$\gamma^* = \frac{2(J(m_k) - J(m_{k-1}))}{\phi'(0)}. \quad (3.26)$$

Powell-Wolfe conditions

Another possibility is to test a sequence of candidate values and possibly accept one of them when certain conditions are satisfied that ensure that enough progress is made following the

search direction. At first glance, it seems reasonable to accept any step size γ that is decreasing the value of the objective $J(m_k + \gamma p_k) < J(m_k)$. But this condition is not sufficient as it possibly provides no sufficient reduction in each iteration to converge to the local minimum. Most line search methods therefore require that the chosen step leads to a sufficient decrease of the objective

$$J(m_k + \gamma_k p_k) \leq J(m_k) + c_1 \gamma_k \nabla J(m_k)^T p_k. \quad (3.27)$$

The inequality is called *sufficient decrease condition*. The decrease has to be directly proportional to step size and directional derivative. But the sufficient decrease condition alone is not adequate to ensure that the algorithm makes reasonable progress because it is accepting all sufficiently small step sizes. A common way to ensure that these step sizes are not accepted is to add another condition related to the slope of the objective called *curvature condition*.

$$\nabla J(m_k + \gamma_k p_k)^T p_k \geq c_2 \nabla J(m_k)^T p_k \quad (3.28)$$

with

$$0 < c_1 < \frac{1}{2}, \quad c_1 < c_2 < 1.$$

It prevents that too small values of γ are accepted. The left hand side of formula 3.28 is the derivative of ϕ at γ_k , and thus the condition ensures that the slope at γ_k is greater than c_2 times the slope at 0. Therefore, it excludes all step sizes that are very small. Together, both conditions are known as *Powell-Wolfe conditions*. Typical values for the constants are $c_1 = 10^{-4}$ and $c_2 = 0.9$ for Newton and quasi-Newton methods, and $c_2 = 0.1$ if steepest descent or conjugate gradients are used (Nocedal and Wright, 1999). Algorithm 6 shows a possible implementation of the Powell-Wolfe step size rule. A first test ensures that a step size $\gamma = 1$ is tried. If $\gamma = 1$ is not accepted, we find a step size γ_- satisfying and γ_+ violating 3.27. Then, we find a stepsize γ that also satisfies 3.28 using bisection of the interval $[\gamma_-, \gamma_+]$.

The conditions are illustrated in 3.5. Sufficient decrease condition 3.27 states that the graph of the function $\phi(\gamma)$ has to be below the linear decreasing function $\gamma c_1 \nabla J(m_k)^T p_k$. To exclude arbitrary small choices of γ , curvature condition 3.28 only accepts step sizes where the slope is larger than $c_2 \nabla J(m_k)^T p_k$. The areas where both conditions are satisfied are highlighted on the axis. Furthermore, a typical bisection step is shown, where two step sizes γ_- and γ_+ that violate 3.28 are averaged to find γ^* that satisfies both conditions.

The Powell-Wolfe conditions can be used in most line search methods, but they are particularly important for quasi-Newton methods because they are scale-invariant. This means that multiplying the objective function by a constant or making an affine change of variables does not alter them. Next, different possibilities to terminate the optimization are presented.

3.2.1.4 Termination criteria

The classical termination criterion for the iterative minimization is to stop the process once the gradient of the objective is almost zero

$$\|\nabla J(m_k)\| < \epsilon \cdot \|\nabla J(m_0)\|, \quad \text{where e.g. } \epsilon = 10^{-5},$$

or after a finite number of iterations. Of course, this has the additional benefit of saving computational resources. As another possibility, another practice is to run the inversion for a fixed number of iterations and to choose the model at some iteration after which the model is not changing significantly any more to prevent overfitting.

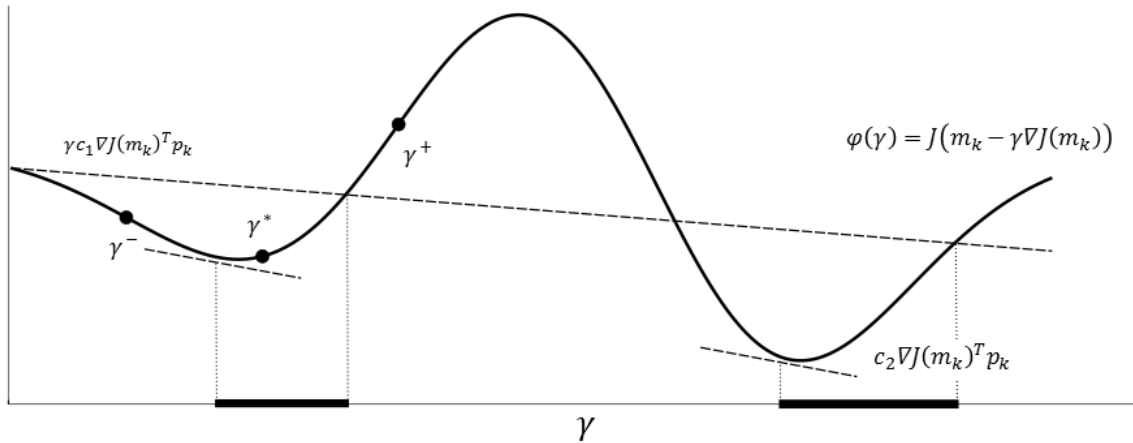


Figure 3.5: Powell-Wolfe step size rule, adapted and extended from (Ulbrich and Ulbrich, 2012)

3.2.2 Summary

To summarize, the main benefits of using L-BFGS are that due to its scale invariance the number of necessary function evaluations for the step size selection is minimized at small costs, especially if function evaluations are related to solutions of PDEs and therefore very costly. The limited-memory variant circumvents the need to store an explicit approximation of the inverse Hessian which leads to low storage requirements. Despite its simplicity L-BFGS often outperforms other local optimization methods and proves to be very efficient especially for large-scale optimization (Nocedal and Wright, 1999). The key ingredient of local optimization methods is the gradient of the objective. It can be computed very efficiently in the case of full waveform inversion using the adjoint sensitivity state method which is introduced next.

3.3 Efficient Computations - The Adjoint State Method

A key part for the transition from forward to the inverse problem described in Sec. 3.1 is the availability of local information about the cost function that should be minimized. The dimension of the parameter spaces considered in this thesis range from 10^4 to 10^6 and this number may exceed 10^{10} for modern applications in seismic inversion (Hinze, 2009). Finite differences and forward approaches are only suitable if the number of model parameters is small. In inverse problems or optimal control the sensitivity of a functional with respect to a large amount of design parameters is needed. For example, in the case of acoustic inversion we are interested in the gradient of a certain functional, representing the error between expected and observed signals at the sensors of some ultrasonic experiment, with respect to a large number of parameters like the distributed compression wave speed on a fine grid. Classical global exploration strategies like simulated annealing or genetic algorithms are not applicable in this setting. The question is: *Is it possible to compute the gradient with respect to this large number of parameters efficiently?* Adjoint approaches circumvent the problem of calculating the sensitivity of the underlying model to each parameter introducing an adjoint or co-state. This allows to apply local minimization methods like gradient descent to solve the inverse problem. Unfortunately, a clear general and simple introduction into the topic of adjoint

Algorithm 6 Powell-Wolfe Stepsize Rule

```

if  $J(m_k + p_k) \leq J(m_k) + c_1 \nabla J(m_k)^T p_k$  and  $\nabla J(m_k + p_k)^T p_k \geq c_2 \nabla J(m_k)^T p_k$  then
  return  $\gamma = 1$ 
else
  if  $J(m_k + p_k) > J(m_k) + c_1 \nabla J(m_k)^T p_k$  then
    Compute largest  $\gamma_- \in \{2^{-1}, 2^{-2}, \dots\}$  such that  $J(m_k + \gamma_- p_k) \leq J(m_k) + c_1 \gamma_- \nabla J(m_k)^T p_k$ 

    Set  $\gamma_+ = 2\gamma_-$ .
  else
    Compute the smallest  $\gamma_+ \in \{2, 2^2, \dots\}$ , such that  $J(m_k + \gamma_+ p_k) > J(m_k) + c_1 \gamma_+ \nabla J(m_k)^T p_k$ 
    Set  $\gamma_- = \frac{\gamma_+}{2}$ .
  end if
  while  $\nabla J(m_k + \gamma_- p_k)^T p_k < c_2 \nabla J(m_k)^T p_k$  do
    Compute  $\gamma = \frac{\gamma_- + \gamma_+}{2}$ .
    if  $J(m_k + \gamma p_k) \leq J(m_k) + c_1 \gamma \nabla J(m_k)^T p_k$  then
       $\gamma_- = \gamma$ 
    else
       $\gamma_+ = \gamma$ 
    end if
  end while
end if

```

operators is missing in most of the literature. The adjoint approach is frequently employed for sensitivity calculation using the concept of Lagrange multiplier. A good introduction from this perspective can be found in (Hinze, 2009). Although the mathematical formulation being very concise, following this approach often disguises the principle behind adjoint computation such that it often comes as a great surprise that one is able to invert for thousands to millions of parameters at the same time when other methodologies are already struggling with only a few. Moreover, the approach for calculating *sensitivities* is often simply referred as adjoint method in the literature which contributes to the confusion and a more concise description is *adjoint sensitivity state method*. An introduction into the general methodology that is not limited to the sensitivity approach is often missing.

For this reason, this chapter tries to give an introduction into adjoint equations from perturbation theory following the particularly well-written book by Marchuk (Marchuk, 1995). The principles are first introduced for a simple one-dimensional heat transfer problem and then extended to linear operators. Only after the general concept is introduced in sufficient depth, the focus is shifted to the original topic of providing sensitivity information that can be used for the iterative solution of an inverse problem. For this purpose the direct and adjoint approach for this calculation are presented and discussed. It is shown that the computational complexity of the adjoint approach is independent of the number of model parameters which makes it very well suited for inverse problems with distributed parameters. In the end, adjoint formulations are derived for the nonlinear least-squares objective function that is central to this thesis. The redundancy in the theory is not accidental but intended to make the point

that adjoint computations can be simple in both, its understanding and computation.

3.3.1 Adjoint state method

3.3.1.1 Linear algebra

To start with, the adjoint approach is best described in the context of linear algebra. Following Giles (Giles and Pierce, 2000), suppose that a vector $u \in \mathbb{R}^n$ is the solution to a linear equation system

$$Lu = f; \quad J := g^T u, \quad (3.29)$$

for some given matrix $L \in \mathbb{R}^{n \times n}$ and vector $f \in \mathbb{R}^n$. It is often called **main** or **primal equation**. Suppose that the main interest is not directly in u , but we wish to evaluate the quantity $J = g^T u$ where $g \in \mathbb{R}^n$. The direct approach consists in solving 3.29 for u first and then calculating the scalar product $g^T u$. Alternatively, there is another way to compute the value of J , if we are not interested in u itself. The so-called **adjoint** or **dual form** is to evaluate $J = v^T f$ instead, where the adjoint solution $v \in \mathbb{R}^n$ satisfies the linear equation system

$$L^T v = g; \quad J := v^T f. \quad (3.30)$$

Note the use of the transposed matrix L^T and the interchange of the roles of f and g . The equivalence of the two forms is easily proven:

$$J = v^T f = v^T Lu = (L^T v)^T u = g^T u. \quad (3.31)$$

For single vectors f and g nothing would be gained by using the dual form. But if there are p different vectors f_1, \dots, f_p and m different vectors g_1, \dots, g_m then the direct approach means to solve p primal problems and then compute m vector products. The adjoint approach involves m solutions to the adjoint problem and p vector products to calculate J . If the dimension of equation system 3.29 is very large, the cost of the vector products to calculate J is negligible compared to solving the linear equation system, and therefore the adjoint approach is much cheaper when $m \ll p$. Especially, if $m = 1$, meaning that there is only one vector product, and p is very large. In the next section this idea is extended to functionals depending on solutions of partial differential equations.

3.3.1.2 Linear continuous functionals

The short excursion to linear algebra showed that there are two ways to calculate the value of a scalar product of a solution of a linear equation system, the direct and adjoint approach. This is also true for linear continuous functionals that depend on the solution of a PDE like the acoustic wave equation. The problem of being interested in the value of a functional that is depending on the solution of a PDE rather than the solution itself is quite common in many engineering disciplines. To motivate the large application area of adjoint computations, some examples of useful linear functionals are given next. Suppose that we are interested in the value of a linear continuous functional J :

$$J = (u, g) := \int_{\Omega} u(x) \cdot g(x) \, dx. \quad (3.32)$$

Here, u is the solution of a PDE and u, g are elements of $L^2(\Omega) := \{u \mid \int_{\Omega} |u(x)|^2 dx < \infty\}$, and (\cdot, \cdot) denotes a scalar product in $L^2(\Omega)$. g can be chosen in a wide variety of ways. Some examples are given next.

(i) Calculate mean value

If it is required to find a mean value of u over a subdomain $\omega \subset \Omega$, then select $g(x)$ in the form

$$g(x) = \frac{1}{mes\omega} \begin{cases} 1, & x \in \omega, \\ 0, & x \in \Omega \setminus \omega \end{cases} \quad (3.33)$$

In this case the functional will be written in the form

$$J[u] = \frac{1}{mes\omega} \int_{\omega} u(x) dx. \quad (3.34)$$

(ii) Point values

If u is a continuous function, one can choose also the Dirac δ -function as $g(x) : g(x) = \delta(x - x_0)$; then

$$J[u] = \int_{\Omega} u(x) \delta(x - x_0) dx = u(x_0). \quad (3.35)$$

(iii) Acoustics

As a more specific example, in acoustics, the functional J can represent a measurement process that translates a pure physical entity u , such as a pressure wave, to a secondary observable like the energy at a fixed sensor position $x = x_r$. Here, the functional depends on the choice of a parameter set m the pressure wave is depending on. For example, the wave speed inside the domain. Then the functional J is given by the following expression:

$$J[m] = \int_{\Omega} \int_0^T \dot{u}^2(m; x, t) \delta(x - x_r) dt dx. \quad (3.36)$$

As another application, a functional can quantify the discrepancy between a recorded ultrasonic signal and its theoretical prediction $u(m; x, t)$. The functional then plays the role of a misfit functional that quantifies the distance between both signals at $x = x_r$:

$$J[m] = \int_{\Omega} \int_0^T [u(m; x, t) - u_0(x, t)]^2 \delta(x - x_r) dt dx. \quad (3.37)$$

This functional will be revisited in section 3.3.2.4 when the adjoint approach for sensitivity calculations is introduced. Instead of directly focusing on this topic the adjoint approach for linear functionals is first presented in a simpler setting to make the principles clear.

Heat transfer in a bar

Even though this thesis is concerned with acoustic wave propagation, the principles behind adjoint computations are most easily explained by presenting a stationary one-dimensional example. A simple example where all important details are already present is as follows:

Consider a heat transfer problem on $\Omega = [0, 1]$ without convection effects along a bar. As boundary conditions, the temperature is fixed to zero at the beginning and end of the bar. Furthermore an external constant source is applied in some part. The state of the bar is described by a one-dimensional Poisson equation:

$$\begin{aligned} -u_{xx}(x) &= f(x) \\ u(0) &= u(1) = 0. \end{aligned} \tag{3.38}$$

Here, u is the resulting displacement field when load f is applied to the bar. For convenience, the PDE is often written in operator notation using the differential operator $L := -\frac{\partial^2}{\partial x^2}$. The domain of L is defined as

$$D(L) := \{u \mid u(0) = u(1) = 0\}. \tag{3.39}$$

One can write $Lu = f$, where u is assumed to be in $D(L)$ as a shorthand for 3.38. We start by assuming that u is in a Hilbert space, e.g $u \in L_2(\Omega)$ with the following scalar product:

$$(u, v) = \int_0^1 u \cdot v \, dx. \tag{3.40}$$

Applying the differential operator L to u and assuming, for the sake of simplicity, that $u, v \in D(L)$, we can rearrange terms by formally applying integration by parts.

$$(Lu, v) = \int_0^1 Lu \cdot v \, dx = - \int_0^1 u_{xx} \cdot v \, dx \tag{3.41}$$

$$= - u_x \cdot v \Big|_0^1 + \int_0^1 u_x \cdot v_x \, dx \tag{3.42}$$

$$= - u_x \cdot v \Big|_0^1 + u \cdot v_x \Big|_0^1 - \int_0^1 u \cdot v_{xx} \, dx \tag{3.43}$$

$$=: (u, L^*v) \tag{3.44}$$

Both boundary terms vanish because of 3.39. By partially integrating twice, an equivalent formula is found where an operator L^* is acting solely on v . This operator is called **adjoint operator**. Compare this to the operator we started with L , that is acting solely on u . If and only if all boundary terms vanish, the following important formula holds:

$$(Lu, v) = (u, L^*v). \tag{3.45}$$

This formula is called **Lagrange identity**. Despite its simplicity, it is the key to efficient computations. The adjoint operator is constructed by integration by parts and by the definition

	Primal operator	Adjoint operator
Laplace operator	$\nabla \cdot (k\nabla u)$	$\nabla \cdot (k\nabla u^*)$
Heat operator	$\frac{du}{dt} - \frac{d^2u}{dx^2}$	$-\frac{du^*}{dt} - \frac{d^2u^*}{dx^2}$
Convection operator	$\frac{du}{dt} + \frac{du}{dx}$	$-\frac{du^*}{dt} - \frac{du^*}{dx}$
Acoustic wave operator	$\frac{d^2u}{dt^2} - \alpha^2 \frac{d^2u}{dx^2}$	$\frac{d^2u^*}{dt^2} - \alpha^2 \frac{d^2u^*}{dx^2}$

Table 3.1: Primal and adjoint operators for common differential operators

of suitable conditions on its domain. Furthermore, if $L^* = L$, then the operator is called self-adjoint. Therefore, the Laplace operator is self-adjoint.

Table 3.1 shows primal and corresponding adjoint operators for the most common differential operators. As seen before, the Laplace operator and also the wave operator are self-adjoint. In general, when the primal operator contains derivatives of odd degree then the adjoint operator will have the opposite sign in front of these term and will therefore not be self-adjoint. Examples are the heat and convection equation.

Assuming u, v to satisfy the boundary conditions all boundary terms vanish. Suppose that we are not interested in u itself, but in the value of a linear continuous functional J that is depending on u .

$$J[u] = \int_{\Omega} u(x) \cdot g(x) dx, \quad (3.46)$$

where $g(x)$ is a prescribed function from L^2 and $u(x)$ is implicitly given as solution of the state equation

$$\begin{aligned} -u_{xx}(x) &= f(x) \\ u(0) &= u(1) = 0. \end{aligned} \quad (3.47)$$

Furthermore, suppose that $g(x)$ is an instrumental or measurement characteristic, e.g.

$$g(x) = \begin{cases} 1, & 0 \leq \alpha \leq x \leq \beta \leq 1 \\ 0, & \text{otherwise.} \end{cases} \quad (3.48)$$

The instrument associated with g only registers solution values within $\alpha \leq x \leq \beta$ and does not respond to the solution in the other parts of the interval. If we want to evaluate J , we can solve 3.47 for $u(x)$ and then integrate the product $u(x) \cdot g(x)$. Consider the following slightly different problem involving the adjoint operator and the measurement characteristic as its source term:

$$\begin{aligned} -u_{xx}^*(x) &= g(x) \\ u^*(0) &= u^*(1) = 0. \end{aligned} \quad (3.49)$$

This is called the adjoint equation, it is specifically designed for the primal problem and it is tied to functional J under consideration through its source term.

The second key concept to adjoint computation is to use Lagrange identity 3.45 and the adjoint equation to obtain an equivalent adjoint formula for the evaluation of J .

An equivalent formula for 3.46 can be obtained by multiplying the main equation 3.47 by the adjoint solution, the adjoint equation 3.49 by the main solution, taking their difference and integrating over the domain:

$$-\int_0^1 \frac{\partial^2 u}{\partial^2 x} \cdot u^* \, dx + \int_0^1 \frac{\partial^2 u^*}{\partial^2 x} \cdot u \, dx = \int_0^1 f \cdot u^* \, dx - \int_0^1 u \cdot g \, dx. \quad (3.50)$$

First, the sought functional J is found on the right hand side. Second, using Lagrange identity 3.45 the left hand side vanishes. In this simple example we could also see this by integrating one of both terms by part twice and using the boundary conditions that solutions u and u^* satisfy. What remains is the following interesting relationship:

$$\boxed{J[u] = \int_0^1 u \cdot g \, dx = \int_0^1 f \cdot u^* \, dx.} \quad (3.51)$$

This means that, if we are interested in J , then we can compute it by evaluating either of both formulas. The second formula contains u^* , the solution to the adjoint problem 3.49. This is the analogy for 3.31. Both formulas can be used but one proves to be more efficient to the other depending on the use case. Because of it's fundamental importance, let's look at a specific example.

Consider the bar problem with a specific load f :

$$\begin{aligned} -u_{xx}(x) &= f(x) \\ u(0) &= u(1) = 0, \end{aligned} \quad (3.52)$$

with

$$f(x) = \begin{cases} 1, & x \in [0; 0.4] \\ 0, & x \notin [0; 0.4]. \end{cases} \quad (3.53)$$

Now, suppose the interest lies not solely in u but especially in a scalar functional $J[u]$:

$$J[u] = \int_0^1 g(x) \cdot u(x) \, dx \quad (3.54)$$

with

$$g(x) = \begin{cases} 1, & x \in [0.7; 1] \\ 0, & x \notin [0.7; 1], \end{cases} \quad (3.55)$$

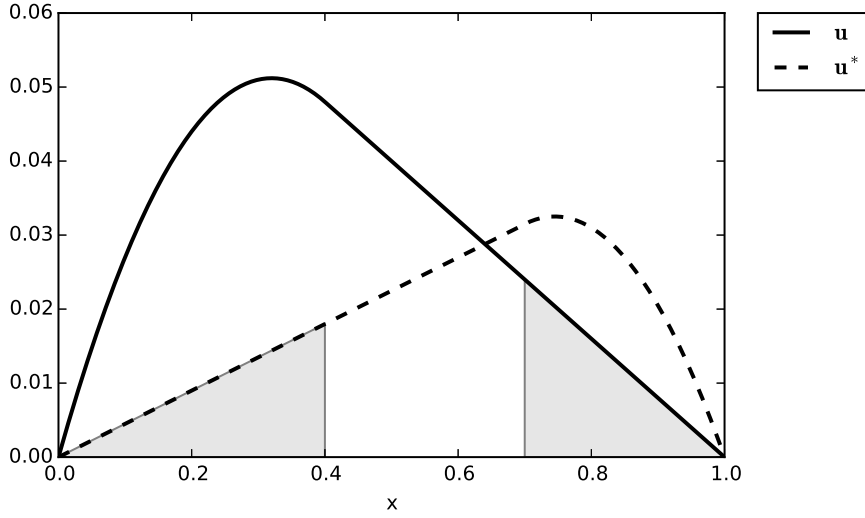


Figure 3.6: Primal and adjoint solutions for bar problem

Formula 3.51 tells us, that we can get the value of the functional computing the solution of an adjoint equation, where the boundary conditions carry over but the instrumental g is acting as adjoint source:

$$\begin{aligned} -u_{xx}^*(x) &= g(x) \\ u^*(0) &= u^*(1) = 0. \end{aligned} \quad (3.56)$$

Fig. 3.6 shows solutions u and u^* for the primal and adjoint problem respectively. The PDE is solved using second order finite differences on a uniform grid with step size $h = 0.01$ and the integration is performed by Simpson's rule. The shaded areas under both curves represent the value of J and are equal by construction. To see the benefits of the adjoint formulation, suppose that the source in the main problem changed and now a solution for the new perturbed problem is needed.

$$\begin{aligned} -u'_{xx}(x) &= f'(x) \\ u'(0) &= u'(1) = 0, \end{aligned} \quad (3.57)$$

with

$$f'(x) = \begin{cases} 1, & x \in [0; 0.5] \\ 0, & x \notin [0; 0.5]. \end{cases} \quad (3.58)$$

The new value of functional J can be calculated using the direct or adjoint formulation:

$$J_g = \int_{0.7}^1 u'(x) \cdot g(x) dx, \quad (3.59)$$

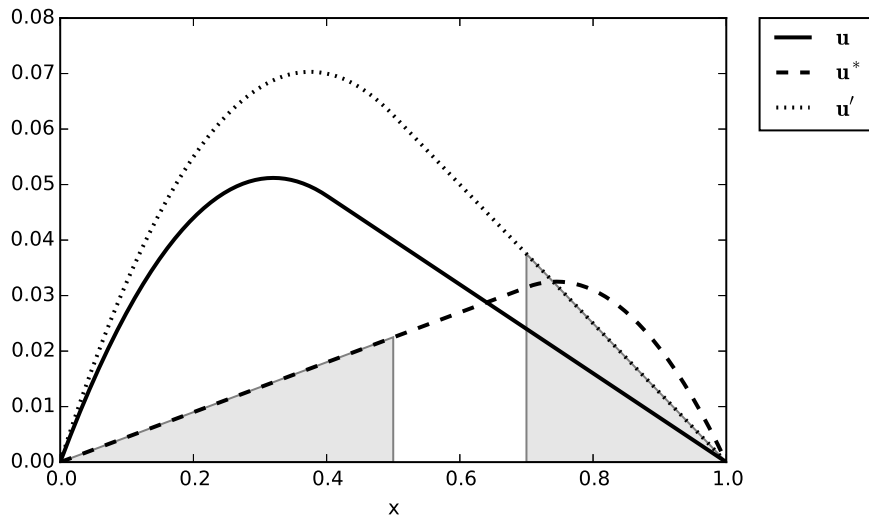


Figure 3.7: Primal and adjoint solutions

$$J_f = \int_0^{0.5} u^*(x) \cdot f'(x) dx. \quad (3.60)$$

Following a direct approach the solution to the new perturbed primal problem u' is needed. Figure 3.7 shows how the solution is affected by changing the source term. As the measurement characteristic did not change, the integration boundaries do not change for J_g . More important, the adjoint solution, which is related to the unchanged adjoint source term g , is **not affected** by the change in the source. The change is only related to its integration boundary. A variation in the source in the main problem is immediately linked with a variation of the functional under study by equation 3.60. There is **no need** to solve perturbed problem 3.57 to calculate J using the adjoint formulation.

Even though, in our case, the propagation of ultrasonic pressure waves is described by the acoustic wave equation, the presented concepts are not limited to this specific type of equation. As it is even simpler to show the concept for a general mathematical model, this is presented first. We follow an introduction by Marchuk (Marchuk et al., 2005).

Consider a general mathematical model of some physical process governed by the following equation, which is often called **state** or **primal equation**

$$Lu = f, \quad (3.61)$$

where L is a linear operator acting on some Hilbert space H with its domain $D(L)$ dense in H , $f \in H$. Assume that we need to compute not u itself but a linear functional of u :

$$J_g[u] = (u, g), \quad (3.62)$$

where g is an element of H , and (\cdot, \cdot) denotes a scalar product in H . The design of 3.62 is quite general for linear and continuous functionals due to Riesz representation theorem¹. Examples

¹If $x \in H$, every continuous linear functional $J : H \rightarrow \mathbb{R}$ can be written uniquely as $J_x[y] = (y, x) \quad \forall y \in H$. See (Werner, 2007)

for common functionals were given in section 3.3.1.2.

We introduce the new adjoint operator L^* with the domain $D(L^*)$ satisfying the Lagrange identity:

$$(Lh, l) = (h, L^*l), \quad h \in D(L), \quad l \in D(L^*), \quad (3.63)$$

where $D(L^*) = \{l \in H : |(Lh, l)| \leq c\|h\|, c = \text{const}, h \in D(L)\}$ and $\|l\| = (l, l)^{1/2}$. Using the adjoint operator, formulate a nonhomogeneous **adjoint equation** related to the functional:

$$L^*u_g^* = g, \quad (3.64)$$

where g is an element of H defining the functional $J_g[u]$. The equation is also called **co-state equation**. An equivalent formula for 3.62 can be obtained by multiplying the main equation by the adjoint solution, the adjoint equation by the main solution, taking their difference and integrating over the domain

$$(Lu, u_g^*) - (u, L^*u_g^*) = (f, u_g^*) - (u, g). \quad (3.65)$$

Using Lagrange identity 3.63, we get

$$(f, u_g^*) - (u, g) = 0. \quad (3.66)$$

Then

$$J_g[u] = (f, u_g^*). \quad (3.67)$$

Thus, if we need to find the value of the functional 3.62, we can get it in two ways:

- (i) The classical way uses state equation 3.61 to relate the physical process u to source f and then to the functional J_g by equation 3.62.
- (ii) Using the equivalent formula 3.67 changes in f are directly related to changes in the functional J_g .

The direct approach is preferable, when the state u of the physical process is needed. However, if only the value of the functional for a lot of different source terms is needed, then formula 3.67 allows to directly relate the changed source to the change in the sought for functional without considering the physical process described by 3.61 by utilizing the specifically designed adjoint problem in 3.64. This means that a second PDE has to be solved (and its solution stored) for each needed functional. Usually one of these two approaches outperforms the other depending on the use case. If there is only one functional and therefore only one related adjoint problem, then the adjoint approach is clearly preferable. Another use case is the appearance of a very complex source term in the main problem that makes it hard to solve. If g is simple then the adjoint approach is preferable. The approach is also very useful for sensitivity analysis and optimal control statements being discussed later. In structural engineering the concept of influence functions and Betti's theorem are important applications of adjoint computations (Hartmann and Katz, 2002).

It has to be mentioned that the adjoint approach relies on a unique solution of the adjoint equation. If and only if a solution exists there is an adjoint formulation of the functional. For the wave equation the self-adjointness of the operator and that boundary conditions are inherited from the forward problem help to ensure the solvability of the adjoint problem. See (Chavent, 2009) for some remarks on this.

Furthermore, it should be mentioned that in the case of changing source terms the commonly used approach is to store an LU decomposition of the discretized main problem and perform a forward and backward substitution to get the new solution. This is one possible reason why adjoint formulations are not common for the use case of changing loads. In the next section the adjoint approach is applied to the computation of **sensitivities of functionals**. This is where the method really shows its strength.

3.3.2 Adjoint sensitivity state method

In problems that typically stem from stability analysis, parameter estimation and data assimilation one is interested in sensitivity information of a certain model or functional of its solution to a large amount of parameters. It is in these cases that an adjoint approach is the only suitable way to get this information in acceptable time. Optimization problems become computationally practical through adjoints. In fact, the efficient computation of gradient information is a special case of the general adjoint approach. Here, the approach is applied to a linear functional that is representing the sensitivity of the functional to the parameters of the underlying model. It is used in engineering disciplines ranging from computational fluid dynamics (Giles and Pierce, 1997; Pironneau, 1974) and shape optimization (Bletzinger et al., 2010; Bletzinger and Maute, 1997; Bletzinger and Ramm, 2014; Bletzinger et al., 2005; Gauger, 2002; Newman III et al., 1999; Othmer, 2014) to machine learning, training of neural networks and especially full waveform inversion in seismology. For general tutorials on the adjoint sensitivity state method see (Errico, 1997; Marchuk, 1995; Yedlin and Van Vorst, 2010) and introductions from a mathematical perspective are given in (Cao et al., 2002, 2003; Giles et al., 2003; Giles and Pierce, 2000; Haber et al., 2012). The section follows a recent publication of Marchuk (Marchuk et al., 2005) from a standpoint of perturbation theory. For the interested reader, a general introduction using the Lagrange multiplier approach that is more common in the literature of sensitivity calculations can be found in (Hinze, 2009) and in appendix A. For great reviews in the seismology community consider (Fichtner, 2011; Fichtner et al., 2013; Plessix, 2006; Virieux and Operto, 2009).

3.3.2.1 Problem formulation

Consider again the general setting, where the value of a linear continuous functional J is considered to be of the following form

$$J(m) = \int_{\Omega} u(m; x) \cdot g(x) dx, \quad (3.68)$$

where $u(m; x)$ is given by a general mathematical model of some physical process governed by the equation

$$L(m)[u(m; x)] = f(x), \quad (3.69)$$

which is depending on some model parameters m over the operator L of the state equation. Model parameters m might be material distribution, source parameter or related to initial conditions. Then, the sensitivity of J with respect to these parameters is given by another linear functional $\frac{\partial J(m)}{\partial m}$:

$$\frac{\partial J(m)}{\partial m} = \int_{\Omega} \frac{\partial u(m; x)}{\partial m} \cdot g(x) dx. \quad (3.70)$$

This is again a linear continuous function in the form considered in the general adjoint approach and it can be used to efficiently calculate the sensitivity of a functional where its evaluation is implicitly depending on the solution of a PDE. This is the common setting for inverse problems where a descent direction like the negative gradient is needed for a local optimization method. Here, the number of design variables can be very large, because parameters might be mesh dependent, for instance one variable per grid point in a large 3D FEM mesh leading to $O(N)$ design variables. This can easily result in 10^6 to 10^9 design variables that have to be considered for the inversion.

An obvious possibility to calculate the sensitivity of the functional is to use finite differences as described in Sec. 2.2. For example, using forward differences of first order, one can approximate the gradient by:

$$\frac{\partial J(m)}{\partial m_i} \approx \frac{J(m_1, \dots, m_i + h, m_{i+1}, \dots, m_N) - J(m_1, \dots, m_i, \dots, m_N)}{h}, \quad i = 1, \dots, N. \quad (3.71)$$

This would require N additional evaluations of J . As every evaluation of J corresponds to one additional solution of the state equation and this is clearly impractical for large N . Therefore, other approaches are needed. The direct and adjoint approach for sensitivity calculations are considered next.

3.3.2.2 Forward Sensitivity State Method

The sensitivity or direct method explicitly calculates the sensitivity of the model to parameter changes. Instead of the unperturbed problem

$$Lu = f, \quad (3.72)$$

consider a new perturbed problem:

$$Lu' = f', \quad (3.73)$$

where $f' = f + \delta f$, $\delta f \in H$. Due to the linearity of the unperturbed problem, its solution may be represented in the form:

$$u' = u + \delta u, \quad \delta u \in D(L). \quad (3.74)$$

Then, using both representations for variations of a functional in the formula $J'_g = J_g + \delta J_g$, we obtain two equivalent relationships:

$$\delta J_g = (\delta u, g), \quad (3.75)$$

$$\delta J_g = (\delta f, u_g^*). \quad (3.76)$$

where u_g^* is a solution of the unperturbed adjoint problem often referred to as *importance function* (value function), or as *influence function*. It is the function that is responsible for the sensitivity of the functional J_g to the source function f . If the right-hand side depends on some parameter m_i , from the last equation we get the formula for variations:

$$\delta J_g = \frac{\partial J_g}{\partial m_i} \delta m_i = \left(\frac{\partial f}{\partial m_i}, u_g^* \right) \delta m_i. \quad (3.77)$$

Then the sensitivity to changes in the source is given by

$$\frac{\partial J_g}{\partial m_i} = \left(\frac{\partial f}{\partial m_i}, u_g^* \right). \quad (3.78)$$

The value of $\partial J_g / \partial m_i$ therefore shows how sensitive the functional J_g is to variations of the parameter m_i . Now, assume that the operator itself depends on some set of parameters m :

$$L(m)u = f, \quad u \in D(L), \quad f \in H, \quad (3.79)$$

and it is required to study the sensitivity of the functional

$$J_g[u] = (u, g), \quad g \in H \quad (3.80)$$

to variations of the parameters m . Along with the unperturbed problem, consider the perturbed one:

$$L(m')u' = f, \quad (3.81)$$

where $m' = m + \delta m$, $u' = u + \delta u$, $\delta u \in D(L)$. Let $L(m)$ be sufficiently smooth in m , such that

$$L(m + \delta m) = L(m) + \frac{\partial L}{\partial m} \delta m + O((\delta m)^2), \quad (3.82)$$

where $\partial L / \partial m$ is the derivative of L defined by the equality (on condition that the limit exists)

$$\lim_{t \rightarrow 0} \frac{L(m + t\delta m) - L(m)}{t} = \frac{\partial L}{\partial m} \delta m. \quad (3.83)$$

Substituting equations 3.81 and 3.82 yields:

$$\left(L(m) + \frac{\partial L}{\partial m} \delta m \right) (u + \delta u) = f \quad (3.84)$$

$$L(m)u + L(m)\delta u + \frac{\partial L}{\partial m} u \delta m + \frac{\partial L}{\partial m} \delta u \delta m = f \quad (3.85)$$

Using equation 3.79 and restricting ourselves to first-order terms, we get

$$L(m)\delta u = -\frac{\partial L}{\partial m}u\delta m. \quad (3.86)$$

This is the principle equation for determining small variations of its solution from the unperturbed state. It is often called **sensitivity equation**. Again, there exist two approaches to evaluate the variation of a linear functional that is depending on its solution δu

$$\delta J_g = (\delta u, g). \quad (3.87)$$

The *direct approach* is to first evaluate 3.86 and then use this solution in 3.87 to calculate $\frac{\partial J}{\partial m_i}$. It is also called *sensitivity approach* as one can use model 3.86 directly to determine the impact of perturbations and therefore estimate the sensitivity of the model. For a large number of parameters m_i , $i = 1, \dots, N$ this would require N solutions to 3.86, which is clearly impractical for very large N . A more efficient and direct way is to use adjoints instead, which is the topic of the next section.

3.3.2.3 Adjoint Sensitivity State Method

Instead of using the sensitivity equation directly one can consider the adjoint problem tied to functional δJ_g as shown in equation 3.76:

$$L^*(m)u_g^* = g. \quad (3.88)$$

We can use the adjoint solution to calculate the value of the variation

$$\delta J_g = -\left(\frac{\partial L}{\partial m}u\delta m, u_g^*\right).$$

The value

$$\frac{\partial J_g}{\partial m} = -\left(\frac{\partial L}{\partial m}u, u_g^*\right) \quad (3.89)$$

provides information about the sensitivity of the functional J_g . How much do changes of m affect J_g ? This value is determined by the adjoint function u_g^* . As the adjoint formulation of the functional directly relates changes in the parameter to changes in the functional without the necessary knowledge of changes in the state, it is not necessary to solve for the sensitivity for each parameter. The adjoint variant is numerically very attractive as only one extra solution of the adjoint problem is necessary. The costs are almost independent of the number of model parameters.

3.3.2.4 Acoustic misfit formulation

For many applications it is typical to look at the misfit between synthetics and measured data. For instance, in seismology the misfit between synthetics and measured data at seismometers is considered. The acoustic wave equation $L(m)u = f$ is given by

$$u_{tt}(x, t) - m(x)\Delta u(x, t) = f_s(x, t) \text{ for } x \in \Omega \subset \mathbb{R}^2 \text{ or } \mathbb{R}^3, t \in [0, T], \quad (3.90a)$$

$$u(x, 0) = u_t(x, 0) = 0 \text{ on } \Omega, \quad (3.90b)$$

$$u = 0 \text{ on } \partial\Omega. \quad (3.90c)$$

As model parameters $m(x) := v_p^2(x)$, the squared propagation speed of compression waves is chosen. For N sensors that record the seismic wave field, the misfit is formulated as the following scalar least-squares functional:

$$J(m) = \frac{1}{2} \int_{\Omega} \int_0^T \sum_{i=1}^N [u(m, x, t) - u_0(x, t)]^2 \cdot \delta(x - x_i^r) dt dx,$$

where $u(m; x_i^r, t)$ is the predicted and $u_0(x_i^r, t)$ the observed ultrasonic signal for sensor r . The sensitivity functional to variations δm in the model parameter is given by the following formula:

$$\frac{\partial J(m)}{\partial m} = \int_{\Omega} \int_0^T \sum_{i=1}^N [u(m, x, t) - u_0(x, t)] \cdot \delta(x - x_i^r) \cdot \frac{\partial u}{\partial m} dt dx.$$

If we are interested in the sensitivity of the least-squares misfit functional to variations δm in the model parameter, then we can compute this value either using the direct approach or using the adjoint approach as described before with measurement characteristic $g = \sum_{i=1}^N [u(m, x, t) - u_0(x, t)] \cdot \delta(x - x_i^r)$ and the self-adjointness of the wave equation. Then the related adjoint problem is given by the following PDE:

$$u_{tt}^*(x, t) - m(x)\Delta u^*(x, t) = g(x, t) \text{ for } x \in \Omega \subset \mathbb{R}^2 \text{ or } \mathbb{R}^3, t \in [0, T], \quad (3.91a)$$

$$u^*(x, T) = u_t^*(x, T) = 0, \text{ on } \Omega, \quad (3.91b)$$

$$u^* = 0 \text{ on } \partial\Omega. \quad (3.91c)$$

The time-reversed adjoint has an interesting interpretation in the context of the wave equation (Virieux and Operto, 2009). Its source term is the residual: the difference between synthetics and recorded data in reverse time. The equation propagates the residual into the structure starting from final time T . Its solution $u^*(x, T - t)$ is called backpropagated field of residuals. Using the solution to the adjoint problem, the computation of $\frac{\partial u}{\partial m_j}$ for every parameter m_j can be circumvented using the adjoint representation of the functional

$$\frac{\partial J}{\partial m} = -(\Delta u, u^*). \quad (3.92)$$

Solving the adjoint equation once, it is possible to compute the sensitivity of functional J for **all** model parameters. This is especially true for a distributed parameter that is varying in space like the compression wave propagation speed $v_p(x)$. This clearly shows the tremendous benefits of the adjoint formulation in this particular setting.

3.3.3 Summary

This chapter gave an introduction into the adjoint state method following perturbation theory. If the interest lies in the value of a functional that depends on a physical state that is described by a PDE then there are two ways to evaluate the functional: the forward way consists of solving the state equation (the PDE) first and then calculating the value of the functional. If the primal nonlinear solution is smooth, the adjoint approach means that a second PDE describing an adjoint state can be formulated (Giles and Ulbrich, 2010a,b). It is tailored to

the functional by its source term. If a solution to the adjoint state equation exists, it can be used to evaluate the functional without the knowledge of the solution to the state equation. It was shown that the later approach allows to calculate the sensitivities of a misfit functional that depends on the acoustic wave equation to changes in the distributed wave propagation speed very efficiently. Only two PDEs need to be solved to calculate the gradient of the misfit functional. This provides the local information needed for gradient-based minimization algorithms considered in this thesis. The next chapter discusses how the adjoint sensitivity state method and local optimization schemes are used for full waveform inversion.

3.4 Summary of the algorithm

After the the necessary fundamentals have been presented in the last chapters, the algorithm is summarized in Fig. 3.8.

Starting with an initial model $v_p(x)$ for the wavespeed of the unflawed structure, a forward modeling generates simulated sensor measurements. With L-BFGS an advanced gradient-based minimization procedure is used to minimize the misfit between the experimental measurements of the flawed specimen and the simulated measurements

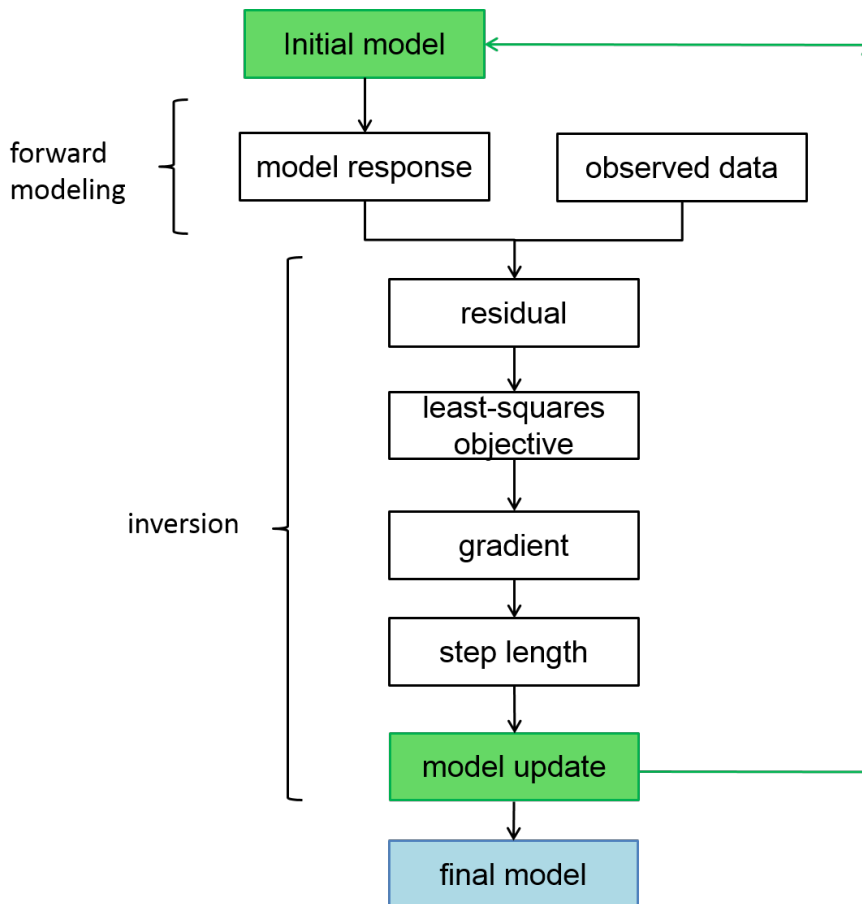


Figure 3.8: Full waveform inversion process

$$J(m) = \frac{1}{2} \int_{\Omega} \int_0^T \sum_{i=1}^{N_s} [u(m; x, t) - u_0(x, t)]^2 \cdot \delta(x - x_i^r) dt dx.$$

The idea is to iteratively improve the initial velocity model of the unflawed structure to generate measurements that are similar to the experimental measurements. The optimization parameters are chosen as $m(x) := v_p^2(x)$. Here, the simulated measurements are generated solving the acoustic wave equation.

$$\begin{aligned} u_{tt}(x, t) - v_p^2(x) \Delta u(x, t) &= f_s(x, t) \text{ for } x \in \Omega \subset \mathbb{R}^2 \text{ or } \mathbb{R}^3, t \in [0, T] \\ u(x, 0) = u_t(x, 0) &= 0, \text{ on } \Omega \\ u &= 0 \text{ on } \partial\Omega \end{aligned}$$

Inversion. The residual of simulated and observed experimental data is computed and the value of the least-squares objective evaluated. The necessary gradient of the high-dimensional objective is calculated with the help of the solution to the adjoint equation $u^\dagger(x, t)$.

$$\nabla_m J(m) = - \int_{\Omega} \int_0^T \Delta u(x, t) \cdot u^\dagger(x, t) dt dx. \quad (3.94)$$

The source term of the adjoint problem consists of the difference between synthetics and recorded data in reverse time. The equation propagates the residual into the structure starting from final time T .

$$\begin{aligned} u_{tt}^\dagger(x, t) - v_p^2(x) \Delta u^\dagger(x, t) &= f_s^\dagger(x, t) \text{ for } x \in \Omega \subset \mathbb{R}^2 \text{ or } \mathbb{R}^3, t \in [0, T] \\ u^\dagger(x, T) = u_t^\dagger(x, T) &= 0, \text{ on } \Omega \\ u^\dagger &= 0 \text{ on } \partial\Omega \end{aligned}$$

where

$$f_s^\dagger(x, t) := \sum_{i=1}^N [u(m; x, t) - u^0(x, t)] \delta(x - x_i^r).$$

Following the calculation of the gradient, the L-BFGS method as described in Alg. 6 is employed to find a suitable step size γ_k . The design parameters are updated by

$$m_{k+1} = m_k - \gamma_k H_k \nabla J(m_k),$$

where H_k is an approximation of the inverse Hessian. The gradient and function information of the last m iterations are stored to update the approximation following algorithm 5. This procedure is repeated until a local minimum is reached:

$$\|\nabla J(m_k)\| < \epsilon \cdot \|\nabla J(m_0)\|, \text{ where e.g. } \epsilon = 10^{-5},$$

The final velocity model visualizes flaws and inclusions as changes in the wave speed and shows details like position, orientation and shape of the flaws.

Both, time reversal and the sensitivity kernel method can be identified as essential building blocks of full waveform inversion for the calculation of the gradient of the high-dimensional cost function.

Having formulated full waveform inversion, its application to US NDT is verified and validated next.

Chapter 4

Applications

The proposed method is applied for the inspection of flawed structures on a variety of examples. Firstly, a flawed (synthetic) aluminum plate is investigated. Because there is only a small number of sources and receivers available in typical US NDT applications, the number of sensors and sources needed for a successful identification of different flaws is investigated. Secondly, the identification of reinforcement in concrete is explored as an application where a look inside a solid is possible employing full waveform inversion. Thirdly, a validation of the suitability of the method is performed using experimental data. Here, the inversion recovers the thickness of an aluminum plate with a manufactured defect using guided ultrasonic waves.

4.1 Aluminumplate: Studies

In this section, the proposed inversion method is applied to detect a flaw in a simulated aluminum plate. Part of the results have been published by the author in (Seidl and Rank, 2016). Both, the plate and the flaw are idealized in the following way: The plate is assumed to be a two-dimensional rectangular domain of dimensions 100 mm x 200 mm. All boundaries are considered rigid. An ultrasonic point source is applied on the plate to scan the specimen. It is modeled as a Ricker wavelet pulse with a dominant frequency of $f_0 = 200$ kHz:

$$f_s(x, t) = f_0^2 \cdot (t - t_0) \cdot \exp(-f_0^2 \cdot (t - t_0)^2) \cdot \delta(x - x_0), \quad (4.1)$$

where t_0 is the delay and x_0 the position where the point source is applied. The propagation of pressure waves is modeled by the acoustic wave equation. Experimental sensor data is emulated using a second simulation model. In it, a flaw is modeled as a small region where the wave speed model deviates from the background wave speed of aluminum of $v_p = 6420 \frac{m}{s}$. Due to the lack of experimental data, a smaller wavespeed is assumed for the flaw, modeled by $v_f = 0.7v_p$. Moreover, 2 % Gaussian noise is added to the sensor data to emulate measurement errors and to avoid an inverse crime to some extent. The wave propagation of the pulse is modeled for a time span $\Delta T = 48 \mu s$.

Finite differences in space and time, with accuracy orders of $O(\Delta x^4)$ and $O(\Delta t^2)$ respectively and an explicit time stepping scheme as described in Sec. 2.2, are used for the numerical solution of the underlying forward and adjoint wave propagation problems. The spatial discretization of the plate is one gridpoint per mm^2 . It is chosen fine enough to be able to resolve different flaws. The simulation time is discretized by 1000 timesteps which are chosen to satisfy the CFL

condition. The fine temporal sampling is used to generate a good resolution of the smooth source signal with approximately 30 gridpoints per dominant wavelength. The simulation time span is chosen in such a way that the wavefront moves at least once through the complete domain. The discretization results in 20 000 parameters for the adaptable wave speed. Full waveform inversion is performed for 20 iterations employing L-BFGS using the gradients of the last five iterations to approximate the Hessian. The stepsize selection is based on the Wolfe conditions.

By a perfect inversion, material characterization and material identification could be achieved. One important question to answer is: *Given the typically very limited amount of sensors and sources in US NDT experiments, is it possible to enhance the resolution of the imaging by putting more effort on the simulation side?*

Additionally, it is very important to investigate the effect of different choices of environmental parameters on the solution of the inverse problem. Therefore the next paragraphs investigate this for the following cases:

- (i) number of sensors
- (ii) number of sources
- (iii) source frequency
- (iv) source signal
- (v) actuator sensor mode
- (vi) noise study.

4.1.1 Number of sensors

In many practical cases – in particular in NDT for solid structures – it is not possible to place sensors in the interior of a body. Therefore, the following investigations restrict sensor positions to the boundary of the structure. In these experiments, only partial information of the wavefield is captured by the misfit where one sensor is placed at every grid point on the boundary of the domain, leading to 600 sensors in total. The first column in Fig. 4.1 shows four test cases that only differ in the flaw orientation. The position of the source is indicated by a black circle. Black boxes on boundary layers indicate that the complete boundary is equipped with sensors. The red area corresponds to a wave speed of 4800 m s^{-1} and the background to a wave speed of aluminum of 6420 m s^{-1} . Full waveform inversion is run for at most 20 iterations and stopped when a (local) minimum is reached in all cases. In the initial model a homogeneous aluminum plate is assumed. The right column of Fig. 4.1 shows the results obtained by the optimization. The flaw, its position, dimension and orientation is clearly visible. Due to the simultaneous update of all wave speed parameters in every iteration, some artificial noise is introduced in regions where the wave speed of the true model did not change.

Fig. 4.2a shows a typical evolution of the misfit with a steep slope in the first iterations and a vanishing slope in later ones. Fig. 4.2b shows the initial, the adapted and the target signal at one sensor¹. By changing the wave speed in the model the signal of the initial homogeneous

¹sensor 4 (top,right position for ten sensor setup) after the jointed inversion for sources at position A,B and C

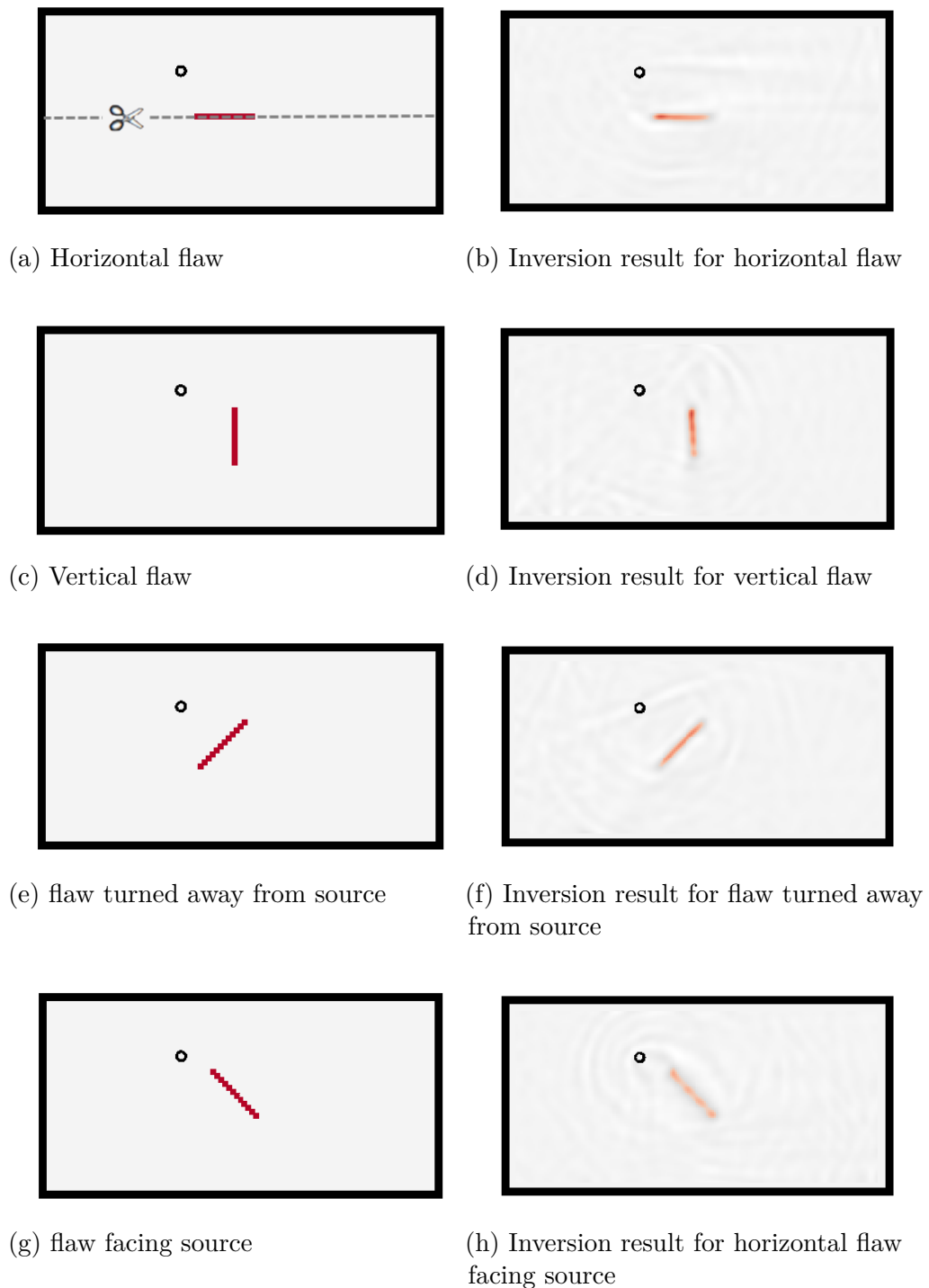


Figure 4.1: The different test cases for the flaw detection algorithm. The US source is depicted by a black circle. The flaw is shown in red. Left: Unknown flaw, Right: Inversion result

model is adapted such that it agrees with the signal of the unknown target model. The misfit is reduced by two orders of magnitude which is typically a good sign for a successful inversion.

Up to now, it was assumed that there is complete information available on the boundary.

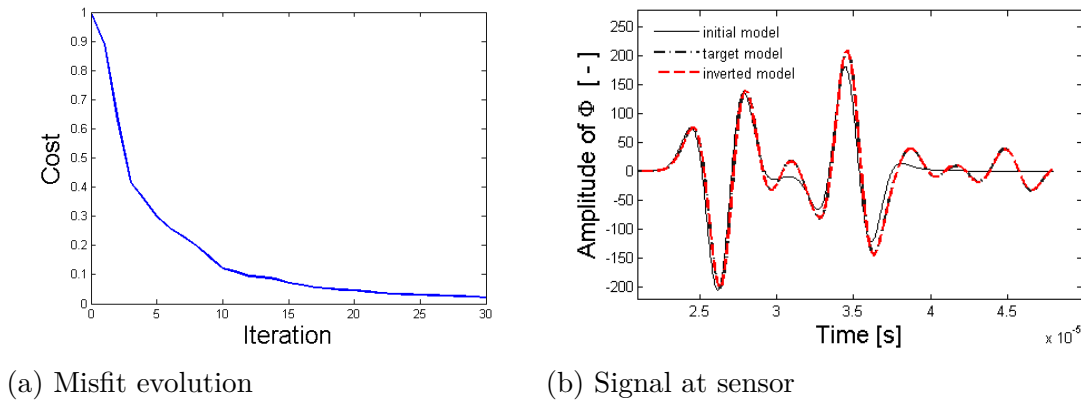
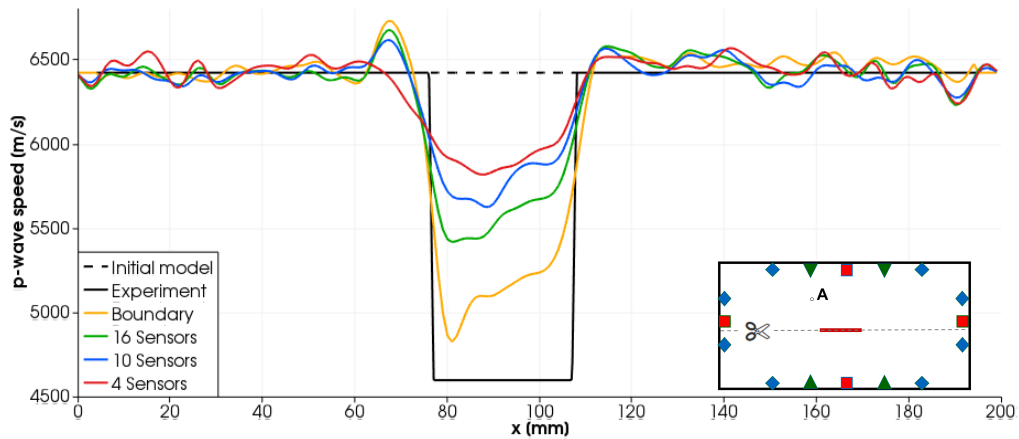


Figure 4.2: General inversion results

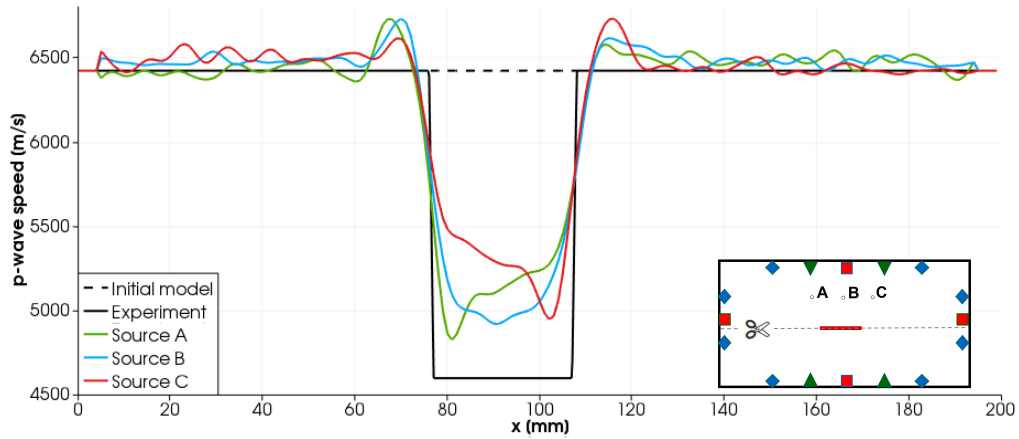
This assumption of placing one sensor at every boundary grid point resulted in an unrealistically large number of sensors. Further investigations are restricted to the horizontal flaw in test case 4.1a.

The next study investigates how the quality of the inversion changes when the number of sensors is reduced to a more realistic amount. In a first computation, 16 sensors are placed on the boundary as shown on the right in Figure 4.3a. In a second computation, only ten sensors are used – indicated by green diamonds and the two red sensors on the top and bottom. A third experiment uses only the four red sensors. Figure 4.3a shows the resulting wave speed field cutting through the horizontal flaw, as indicated by the scissors symbol. This allows the comparison of the quality of the inversions. The flaw is clearly visible in all test cases, even though the inversion did not lead to a perfect inference of the unknown wave speed parameters. Furthermore, the results indicate that the accuracy of the inversion depends not only on the number and positioning of the sensors but also on the source location, as the inversion is more suitable in identifying the closest edge of the flaw. To verify this, the same ultrasonic pulse is applied in the next computation, but its position is varied from position A over B to C as shown in Figure 4.3b.

Comparing the results from varying the source position with the true wave speed model, the following details are observed. First, the quality of the inversion results clearly depends on the positioning of the source relative to the unknown flaw location. In position A, the US pulse is more accurate in identifying the left part of the flaw. When the source is positioned in such a way that there are strong reflections of the waves from the complete flaw, as is the case when placing the source at position B, the inversion is more able to grasp the homogeneity and dimension of the flaw. If the source is positioned further to the right, only the right tip of the flaw is found to give an almost correct wave speed model. Therefore, the source position is crucial for the inversion success. This observation is a major drawback that will be addressed later. Additionally, decreasing the number of sensors clearly decreases the inversion quality. At a first glance, these are rather unpromising results for realistic cases. Here, the key is recognizing that the more information available concerning the misfit, the better the inversion results will turn out. This is the topic of the next section.



(a) One source



(b) Varying source position

Figure 4.3: Cut through crack for various sensor setups.

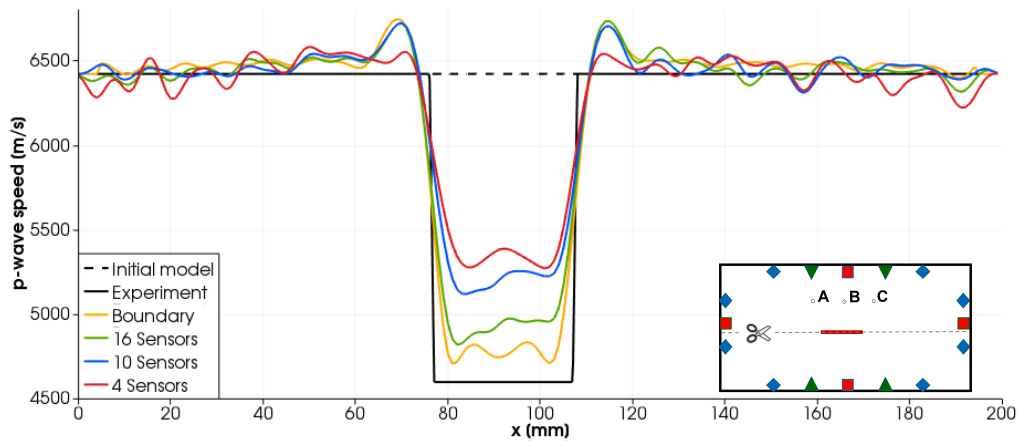
4.1.2 Number of sources

Previously, it was shown that the quality of the inversion strongly depends on the position of the source with respect to the flaw location. Because the flaw position is not known a priori, a possible approach to reduce this dependence is to perform multiple experiments with varying source positions. If a sequence of experiments is performed with K different source positions, this will lead to a generalized misfit functional.

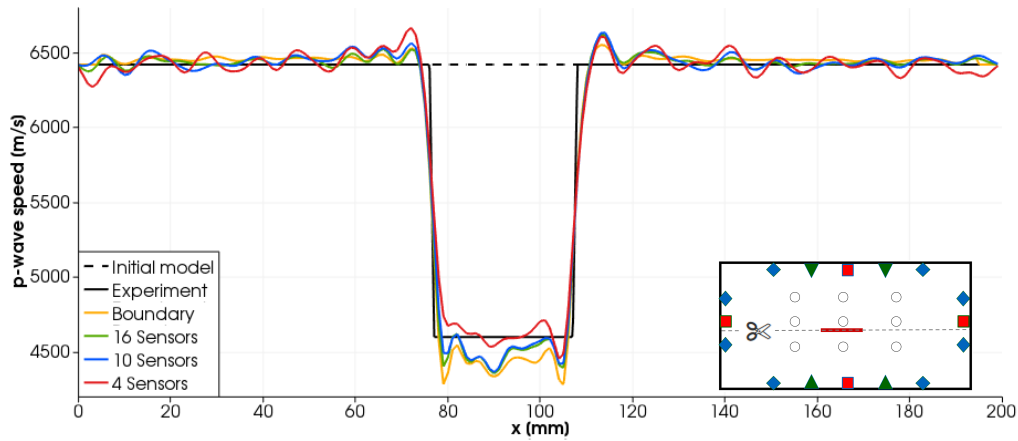
$$\chi(m) = \frac{1}{2} \sum_{k=1}^K \sum_{i=1}^{N_s} \int_{\Omega} \int_0^T [u(m, s_k; x, t) - u^0(s_k; x, t)]^2 \delta(x - x_i^r) dt dx \quad (4.2)$$

In many practical applications piezoelectric transducers are used to excite and sense the waves. In this case, performing multiple experiments, i.e. using multiple source positions, can be easily done as each transducer can be run in “actuator and sensor mode” due to the reversibility of the piezoelectric effect.

In the next computation, the setup is the same as before, except that three experiments are combined in a larger minimization where the source position is varied from position A over



(a) Inversion results for combining three experiments



(b) Inversion results for combining nine experiments

Figure 4.4: Cut through crack combining multiple experiments.

position B to position C. To inspect the quality of the inversion, the cut through the flaw is again used. Figure 4.4a shows the results in this scenario. The wave speeds are clearly closer to the true values, and all choices of sensors provide sufficient information on flaw position, dimension and orientation, even in the case of only four sensors. Especially the dimension of the flaw is recovered well in all computations. In the case of complete boundary measurements, even the wave speed in the flaw is captured correctly. This shows that the inversion results can be improved by adding new experiments even if only few sensors are available. Nevertheless, if less sensors are used there is a decrease in accuracy, and the noise around the flaw increases.

To inspect the influence of additional sources, the next experiment is set up like the previous one, but with six additional sources. Again, all four boundary cases are considered. The setup and inversion results are shown in Figure 4.4b. In all cases, the flaw is reconstructed almost perfectly. The results reveal all important details about flaw location, dimension and orientation. Clearly, the combination of additional experiments leads to a steady increase in the accuracy of the inversion.

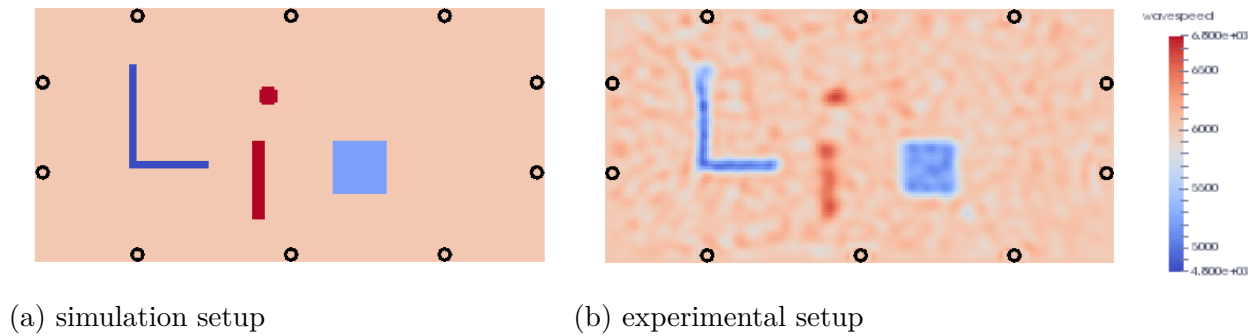


Figure 4.5: Inversion for multiple flaws with different wavespeed

4.1.2.1 Actuator Sensor Mode

This very promising result can be easily adapted in every day NDT practice. Here, sensors can be used either as actuator (source) or sensor. So it is reasonable to use each sensor as source once and let each other sensor record the impulse in a round-robin fashion. This way it should be possible to increase the imaging of flaws using the same setup in the lab. This comes at the price of additional simulation costs per added experiment. Figure 4.5 shows an example using the actuator-sensor mode of ten boundary sensors to invert for an unknown complex speed model with flaws of different wave speed. Figure 4.5a shows the unknown initial model. It consists of four flaws of different shape, dimension and wavespeed. The inversion results running BFGS for 20 iterations are shown in Fig. 4.5b. Here, a Ricker wavelet source with dominant frequency of 150 kHz was used. All flaws with their different wavespeeds and dimensions are clearly reconstructed. This example shows some of the benefits of full waveform inversion compared to simpler methods like time-reversal and topological energy method. Flaws of different sizes that might be small (and around wavelength) or larger than the wavelength can be detected simultaneously using only ten sensors.

4.1.3 Source frequency

For the rest of this study, we focus on this complex inversion example. A classical result from refraction theory is that only objects in the order of the wavelength of the source can be inferred. This is especially true for time-reversal methods. In the next study, the influence of the source frequency is studied in detail. All parameters are chosen as before, only the dominant frequency of the Ricker wavelet is varied from 50 kHz to 100 kHz and 200 kHz. With a background wavespeed of $v_p = 6020 \text{ m s}^{-1}$ this leads to associated wave lengths of 12 cm, 6 cm and 3 cm. Fig. 4.6 shows the results of the inversion. Fig. 4.6b shows the results for 50 kHz. For illustration, the wavelength of the source impulse in the medium is plotted in each plot. Using the source with lowest frequency the flaws are still recognizable but smeared out (in the order of the wavelength). Increasing the wavelength to 100 kHz leads to a clear and better reconstruction of the sharp features and a better contrast of the background. The results are shown in Fig. 4.6c. Increasing the frequency further to 200 kHz, the connection of the structures is not as clear as in the reconstructions before, as shown in Fig. 4.6d. It is hard to decide if there are connected structures or noise. Nevertheless, the area of all four flaws is still clearly detectable. In summary, this shows that the resolution of the inversion is limited

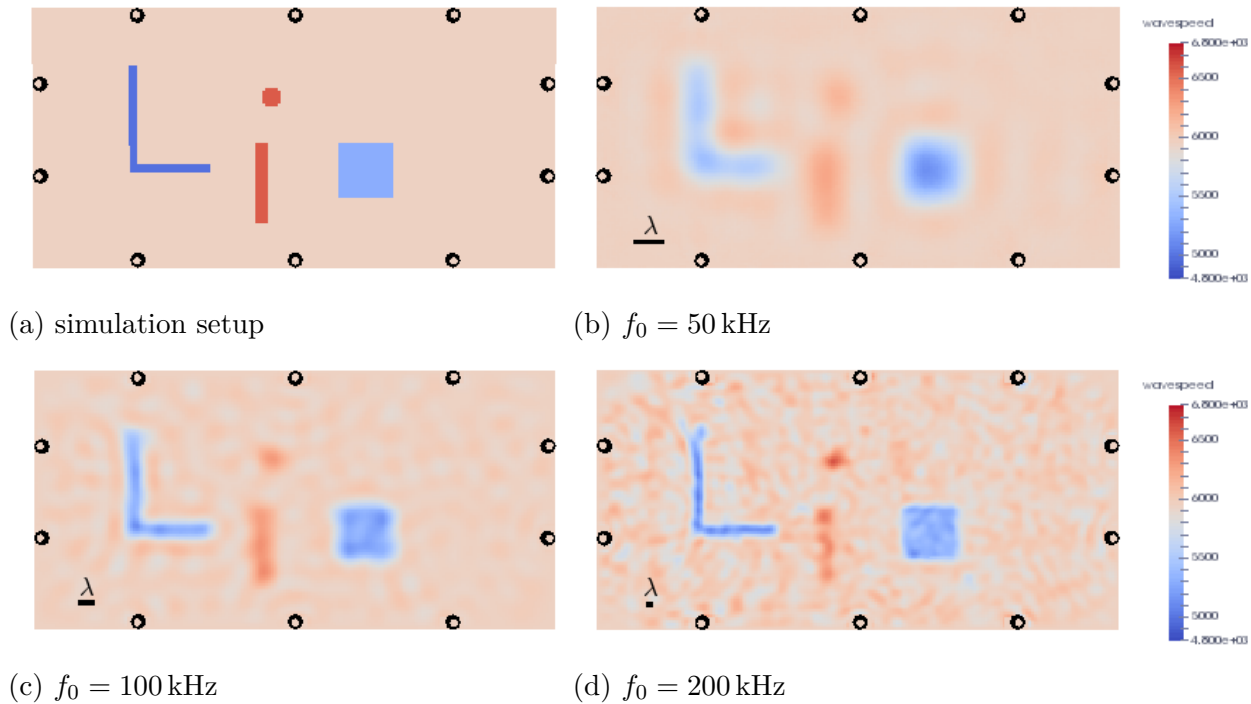


Figure 4.6: Inversion for sources with different frequencies

by the wavelength of the source signal and its frequency has to be chosen carefully to allow a good reconstruction quality.

4.1.4 Source signal

Clearly, not only the source frequency but also the source signal itself has an influence on the inversion quality. In most of the studies so far a Ricker wavelet was used for simplicity. Even though an ultrasound transducer might be able to produce a Ricker-wavelet-like excitation in most US NDE applications concerning investigation of plates, Hann-windowed tone bursts with a certain number of cycles are used as input as they are easier to generate in real experiments. For example, the validation experiments in section 4.3 use a 5-cycle tone burst as excitation. Therefore, an investigation of the inversion quality for different source terms is very important. Figure 4.7 shows inversion results when varying the source signal for the complex actuator-sensor mode example. For illustration, the source signal is shown in the top right corner of each plot. The same colormap as before is used. Figs. 4.7b to 4.7f show results using Ricker wavelets and tone bursts of different frequencies for the excitation. The frequencies are chosen in a way such that the excitation time for each source signal is approximately the same. It can be seen that the number of cycles and the inversion quality are indirectly related. The more cycles there are the harder it is to recognize the large homogeneous areas as what they are and the more focus is placed on the boundary, where the reflections are occurring.

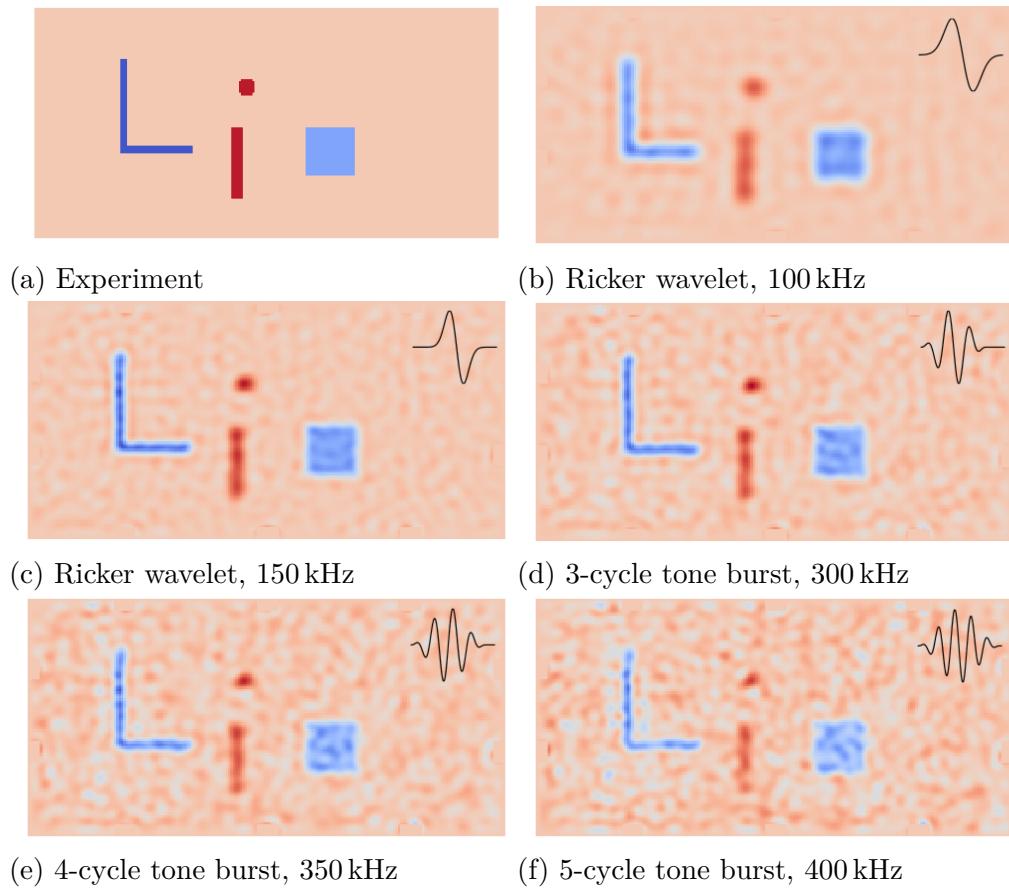


Figure 4.7: Inversion results for different source signals

4.1.5 Noisy flaw inference

For all numerical experiments used so far, the assumption that the pressure wave speed is reduced by a certain magnitude in some area of the model corresponding to perturbed regions of the structure under investigation was used (e.g. $v_f = 0.7v_p$). In this section, a sensitivity study of the algorithm with respect to this assumption is conducted to identify limits for detecting flawed areas. This is very interesting from a health monitoring point of view answering the question whether the algorithm is able to detect perturbations when the material is only slightly damaged. The setup of sensors and sources is shown in Figure 4.8a and a series of small flaws with different wave propagation speeds is introduced in the homogeneous domain to be reconstructed. From left to right, the interior of the flaws correspond to $0.7v_p$, $0.8v_p$, $0.9v_p$, $0.95v_p$ and $0.99v_p$. A Ricker wavelet pulse with dominant frequency of 200 kHz is applied at eight positions for eight different experiments. The inversion is run for 30 iterations until a local minimum is reached. In a first inversion, the experimental signals are used without adding noise. The wave propagation speed is shown in Figure 4.8b. Clearly, the location, orientation and dimension of all flaws with a wave propagation speed up to $0.95v_p$ (or a difference of 300 m s^{-1} or larger) can be inferred from the inversion results. The smallest flaw cannot be distinguished from the background noise. In a second study, the inversion is repeated, but 10% and 20% Gaussian noise is added to the experimental signals. Figures 4.8c and 4.8d show the corresponding inversion results. Compared to the previous inversion, there is more noise

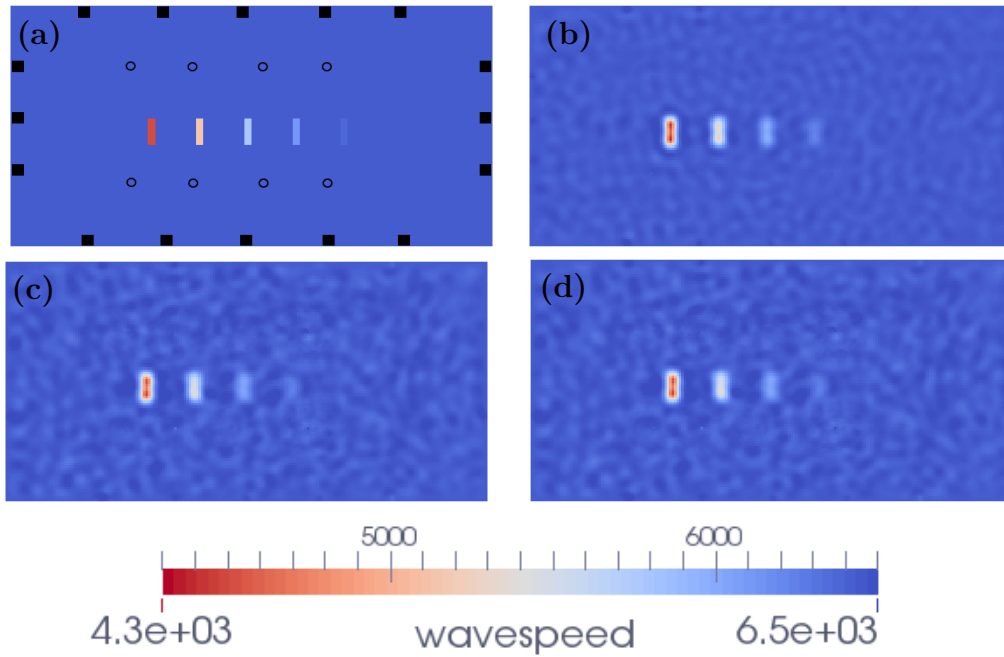


Figure 4.8: Inversion for multiple flaws with different wave propagation speeds.

introduced in the complete domain and the flaw with a wave propagation speed of $0.95v_f$ or 6100 m s^{-1} is hardly detectable anymore. This shows that the inversion method is robust for a moderate amount of Gaussian noise. This corresponds to results obtained by a classical time-reversal model as demonstrated in (Givoli and Turkel, 2012).

4.1.6 Summary

To study its potential, the proposed inversion method was applied to detect flaws in a simulated aluminum plate. It was shown that the method is capable of exploiting the actuator-sensor mode of common piezoelectric sensors to increase the quality of reconstruction considerably by an extended misfit formulation. This allows a possible application in NDT where only a handful of sensors are available in general. Furthermore, it was investigated whether the inversion quality is affected by changing the source parameters and the amount of sensors. One remarkable property of full waveform inversion compared to currently employed methods like time-reversal and topological energy method is the ability to detect multiple flaws of different properties and strongly varying dimension simultaneously without any prior knowledge. Additionally, it was studied how (artificial) noise affects the solution. These are all promising results for the two-dimensional case. The next paragraph deals with the application of the method to three-dimensional objects and a possible look inside a structure through US tomography.

4.2 Full Waveform Inversion for Solids

There is a need of high resolution 3D NDE imaging systems to ensure quality during the production process as well as service and maintenance of structures. Therefore, the goal of ultrasound tomography often is to identify the current state or internal structure of solids. The



(a) Reinforcements in concrete

(b) Cracked reinforced column

Figure 4.9: Reinforcements of concrete

last section showed promising results for the two-dimensional case and the logical next step is to apply the method to solids. A possible application of US tomography is to image reinforcement in concrete. Reinforced concrete is a composite material in which the relatively low tensile strength and ductility of concrete are counteracted by the inclusion of reinforcement having higher tensile strength or ductility. For reinforcement steel bars are embedded passively in the concrete before it sets. After the production process the exact positions of the reinforcement in the concrete is not known. Figs. 4.9a² and 4.9b³ show examples of such reinforcements. To avoid damages resulting from drilling into it, the knowledge of its position, dimension and depth is important. Typically, an electromagnetic device such as an Elcometer P120⁴ is used to inspect concrete in real time. Nevertheless, to provide a proof of concept it is investigated whether full waveform inversion can be applied to inspect a block of concrete for the position of its unknown reinforcements. A major drawback of the limited number of US sensors that one can attach to a structure is the decreasing resolution when the same number of sensors as in 2D is used.

4.2.1 Numerical example

For the desired proof of concept, the proposed method is applied to detect possible steel reinforcement in a simulated block of concrete. Its position and dimension is assumed to be unknown. The concrete and the reinforcement are idealized in the following way: The block of concrete is assumed to be of dimensions $100 \times 100 \times 100 \text{ cm}^3$. All boundaries are considered rigid and ultrasonic point sources are applied on the boundary to scan the solid. Sources are modeled as Ricker wavelet pulse with dominant frequency 10 kHz. As background material ultra high performance concrete (UHPC) with a wavespeed of $v_{\text{UHPC}} = 4750 \text{ m s}^{-1}$ is assumed.

²Thomas Max Müller / pixelio.de

³<https://commons.wikimedia.org/wiki/Concrete>

⁴<http://www.elcometer.com/en/concrete-inspection/rebar-stud-locators/elcometer-p120-rebar-locator.html>

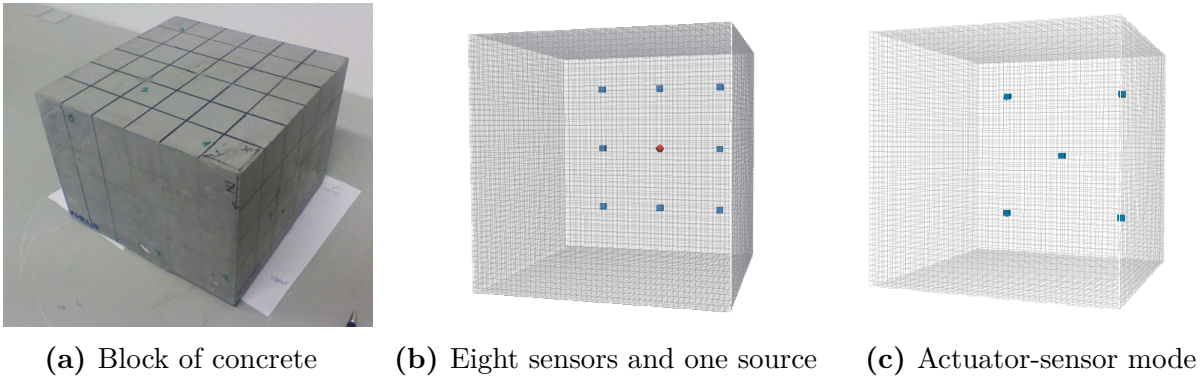


Figure 4.10: Concrete block in lab and sensor setup

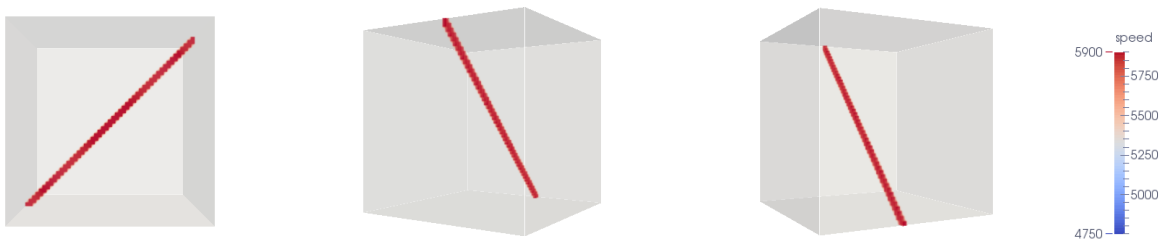


Figure 4.11: Experimental model for reinforced concrete

Concrete is a composite material composed of coarse aggregate bonded together with a fluid cement that hardens over time. UHPC is a fine-grain concrete and the size of its sand and pores is very small ($\ll 1$ mm). As the wavelength of the source is large, the block is assumed to be homogeneous for this study. Fig. 4.10a shows an example of a typical block in the lab. As in the two-dimensional case, the propagation of pressure waves is modeled by the acoustic wave equation. The steel reinforcement is approximated as a region where the wave speed model deviates from the background wave speed of concrete by $v_{\text{steel}} = 5900 \text{ m s}^{-1}$. The wave propagation of the pulse is modeled for a time span $\Delta T = 0.6$ ms. The same finite-difference approximations as in the two-dimensional case are used for the numerical solution of the forward and adjoint problems. The spatial discretization is chosen as one gridpoint each 2 cm, leading to a $50 \times 50 \times 50$ spatial grid. The simulation time is discretized by steps of length $\Delta t = 1 \mu\text{s}$. The modeled time span is chosen such that an US impulse moves at least once through the complete domain. The discretization results in 125 000 parameters for the adaptable wave speed at each grid point.

The question to be answered is: *Is it possible to recover the position, dimension and orientation of the unknown steel reinforcement using full waveform inversion?*

4.2.2 Reconstruction results

In a first experiment, eight sensors are distributed over each of the five available faces of the cube excluding the bottom. To illuminate the reinforcement from different angles an US source is placed to the center of each face. The initial simulation model assumes a completely homogeneous block of concrete. Fig. 4.10b shows the placement of the sensors (blue rectangles) and sources (red circle) for the back face of the block. True experimental data is substituted

by data generated by a second simulation model with similar setup but including modeled steel reinforcement. Fig. 4.11 shows the (unknown) model with a diagonal steel reinforcement from different angles. For the inversion L-BFGS is run for 30 iterations and the deviation from the initial model for different angles is shown in Fig. 4.12. Full waveform inversion is able to reconstruct the dimension, orientation and position of the unknown reinforcement. This is remarkable especially because other model-based methods like time reversal and topological energy method are not able to identify such elongated small regions. It is valuable to inspect the deviation of the wave speeds to visualize the inside of an object particularly if the inversion is not perfect due to the small amount of sources and sensors. This way, regions where the algorithm adapts the wave speed are easily identifiable.

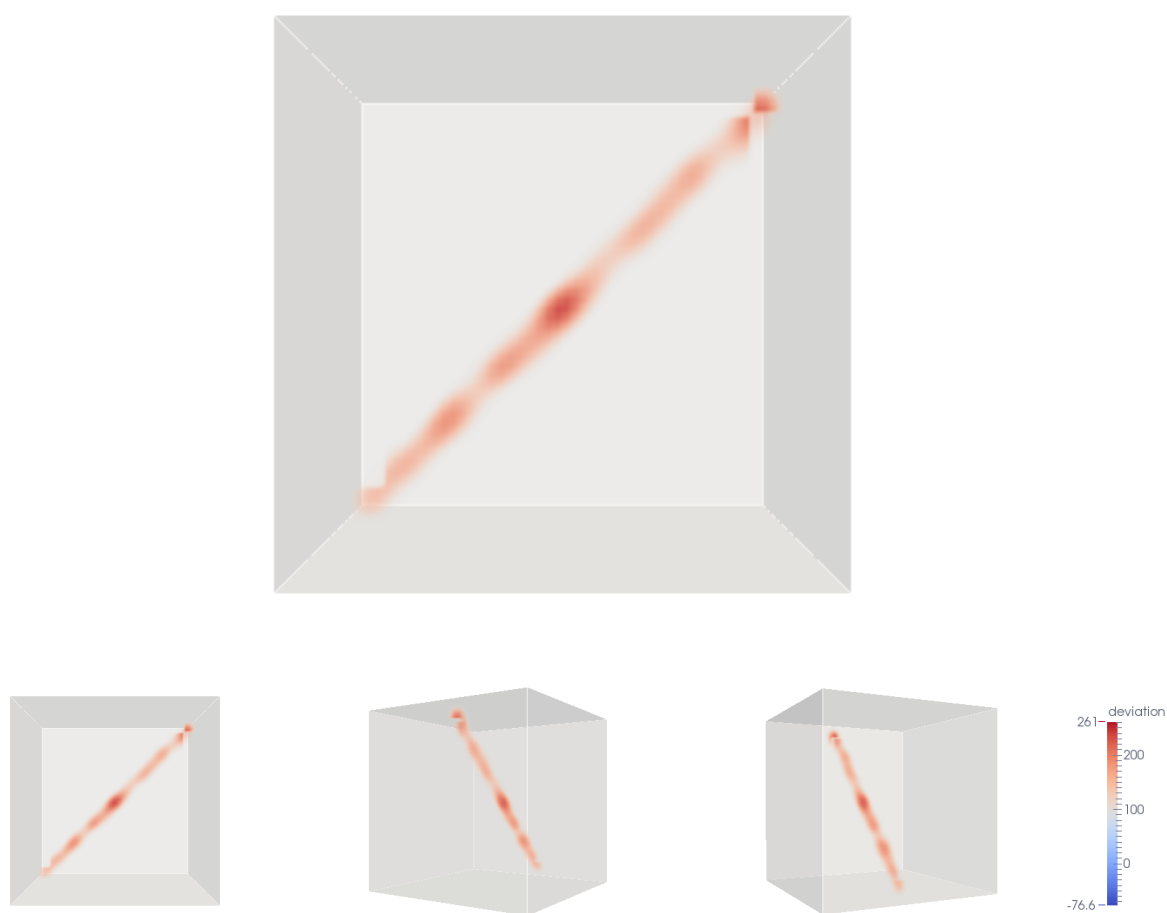


Figure 4.12: Inversion results: deviation from initial model

As before, it is possible to use all sensors in *actuator sensor mode*. Thus, a second sensor configuration is investigated where only five sensor measurements per face are used and each sensor is utilized first as a transmitter and afterwards as a receiver. Fig. 4.10c shows the placement of the sensors (blue rectangles) for the back face of the block. All other parameters of the simulation remain as before. Fig. 4.13 shows the deviation of the inverted model from the initial model for different angles. Again, full waveform inversion is able to visualize the unknown reinforcement.

One important aspect to note though, is that – despite its usefulness as an imaging method for the internal structure – full waveform inversion in its common formulation is not particularly close in capturing the wavespeed in the true model *quantitatively*. This can be seen in Fig. 4.14 investigating the speed profile through the reinforcement from bottom left to top right. There are multiple reasons for this. First, the poor coverage by sources and receivers does not allow for a perfect inversion in terms of correct wavespeed. Second, from a mathematical point of view a large difference between background material and unknown true material poses a problem. Because the model, or more precisely the optimization parameters are chosen as the squared p-wave speeds inside the specimen, the misfit and therefore the error in the signals is heavily reduced by the inversion method by adapting the material at the correct locations. A possible remedy is to extend the misfit formulation to include prior information about the expected solution as will be discussed in the outlook.

As the most important goal of NDT is imaging and not material identification and especially because the true model responsible for the data is not known in reality, studying the deviation from the initial model is satisfactory.

4.2.3 Summary

Full waveform inversion was applied to detect reinforcement in concrete for a simplified model to demonstrate its application to visualizing the inside of solids. The deviation of the inverted to the initial model showed a clear image of the unknown reinforcement when a small number of sensors and sources was used. The quality of the inversion was increased by employing sensors in actuator-sensor mode. The method is able to image the location, dimensions, and orientation of steel reinforcement. Furthermore, no prior information of the amount and dimension of the expected reinforcement and its material description was necessary to give a clear image. When, instead of imaging, the goal is material identification the algorithm can be enhanced by including prior information. This is discussed as part of the outlook. Until now, the experimental data was synthesized by a second simulation model. Therefore, the next important question to answer is if the method can also be employed successfully when confronted with real data from a lab. This is the problem of validating full waveform inversion and it is the content of the next chapter.

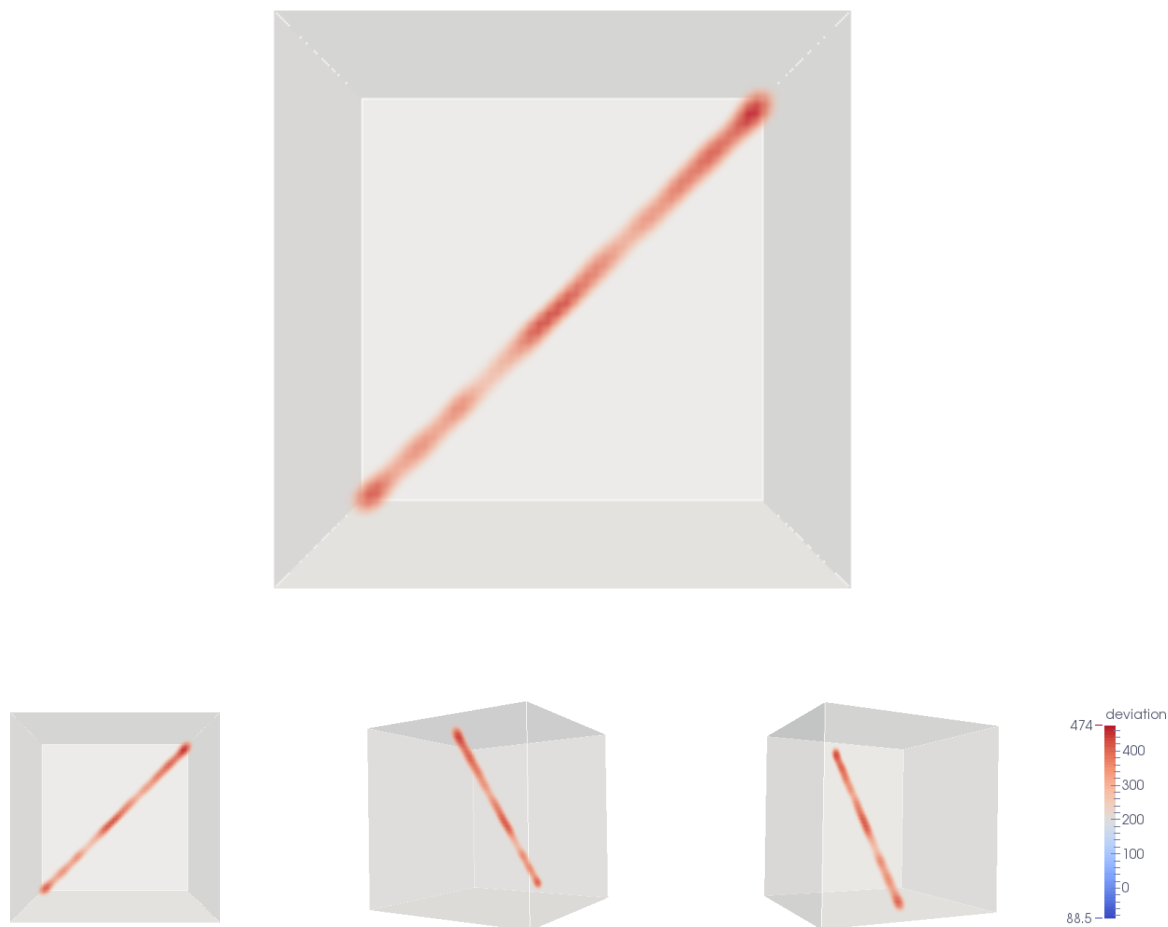


Figure 4.13: Deviation from initial model using actuator sensor mode

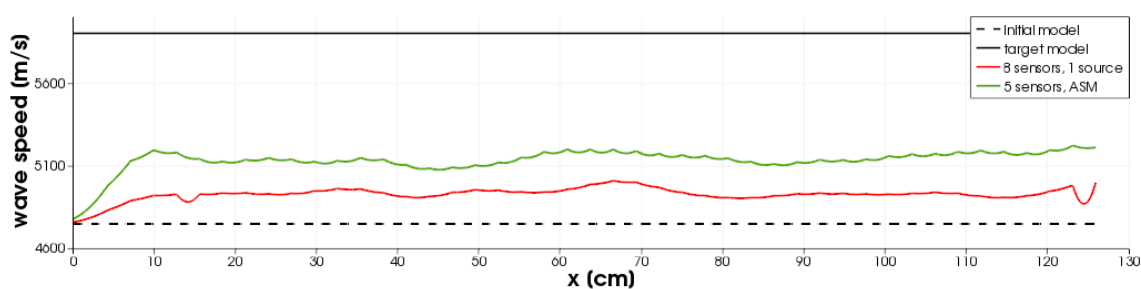


Figure 4.14: Inverted wavespeed in steel reinforcement

4.3 Validation experiments

The previous sections showed promising results applying full waveform inversion for US NDT in 2D and 3D cases. In each case quasi experimental data were provided by a synthetic target model. Yet, it is not self-evident at all that the inversion method yields similar results when confronted with real observations. Therefore, the validation of the method for US NDT

applications is of utmost importance. The tasks of verification and validation are defined as in (Moczo et al., 2014).

(i) Verification

*In general, the verification of a numerical method may be defined as the **demonstration of the consistency of the numerical method** with the original mathematical-physical problem defined by the controlling equation, constitutive law, and initial and boundary conditions. Quantitative analysis of accuracy should be part of the verification.*

(ii) Validation

*Once the method has been verified and analyzed for accuracy it should be confronted with observations - it should be validated. In general, the validation may be defined as the demonstration of the capability of the theoretical model (i.e., the mathematical-physical model and its numerical approximation) to **reproduce observations**.*

Therefore, verification proves the correctness of the computation by comparing computed results with results on (validated) benchmark problems, possibly obtained by other software which has been verified previously, and is answering the question "Is my computation correct?". In contrast, the act of validation can be described as confronting the method/model with real observations. In the case of US NDT this means to confront the method with measurements from the lab. Moreover, in the case of US NDT not only the mathematical model but the whole inversion scheme has to be validated. This means that it is not enough to show that the acoustic approximation is valid but also that the formulation of the misfit, the adjoint problem, the optimization scheme and their interplay is correct.

As the current work is limited to the acoustic case, it is apparent to validate the method on a NDT problem where this assumption is true. In most US NDT inspections of plates, lamb waves in the US range are used for detection (Belanger et al., 2008; Huthwaite, 2014; Leonard et al., 2002). Unfortunately, an acoustic model is not able to provide them. Nevertheless, the propagation of dispersive lamb waves in aluminum plates can be approximated by a two-dimensional acoustic model *for a fixed frequency* (Huthwaite and Simonetti, 2011).

The goal is a validation of full waveform inversion (and its implementation) through a monochromatic reconstruction of the thickness of a known drilled hole in an aluminum plate. Therefore, only waves of one frequency are investigated for the inversion. The experimental measurements in the lab and a first validation of full waveform inversion in frequency domain using guided waves was achieved most recently by the group of Prof. Fan Zheng⁵ from Nanyang Technological University, in Singapore. Their results for the experiment are published in (Rao et al., 2016a). They provided the data for our validation.

The objectives for this part are the following:

(i) show applicability of time domain FWI to a problem in US NDT

(ii) validate the developed time domain FWI approach

⁵Prof. Zheng Fan, Jing Rao, School of Mechanical and Aerospace Engineering, Nanyang Technological University, Singapore

- (iii) study the influence of sources and sensors on the quality of the inversion method by answering the question *How many sensors and experiments are necessary for a successful inversion?*

The answer to this question is of particular importance from a NDT perspective because the amount of sensors and sources is often the limiting factor regarding resolution in most applications. The validation is divided into the following steps:

- (i) Detailed description of the experiment
- (ii) Definition of the acoustic simulation model for the plate problem
- (iii) Determination of a suitable cost function
- (iv) Calibration of simulated and experimental data
- (v) Validation of the inversion with experimental data
- (vi) Study of the influence of number of sensors and experiments on the quality

First, the validation experiment is described in detail.

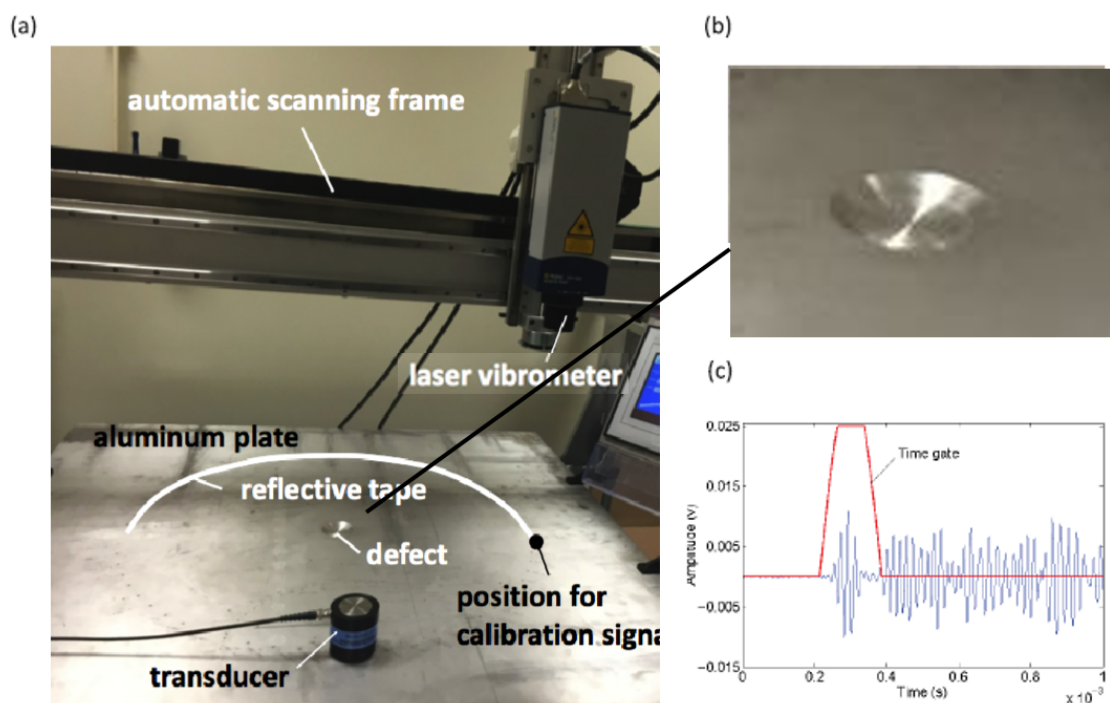


Figure 4.15: Setup of validation experiment, after Rao et al. (2016a)

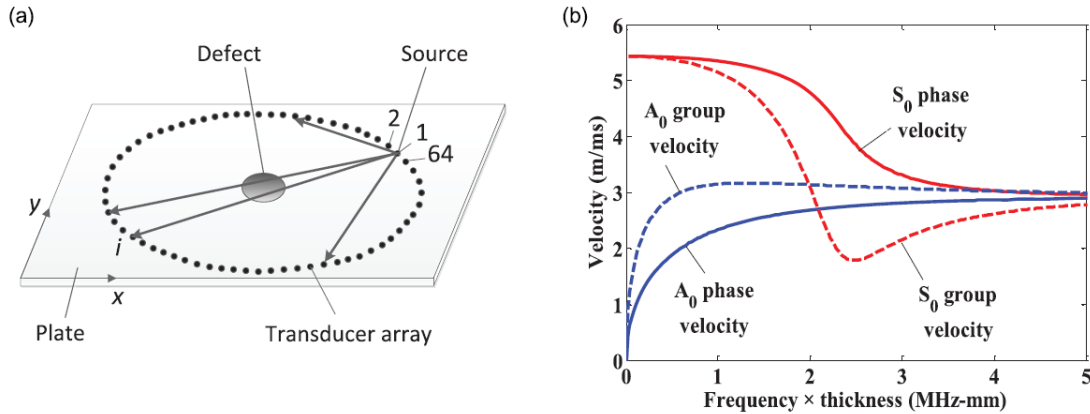


Figure 4.16: Validation setup of FWI, after Rao et al. (2016a)

4.3.1 Description of experiment

The dimensions of the inspected aluminum plate are $1000 \times 1000 \times 10 \text{ mm}^3$. An illustration of the setup is shown in Fig. 4.16a. A flat-bottomed circular hole with a diameter of 60 mm and a depth of 5 mm was drilled into the center of the plate. Its out-of-plane displacement is monitored at 64 equally spaced positions on a 700 mm diameter circle around the defect using a Polytec OFV-505 laser vibrometer. To avoid reflections from the edge, only transmitted signals are used, reducing the measurement to 33 positions. As a source a 5-cycle Hann-windowed toneburst signal at 50 kHz, applied in out-of-plane direction, is generated by a Tiewie Handyscope HS3. Applying the force at this frequency ensures that nearly pure flexural waves are excited (Belanger et al., 2008). The experimental setup in the lab is shown in Fig. 4.15(a). The generated flexural wave mode, also called A_0 -mode, has its average displacement in the transverse direction and can be recorded by out-of-plane motion using the laser vibrometer. A typical recorded signal is shown in 4.15c. To obtain the first arrival package (the A_0 -mode) and to remove unwanted components a time gate is applied. The measurement is repeated for all 33 sensor positions and the monitor positions are modified to the opposite side of the transducer for each experiment as indicated in Fig. 4.17 for four of the 64 experiments.

The next paragraphs describe the physics, the simulation model, the inversion scheme and necessary calibration.

Physics

Even though the A_0 -mode is an elastic waveform, it has been shown that the propagation of dispersive modes of a certain frequency in plates can be approximated by a two-dimensional acoustic model neglecting the thickness of the plate. This is true, even though no mode conversions at the hole are considered in the model (Huthwaite and Simonetti, 2013). The dispersion relation for fundamental lamb wave modes in an aluminum plate is shown in Fig. 4.16b. It provides the phase velocity of selected guided modes as a function of the frequency-thickness product. For the chosen frequency of 50 kHz and plate thickness of 10 mm, there is a large difference between group and phase velocity of the A_0 -mode. Therefore, the mode is strongly dispersive, in particular to thickness variations.

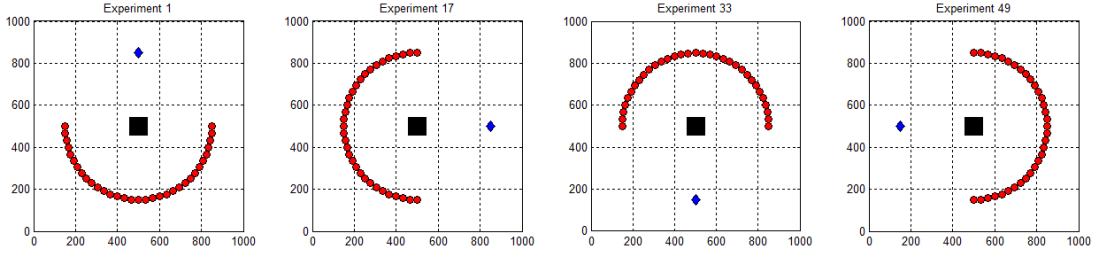


Figure 4.17: Setup of validation experiment for different source positions.

Acoustic model

The propagation of the flexural mode through the plate is described in the space-frequency domain by the Helmholtz equation *at one frequency* f_0 ,

$$\Delta u(x, \omega) + \frac{\omega^2}{v_{A_0}^2} u(x, \omega) = \tilde{f}(x, \omega), \quad (4.3)$$

where $u(x, \omega)$ is the displacement wavefield, $\omega = 2\pi f_0$ the angular frequency, v_{A_0} the phase velocity of A_0 -mode and $\tilde{f}(x, \omega)$ the ultrasonic source. It is derived by a Fourier transform of the acoustic wave equation or equivalently by assuming $u(x, t) = U(x)e^{i\omega t} + \bar{U}(x)e^{-i\omega t}$ (Givoli, 2014). It has been employed directly in (Rao et al., 2016a). Every method developed for the time domain can also be used in the frequency domain by applying the Fourier transform to all variables and equations (Givoli, 2014).

The frequency domain approach is the method of choice if the solution for dominant or well-chosen frequencies is needed or the underlying problem is two-dimensional. In these cases 4.3 can be solved efficiently using direct linear system solvers like LU decomposition. This allows an easy computation of wavefields for multiple source locations. However, the frequency domain approach is usually limited to 2D problems due to large memory requirements related to the storage of the LU decomposition in 3D. Therefore, in realistic 3D applications the time domain approach is implemented. (Fichtner, 2011).

For this reason and because all results so far are based on a solution of the acoustic wave equation in the space-time domain the equation is formulated equivalently in the space-time domain using a monochromatic source function.

$$\partial_{tt} u(x, t; \omega) + v_{A_0}^2 \Delta u(x, t; \omega) = f(x, t; \omega) \quad (4.4a)$$

$$u(x, 0; \omega) = u_t(x, 0; \omega) = 0, \quad \text{on } \Omega \quad (4.4b)$$

$$u(x, t; \omega) = 0 \quad \text{on } \partial\Omega \quad (4.4c)$$

The source term is $f(x, t; \omega) = A \cdot \sin(\omega t + \phi) \cdot \delta(x - x_s)$, with A being its amplitude and ϕ its phase. The additional argument ω in $u(x, t; \omega)$ emphasizes that this is the solution of the acoustic wave equation for one certain angular source frequency ω .

The measured time-dependent signals at the sensors are then mapped into frequency domain

selecting amplitude and phase information at $f_0 = 35$ kHz. The 1 m^2 plate is discretized by the same finite differences as before with a spacing of 2.5 mm in both directions leading to a 400×400 grid. Using this spacing there is sufficient sampling per dominant wavelength. The simulation is run for 0.8 ms divided in 1000 time steps such that the CFL condition is satisfied. The simulation domain is extended such that there are no non-physical reflections at the boundary.

Inversion scheme

Experimental data are the time domain signals recorded by the laser vibrometer. These data cannot be used directly in the inversion as the acoustic model is only valid for modeling the propagation of the wave mode at one frequency. The source function has a 15 dB bandwidth from 35 kHz to 65 kHz. Therefore, performing a Fourier transform, the experimental data are reduced to amplitude and phase information at a frequency $f_0 = 35$ kHz that is fixed for the inversion. The recorded data at the sensors are represented by a vector of \mathbf{d}_{obs} of complex numbers, representing the amplitude and phase information at the sensors.

The diameter of the defect is 60 mm, which corresponds to $\approx 1.3\lambda$ at 35 kHz. Thus it should be detectable at this frequency. As the frequency of a guided wave remains the same as it travels through a region of reduced thickness, the dispersion curve provides a direct mapping between the corresponding velocity of the wave mode for a certain frequency and the local thickness of the plate. When passing through the flaw, the reduced thickness leads to increased speed of the waves. This effect can be used to formulate a misfit functional for full waveform inversion.

The simulated signals at the sensors at iteration k , \mathbf{d}_{calc}^k , are amplitude and phase information stored as complex numbers. Then, a least-squares misfit can be formulated similarly as in the time domain.

$$J^{(k)}(m) = \frac{1}{2} \sum_{i=1}^N \Delta \mathbf{d}_i^\dagger \Delta \mathbf{d}_i, \quad (4.5)$$

with $\Delta \mathbf{d}_i := \mathbf{d}_{calc,i}^k - \mathbf{d}_{obs,i}$ being the misfit between the data computed at all sensors with the current model and the observed data for experiment i . The superscript \dagger represents the transposed conjugate and the residuals are combined for all N experiments. Furthermore, the corresponding adjoint problem for experiment p is

$$u_{tt}^\dagger(x, t; \omega) - v_{A_0}^2(x) \Delta u^\dagger(x, t; \omega) = f_s^\dagger(x, t; \omega) \text{ for } x \in \Omega, t \in [0, T] \quad (4.6a)$$

$$u^\dagger(x, T; \omega) = u_t^\dagger(x, T; \omega) = 0, \text{ on } \Omega \quad (4.6b)$$

$$u^\dagger = 0 \text{ on } \partial\Omega \quad (4.6c)$$

where

$$f_s^\dagger(x, t; \omega) := \sum_{j=1}^M [z \cdot e^{i\omega t} + \bar{z} e^{-i\omega t}] \delta(x - x_j^r).$$

where $z := \mathbf{d}_{calc,p}^k - \mathbf{d}_{obs,p} \in \mathbb{C}$ at sensor position x_j . As in the time domain case the residual is injected at the sensor positions but here a sinusoidal load of a certain frequency is applied. Its

amplitude and phase is determined by the differences between simulated and recorded signals. Solving this problem backward in time then means conjugating the source term $f_s^\dagger(x, t; \omega)$.

The overall procedure is illustrated in Fig. 4.18. It shows how the full waveform inversion process is extended in case of lamb wave tomography. An initial frequency f_0 has to be chosen that defines the wave speed in the initial acoustic simulation model through the dispersion relation. Observed data and model response are in the time domain and thus have to be mapped to its frequency content at f_0 to be used in the residual and least-squares objective 4.5. After the inversion, the final velocity model is mapped to a thickness model using the dispersion relationship.

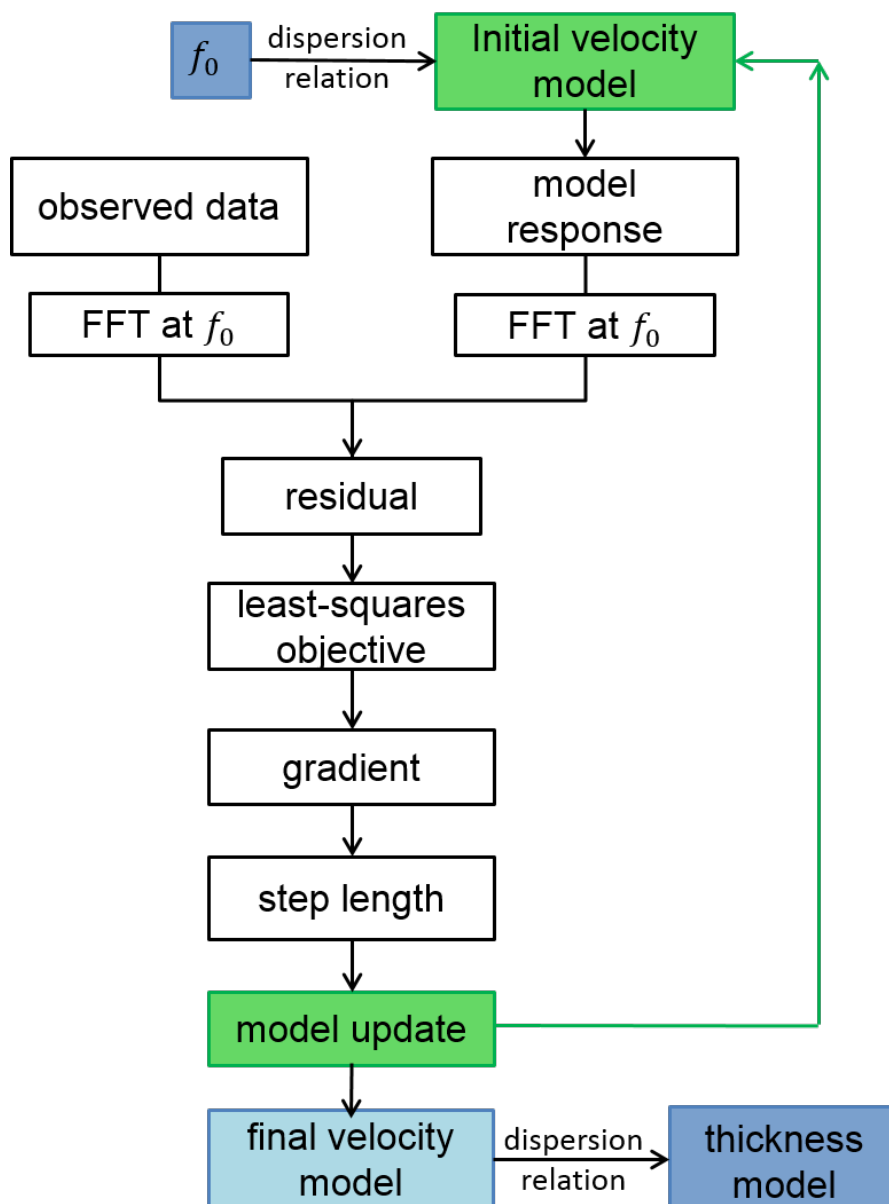


Figure 4.18: Validation process of FWI

Data calibration

A very important step when using data from an experiment is the calibration of simulated and measured data. This needs to be done to account for deviations between experiment and simulation model. These include, but are not limited to, incorrect sensor placements, attenuation and ambient conditions. One way, also followed by Rao in (Rao et al., 2016a), is to match the wave propagation results of experimental data of the undamaged plate and simulation data without scatterer. This can be done by introducing a calibration factor

$$Q = \frac{fft^*(d_{Sim})}{fft^*(d_{Exp})}. \quad (4.7)$$

For each experiment, the recorded experimental data (amplitude and phase information at 35 kHz) are mapped to the simulated data by introducing a complex calibration factor Q . One problem arises due to the presence of the defect in the experiment: undistorted signals are only available at certain positions. The position of the calibration sensor is shown in 4.15(c). In order to emulate the necessary measurements of the unflawed plate the calibration signal is mapped to all other receivers according to their position relative to the transducer.

4.3.2 Reconstruction results

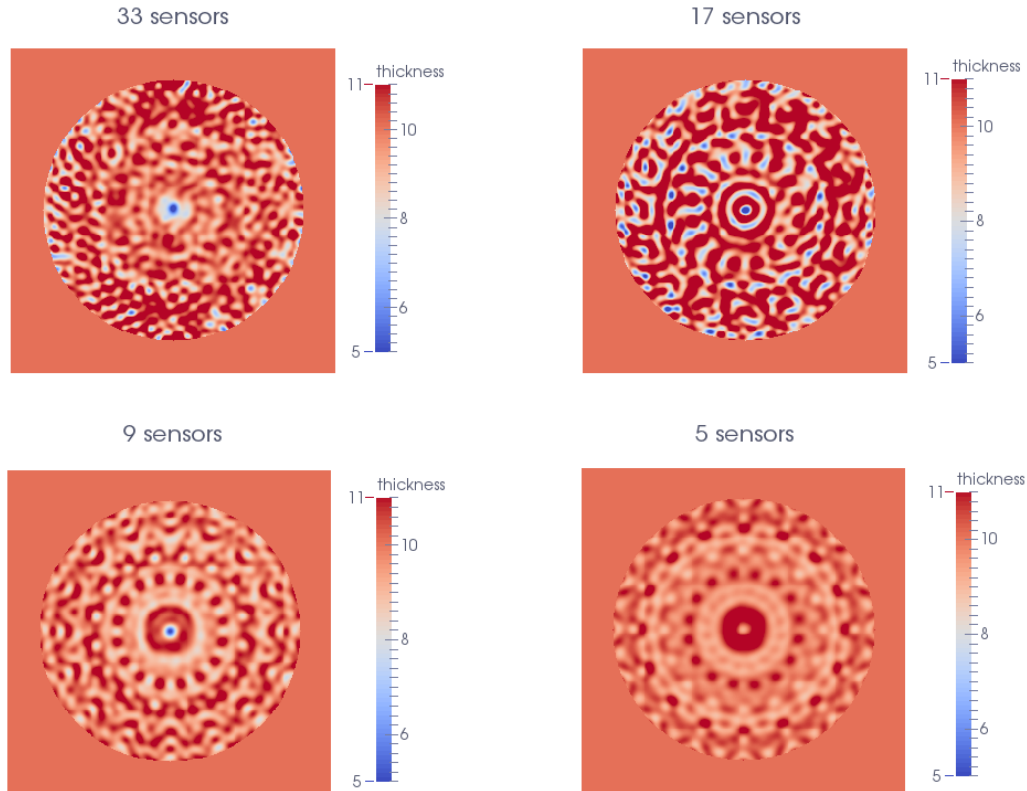


Figure 4.19: Inversion results for 16 experiments and varying number of sensors

In the lab experiments, data were generated by moving a transducer on a circular path around the defect at 64 equally spaced positions and the laser vibrometer recorded the out-of-plane

movement at 33 positions behind the flaw. *Rao et al.* were able to reconstruct the flaw using full waveform inversion for the complete data set (Rao et al., 2016a). They solved the forward problem 4.3 in the frequency domain by a finite difference method using a mixed-grid approach and smoothed the gradient to reduce unreasonable artifacts. Most importantly, they used all data and a multi-scale approach to reconstruct complex corrosion-like defects. In this work, we solve the acoustic wave equation instead of the Helmholtz equation using our time-domain finite difference solver and apply the BFGS method. Instead of smoothing the gradient, we assume that the flaw is located inside the sensor array and thus limit the optimization parameters to a smaller circular region as discussed in Sec. 2.4. We only perform a monochromatic reconstruction for $f_0 = 35$ kHz. Furthermore, we investigate the important question, how many experiments and sensors are truly needed for a successful inversion. Considering that the positions of most sources are very close to each other compared to the wavelength of the source and that this is also true for most sensor measurements, it is reasonable to expect that some of the recorded data is redundant and that a successful inversion can be possible using less data. This is very important for common US NDT where the typically small number of available sensors and sources is a limiting factor for the achievable resolution of all reconstruction methods. To study the minimal amount of sensors and receiver, the inversion is performed using only a subset of the experiments and sensor data available.

To start with, the quality of the inversion was investigated using 4 and 8 experiments with a varying number of sensors. In all inversions it was not possible to reconstruct the flaw and its depth. Therefore, the results are not shown and the focus is on an inversion using 16 experiments, i.e. 16 positions of the transducer. L-BFGS is run for 10 iterations as this proved to be sufficient following (Huthwaite and Simonetti, 2013; Rao et al., 2016a) and the number of sensors used is varied. Fig. 4.19 shows the results of the inversion using only data of every fourth experiment on the circle. The reconstruction of the wavespeed is mapped to an estimate of the thickness of the plate. Fig. 4.19a shows the results using all 33 available sensor measurements. Clearly, the position and dimension of the drilled hole is successfully reconstructed in the middle of the plate. Furthermore, the results give a good estimate of the depth of the hole. Fig. 4.19b shows the result when only every second sensor is used. Still, the flaw, its dimension and depth, is correctly reconstructed, but there is a lot of noise that makes a clear detection of only the flaw impossible. Very interestingly, when only nine sensors are used, the position, dimension and depth of the flaw is clearly reconstructed again, as shown in Fig. 4.19c. One possible reason for the problems with 17 sensors and not with nine is that the sensor positions in the experiment are not perfectly aligned with the finite difference grid and therefore some of the slightly shifted sensor measurements due to wrong positioning might introduce some error that makes it tougher for FWI to find a suitable minimum. Fig. 4.19d shows the results when only using five sensors. This number of sensors does not seem to be enough for a successful inversion.

To investigate the results further and compare them to the ones obtained by *Rao et al.*, the thickness profile along the flaw is shown in Fig 4.20. Fig. 4.20a shows the results by *Rao et al.* and 4.20b the results obtained with our inversion. In the case of 17 sensors there are strong oscillations and an overestimation of the minimal thickness. In all other cases the depth of the flaw is reconstructed correctly.

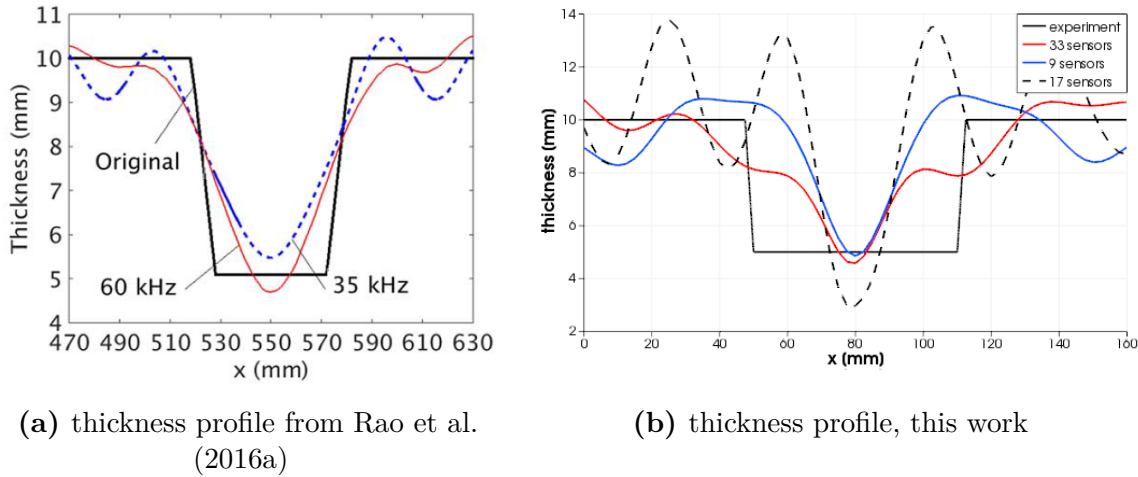


Figure 4.20: Inversion results: Comparison to results from Rao et al. (2016a)

4.4 Summary

The applicability of full waveform inversion was investigated in the context of US NDT. Firstly, the suitability of the method in the case of acoustic plate problems was studied. The non-uniqueness of the inverse solution of a full waveform inversion motivated an investigation of the effect of changing various parameters like varying sources on the solution and special emphasis was put on studying the question how many sensors are needed for a successful inversion. For the case of a realistic number of sensors, it was shown that the actuator-sensor mode of common piezoelectric sensors can be used to significantly improve the resolution. Secondly, full waveform inversion was applied to image the location of reinforcement in concrete for a simplified model. This demonstrated the possibility to look inside solid specimen using acoustic tomography. The deviation of the inverted from the initial model gives a clear image of the location of unknown reinforcement when using actuator-sensor mode. Thirdly, the cornerstone was the validation of the applicability of full waveform inversion for US NDT. Positive validation results in frequency domain by *Rao et al.* have been approved using our own time-domain full waveform inversion code. Moreover, these results have been enhanced by a study on the minimal amount of sensors and sources needed for the inspection of a drilled hole which showed that only 25% of the recorded data are actually needed. This gives a first proof of concept for the applicability of full waveform inversion for US NDT. Possible enhancements and applications of the methods are discussed in the outlook.

Chapter 5

Conclusion and Outlook

5.1 Conclusion

In the field of ultrasonic nondestructive testing (US NDT), ultrasonic impulses are used to detect flaws in components without causing damage. Based on performing experiments alone, it is possible to infer the state of the component - but this usually provides only limited details about the interior damage such as its position, dimensions, or orientation. Furthermore, the number of sensors that can be used to record the signals is restricted to only a few, because of the shape and the dimensions of a typical specimen.

As US waves are reflected at crack surfaces, the reflections are contained in the complete measured waveforms. Simple reconstruction methods rely only on a single attribute of the recorded US data - such as travel time or amplitude - and it is assumed that this attribute can be related to a physical quantity like the wave speed inside the specimen.

Clearly, using all information that is encoded in the measured signals instead of only one attribute should increase the resolution of the imaging and possibly allow to determine the position, orientation, and dimensions of the flaws more precisely. For this purpose, a full numerical simulation of the wave propagation is necessary.

The work transferred *full waveform inversion* from exploration geophysics to US NDT. In this context, the method can be interpreted as a simulation model-based NDT system, where experimental data is compared to simulated data. The key to full waveform inversion is a clear mathematical formulation of the question *How do I have to change the distributed wave speed inside the specimen to get my simulation model to produce signals at the sensors that are as close as possible to the experimentally measured once?* Here, flaws such as inclusions or holes are modeled as a deterioration of the wave speed in the specimen.

If the signals are similar, one can expect that the position, orientation, and dimensions of the flaws are captured in the adapted wave speed model and, thus, that the flaws and its details can be inspected visually.

Formally, the problem is posed as a nonlinear optimization problem, and an initial wave speed model is adapted in such a way that the discrepancy between the experimental measurements and the model output is minimized using a gradient-based iterative optimization. Here, full wave equation modeling is performed at each iteration, and the adjoint sensitivity state method is used to efficiently calculate the gradient of the high-dimensional objective. As an initial guess, a model of the undamaged specimen is assumed.

The work focused on a prototypical implementation in the case of acoustic wave propagation. Although an acoustic model only describes the propagation in fluids and gases accurately, it is also appropriate to model the first arrival of pressure waves in elastic media.

While other model-based NDT approaches like ray-based inversion, time reversal, and the sensitivity kernel method are not suitable to invert for multiple scatterers of different dimensions simultaneously (and since it does not provide information on size, orientation, or the shape of flaws in the interior) the proposed method

- evaluates the full ultrasonic wave signal and, thus, the maximal information available
- delivers a tomographic image and - as flaws are generally treated as deterioration of material parameters - allows for nondestructive testing
 - by identification of position, orientation, and shape of flaws
 - by simultaneous detection of multiple flaws of different size
 - without prior knowledge of flaw occurrence or its specific characteristics
- is model-based, enabling easy incorporation of data from multiple NDT experiments, e.g.
 - improving image quality by additional experiments
 - allowing measurements at different points in time without enforcing positioning of sensors at identical spatial coordinates.

Furthermore, it was shown how time reversal and the sensitivity kernel method can be identified as integral parts of full waveform inversion. The general complexity of the proposed approach is justified by the potential to fully automate the imaging of complex structures using US NDT, which would be a major milestone for the quality assurance in civil and mechanical engineering.

As the result of full waveform inversion is a wave speed field of the flawed structure, image-based NDT is easily possible.

An attempt is made to answer the research questions posed in the introduction of the thesis.

(1) Can full waveform inversion be employed to provide more information on the position, dimensions, and orientation of flaws than common model-based US NDT methods by putting more emphasis on the simulation side, as full wave equation modeling is performed at each iteration? (2) Can the resolution of the imaging be enhanced by adapting the method to a typical NDT setup? (3) Can the method be validated for US NDT using experimental data?

- (1) Given enough sensor measurements and experiments, the inverted model is able to provide information on the size, orientation and shape of flaws in the interior of the specimen. The applicability of the method to US NDT was verified by simulations on a flawed emulated aluminum plate. Furthermore, it was studied how differences in setup influence the solution quality. As a means of verification in the case of solids, the visualization of reinforcement in concrete was explored, implying that full waveform inversion can be used to take a look inside a solid. Overall, the method showed very promising results regarding the detection of multiple flaws of different dimensions, orientation, or position.

- (2) Especially in the typical case of NDT, where only a limited number of sensors is available, putting more emphasis on simulation using the complete signal information allows a better resolution with less sensors. In this case, it is possible to set up one large inversion based on the measurements from multiple experiments employing the actuator-sensor mode of piezo-electric sensors, where one sensor acts as source in a round-robin fashion. As multiple experiments have to be simulated, this leads to increased simulation costs – but it showed to significantly improve the resolution of the imaging.
- (3) A first successful validation of the suitability of the method for a specific problem in US NDT was performed using experimental data. In the special case of a thin aluminum plate, the propagation of flexural waves (lamb waves) can be approximated by a two-dimensional acoustic model for a fixed frequency, neglecting the thickness of the plate. Therefore, it was possible to recover the thickness of an aluminum plate with a manufactured defect using guided ultrasonic waves. It is expected that it can be applied to detect corrosion in tubes.

The overall goal of both exploration seismology and US NDT is to get the most information out of the available data. As seismologists learned that ray-based models only provide a limited resolution this is also true for US NDT. One obvious way to increase the resolution is to use as much of the recorded data as possible – but US NDT is of considerable advantage for various reasons. The source signal and its frequency can be adapted to the expected flaw size, the positioning of sensors can be optimized, experiments can be repeated, and validation experiments can be performed on specimen with known fabricated defects. All of this is not possible for seismologists, and it clearly affects the possible resolution. This thesis showed that by putting more weight on the simulation side by computing an accurate numerical wave propagation an increased resolution is possible. This is still a very expensive task at the moment, especially when considering elastic wave propagation. In many disciplines in science and engineering the areas where computation or a combination of computation and simulation play a major role are easily identified: They are called *computational biology*, *computational chemistry*, *computational physics*, *computational mechanics* or *computational seismology*. In this spirit the study of NDT with a focus on simulation models may be called *computational NDT*. More attention will be drawn to this area with increasing computational power.

5.2 Outlook

This thesis was able to prove the applicability of full waveform inversion for US NDT. For the prototypical implementation, the underlying problem was kept as simple as possible. This led to promising first results but further research is necessary. Various improvements are possible that are discussed next.

Multi-scale full waveform inversion. An important improvement of full waveform inversion in terms of resolution quality concerning small-scale features can be achieved by not only considering a monochromatic inversion but by carrying out successive inversions over data with decreasing wavelength. Cost functions related to small-period (or high-frequency) data are known to be highly nonlinear with many local minima. Therefore, if the initial model is not a good estimate, an iterative optimization method might get stuck in a bad local minimum

that is far away from the global one. It is known that cost functions for long-period data tend to be smooth with fewer local minima (Fichtner, 2011). Clearly, by using solely long-period data, the inverted model can only roughly resemble the true material distribution. However, and this is the important concept, the rough estimate that explains the long-period data well is very useful as initial model for a subsequent inversion employing shorter wavelength data. By reconstructing long-period features in the model first, it is possible to incorporate short-period features in later stages. Multi-scale full waveform inversion is more demanding in terms of runtime, but it yields an increased resolution for complex models in seismology (Bunks et al., 1995; Fichtner et al., 2013; Mao et al., 2012; Ravaut et al., 2004) and it is applied for the reconstruction of complex corrosion patches in an NDT environment (Rao et al., 2016a).

Incorporation of prior information. In the current prototypical implementation of full waveform inversion no information on the desired or expected solution of the problem has been assumed. In many NDT applications, however, there is prior information about flaws available. For example, if we expect jumps in the wave speed because of a cracking of the material, it is desirable to incorporate this information in a suitable regularization term in our cost function. In this particular case, including total variation regularization helps to recover sharp material interfaces (Fichtner, 2011).

Furthermore, if we know in advance what we are looking for, incorporating this into the misfit may significantly improve the method by either increasing its resolution quality or by decreasing the necessary number of iterations to find a suitable solution. If we want to inspect concrete with regard to steel reinforcement as described in Sec. 4.2, we already know the wave speed of the expected flaw. If there is a large difference in wave speed between the background material and the reinforcement, then we can drive the optimization to binary solutions where the material is either identified as background or reinforcement by adding suitable penalty and regularization terms to the data misfit.

Another interesting scenario in US NDT is when holes or delaminations are considered. In these cases, when the unknown wave speed is zero or close to it, the continuous correction of the material is not able to capture this unless a suitable reformulation of the misfit is performed to push the solution in the right direction. Hence, there is great potential to incorporate prior information into the optimization.

Governing equation. For this first prototypical implementation of full waveform inversion for US NDT, we assumed that an acoustic model of the wave propagation is valid. This model has severe limitations since shear and lamb waves as well as mode conversions occurring at the boundary cannot be described, as partly discussed in Sec 1. Clearly, the most general and suitable formulation for the propagation of US waves is given by the elastic wave equation, which can be derived directly from Newton's second law.

In (Bleistein et al., 2001) it was already mentioned, that going from acoustic to elastic approximation comes with a significant cost: *"The price for this increase in information is high [considering S-waves, elasticity], as there are difficult mathematical obstacles that must be surmounted in the pursuit of useful elastic formulations."*

An inversion formula that makes use of data for all wave types provides more information about the material. But considering the elastic model brings additional challenges. One is that the solution is not a scalar field but a vector field. This leads to both – a significantly increased memory consumption and a runtime of the solver, which are approximately multiplied

by a factor of 10. Another challenge is that additional phenomena like birefringence, the apparent splitting of shear waves, are encountered working with shear waves. Importantly, the inversion becomes a multi-parameter optimization problem, because parameters cannot only be the pressure wave velocity, but also the shear wave velocity, or even the density of the medium. In the most general setting, one could theoretically invert for 21 elastic parameters simultaneously. Clearly, this leads to an increased complexity compared to acoustic inversion which makes this problem even harder to solve. Inverting for multiple parameter simultaneously may lead to ambiguity because a change in one parameter might explain the data equally well as a change in the other parameter. One approach is to first consider only an inversion of the pressure wave velocities and then consider the inversion of shear wave velocity, given the fixed pressure wave velocities. Inverting for multiple parameters makes the inherent problem of data quality and poor sensor coverage even more substantial, especially in 3D.

Numerical method. The numerical solution of the wave equation was based on a simple finite-difference scheme with explicit time stepping. Even though finite-differences are widely used in seismology (Moczo et al., 1997, 2014, 2007), other numerical methods seem to be better suited for US NDT. A great overview of numerical methods for seismic wave propagation is presented in (Igel, 2016). Especially the modeling of free surface conditions and the application to complex geometries are tough problems for finite-differences.

An alternative is the spectral element method (SEM). Here, the computational domain is subdivided into non-overlapping elements that can be adapted to irregular geometries. This is very important for US NDT where such geometries appear frequently. As an example, consider a wing of an airplane for which the geometry is derived from a CAD model. In other cases a geometry description might be based on computer tomography. Spectral elements are designed in such a way that they lead to a diagonal mass matrix that can be easily inverted. This fact renders a fast explicit time stepping possible. Inside an element, a high-order spectral approximation is employed for the dynamic field. For more information, see (Duczek et al., 2013; Joulaian et al., 2014; Komatitsch and Tromp, 2002; Komatitsch and Vilotte, 1998).

Parallel Computing. The overall cost of full waveform inversion depends on the necessary number of function and gradient evaluations to reach a local minimum. The cost of an evaluation is dominated by the solution of the wave equation. To reduce the runtime, the solution process of the wave equation should be parallelized as much as possible. Many of the open-source frameworks that have been developed in seismology are fully parallelized and can be run on supercomputers, on both CPUs and GPUs, and can be applied to ultrasonic wave propagation. Examples are SpecFEM3D¹, SES3D², Salvus³, SeisSol⁴ and ExaHyPE⁵.

In US NDT, data from multiple experiments employing the actuator-sensor mode is often available. In this case, an alternative is to parallelize the function and gradient evaluation by distributing simulations of different experiments to different threads.

If the number of experiments is large ($\gg 10$), then it is beneficial to use *encoded sources*. Here, the linearity of the wave equation with respect to sources is exploited by a simultaneous

¹<https://geodynamics.org/cig/software/specfem3d>

²<http://www.cos.ethz.ch/software/ProductionSoftware/ses3d.html>

³<http://salvus.io>

⁴<http://seissol.org>

⁵<http://exahype.eu/>

excitation of sources from different experiments. Thus, it is possible to reduce the number of necessary simulations per evaluation to only a few. It has been shown that this procedure can speed up full waveform inversion considerably (Krebs et al., 2009; Schiemenz and Igel, 2013).

Optimal experimental design. As we have seen, the number of sensors is often limited to only a few and the question naturally arises where to place them to ensure that the inspection will exhibit the best possible resolution. The topic of optimal experimental design has recently been addressed in the seismic community. Often, a uniform placement does not lead to the best possible resolution, and optimization methods can be used to determine the best setup and minimal number of sensors. A great introduction can be found in (Curtis, 2004; Long et al., 2015; Martiartu et al., 2017). In its simplest form, optimal experimental design uses a ray-theoretical model to determine the setup of sensors and sources, which maximizes the overall ray-density between sensors and sources. Revisiting the sensor setup in Sec. 4.2, we placed five sensors on each of the five available sides of a cube. In terms of ray-density, this cannot be an optimal design. This is due to the fact that the ray-density close to the top face is higher than close to the bottom face as there are no sensors at the bottom face. Consequently, it would have been beneficial to put more sensors close to the bottom to increase ray-density where sensors are further away. Likewise, following the same argument, the measurement positions on the half-circle in the validation experiment in Sec. 4.3 should be placed in such a way that more measurements are taken close to both ends of the half-circle. In general, optimal experimental design is expensive but it has to be performed only once to determine the necessary number of sensors and their optimal positioning.

Appendix A

Lagrangian Formulation

Sec. 3.3.2 introduced the adjoint formulation of a sensitivity function from the standpoint of perturbation theory. In this case a more convenient way to derive the adjoint formulation is to use Lagrange multipliers. Following (Plessix, 2006), let $J(m) = h(u(m), m)$ be the cost function we want to minimize. Here, m is the model parameter and belongs to the model parameter space \mathbf{M} . The state variable, u , belongs to the state variable space \mathbf{U} , which is either real or complex, and satisfies the state equation defined by the mapping, F ,

$$F(u(m), m) = 0. \quad (\text{A.1})$$

In order to distinguish between such a physical realization u and any element of \mathbf{U} , its elements are denoted by \tilde{u} .

It is well known from optimization theory that if we want to find the minimum u of $h(\tilde{u}, m)$ under the constraint $F(u, m) = 0$, we can formulate this problem using the Lagrangian associated to this minimization problem.

$$\mathcal{L}(\tilde{u}, \tilde{\lambda}, m) = h(\tilde{u}, m) - \langle \tilde{\lambda}, F(\tilde{u}, m) \rangle, \quad (\text{A.2})$$

where λ is an element of the dual space of U which does not depend on m . Importantly, u is a physical realization, thus $F(u, m) = 0$ for any $\tilde{\lambda}$ and therefore

$$\mathcal{L}(u, \tilde{\lambda}, m) = h(u, m) = J(m). \quad (\text{A.3})$$

Deriving for m

$$\frac{\partial \mathcal{L}(u, \tilde{\lambda}, m)}{\partial \tilde{u}} \frac{\partial u}{\partial m} + \frac{\partial \mathcal{L}(u, \tilde{\lambda}, m)}{\partial m} = \frac{\partial J}{\partial m}. \quad (\text{A.4})$$

It is possible to choose $\lambda \in U^*$ such that

$$\frac{\partial \mathcal{L}(u, \tilde{\lambda}, m)}{\partial \tilde{u}} = \frac{\partial h(u, m)}{\partial \tilde{u}} - \left(\frac{\partial F(u, m)}{\partial \tilde{u}} \right)^* \lambda = 0 \quad (\text{A.5})$$

Therefore, the gradient can be computed using the following formula.

$$\frac{\partial J}{\partial m} = \frac{\partial \mathcal{L}(u, \lambda, m)}{\partial m} \quad (\text{A.6})$$

$$= \frac{\partial h(u, m)}{\partial m} - \left\langle \lambda, \frac{\partial F(u, m)}{\partial m} \right\rangle \quad (\text{A.7})$$

u is a minimum of this problem if (u, λ) is a saddle point of \mathcal{L} . λ are called the Lagrange multipliers. At a saddle point the derivative of \mathcal{L} is zero. The derivatives with respect to \tilde{u} and $\tilde{\lambda}$ are

$$\frac{\partial \mathcal{L}(\tilde{u}, \tilde{\lambda}, m)}{\partial \tilde{\lambda}} = -F(\tilde{u}, m), \quad (\text{A.8})$$

$$\frac{\partial \mathcal{L}(\tilde{u}, \tilde{\lambda}, m)}{\partial \tilde{u}} = \frac{\partial h(\tilde{u}, m)}{\partial \tilde{u}} - \frac{\partial F(\tilde{u}, m)}{\partial \tilde{u}}^* \tilde{\lambda}. \quad (\text{A.9})$$

Therefore, $\frac{\partial \mathcal{L}(u, \lambda, m)}{\partial \lambda} = 0$ gives the state equation and $\frac{\partial \mathcal{L}(u, \lambda, m)}{\partial \tilde{u}}$ the adjoint-state equation. Additionally, $\frac{\partial \mathcal{L}(u, \tilde{\lambda}, m)}{\partial m} = \frac{\partial J}{\partial m}$. The optimization theory with equality constraints tells us that one Lagrange multiplier is associated with each scalar equation defining constraint. Here, one scalar adjoint state is associated with each scalar equation defining the mapping F . The three steps to compute the gradient are:

1. Build the Lagrangian \mathcal{L} .

$$\mathcal{L}(\tilde{u}, \tilde{\lambda}, m) = h(\tilde{u}, m) - \langle \tilde{\lambda}, F(\tilde{u}, m) \rangle.$$

2. Definition of adjoint state equation.

The adjoint state equation is defined by $\frac{\partial \mathcal{L}(u, \lambda, m)}{\partial \tilde{u}} = 0$ where the derivative is evaluated at (u, λ) .

$$\left(\frac{\partial F(u, m)}{\partial \tilde{u}} \right)^* \lambda = \frac{\partial h(u, m)}{\partial \tilde{u}} \quad (\text{A.10})$$

3. Computation of gradient of $J(m)$.

For this, compute the derivative of \mathcal{L} with respect to m

$$\frac{\partial J}{\partial m} = \frac{\partial \mathcal{L}(u, \lambda, m)}{\partial m} = \frac{\partial h(u, m)}{\partial m} - \langle \lambda, \frac{\partial F(u, m)}{\partial m} \rangle. \quad (\text{A.11})$$

Following the Lagrangian approach, we arrive at the same adjoint formulation of the gradient as in Eq. 3.89.

In the considered case, where the cost is the classical least-squares objective, which is only indirectly depending on m , the state is described by the acoustic wave equation and model parameters are chosen to be $m(x) := v_p^2(x)$, the gradient is given by

$$\frac{\partial J}{\partial m} = -\langle \lambda, \frac{\partial F(u, m)}{\partial m} \rangle = - \int_{\Omega} \int_0^T \Delta u \cdot \lambda \, dt \, dx. \quad (\text{A.12})$$

This agrees with the adjoint formulation for the acoustic wave equation derived by perturbation theory, as shown in Eq. 3.94.

Bibliography

- Afanasiev, M., Ermert, L., Staring, M., Trampert, J., and Fichtner, A. (2016). Full seismic waveform inversion of the African crust and Mantle-Initial Results. In EGU General Assembly Conference Abstracts, volume 18, page 4543.
- Aki, K., Christoffersson, A., and Husebye, E. S. (1977). Determination of the three-dimensional seismic structure of the lithosphere. Journal of Geophysical Research, 82(2):277–296.
- Amitt, E., Givoli, D., and Turkel, E. (2014). Time reversal for crack identification. Computational Mechanics, 54(2):443–459.
- Ammari, H., Bretin, E., Garnier, J., and Wahab, A. (2013). Time-reversal algorithms in viscoelastic media. European Journal of Applied Mathematics, 24(04):565–600.
- Baysal, E., Kosloff, D. D., and Sherwood, J. W. (1983). Reverse time migration. Geophysics, 48(11):1514–1524.
- Belanger, P., Cawley, P., Thompson, D. O., and Chimenti, D. E. (2008). Lamb wave tomography to evaluate the maximum depth of corrosion patches. In AIP Conference Proceedings, volume 975 of 1, pages 1290–1297.
- Bishop, C. M. (2006). Pattern Recognition and Machine Learning. Information science and statistics. Springer, New York.
- Bleistein, N., Cohen, J. K., and Stockwell, J. W. (2001). Mathematics of Multidimensional Seismic Imaging, Migration, and Inversion. Number v. 13 in Interdisciplinary applied mathematics. Springer, New York.
- Bletzinger, K.-U., Firl, M., Linhard, J., and Wüchner, R. (2010). Optimal shapes of mechanically motivated surfaces. Computer Methods in Applied Mechanics and Engineering, 199(5-8):324–333.
- Bletzinger, K.-U. and Maute, K. (1997). Towards generalized shape and topology optimization. Engineering Optimization, 29(1-4):201–216.
- Bletzinger, K.-U. and Ramm, E. (2014). Computational form finding and optimization. In Shell Structures for Architecture: Form Finding and Optimization, pages 45–56. Routledge.
- Bletzinger, K.-U., Wüchner, R., Daoud, F., and Camprubí, N. (2005). Computational methods for form finding and optimization of shells and membranes. Computer Methods in Applied Mechanics and Engineering, 194(30-33):3438–3452.

- Blitz, J. and Simpson, G. (1996). Ultrasonic Methods of Non-Destructive Testing. Non-destructive evaluation series. Chapman & Hall, London.
- Brooks, R. A. and Chiro, G. D. (1976). Principles of computer assisted tomography (CAT) in radiographic and radioisotopic imaging. Physics in Medicine and Biology, 21(5):689–732.
- Broyden, C. G. (1970). The Convergence of a Class of Double-rank Minimization Algorithms 1. General Considerations. IMA Journal of Applied Mathematics, 6(1):76–90.
- Bunks, C., Saleck, F. M., Zaleski, S., and Chavent, G. (1995). Multiscale seismic waveform inversion. GEOPHYSICS, 60(5):1457–1473.
- Burrascano, P., Callegari, S., Montisci, A., Ricci, M., and Versaci, M., editors (2015). Ultrasonic Nondestructive Evaluation Systems. Springer International Publishing, Cham.
- Buzug, T. M. (2008). Computed Tomography: From Photon Statistics to Modern Cone-Beam CT. Springer, Berlin.
- Cao, Y., Li, S., and Petzold, L. (2002). Adjoint sensitivity analysis for differential-algebraic equations: Algorithms and software. Journal of computational and applied mathematics, 149(1):171–191.
- Cao, Y., Li, S., Petzold, L., and Serban, R. (2003). Adjoint Sensitivity Analysis for Differential-Algebraic Equations: The Adjoint DAE System and Its Numerical Solution. SIAM Journal on Scientific Computing, 24(3):1076–1089.
- Carlson, N. and Johnson, J. (1992). Ultrasonic sensing of weld pool penetration. NDT & E International, 25(1):47.
- Chapman, C. H. (1987). The Radon transform and seismic tomography. In Nolet, G., editor, Seismic Tomography, pages 25–47. Springer Netherlands, Dordrecht.
- Chavent, G. (2009). Nonlinear Least Squares for Inverse Problems: Theoretical Foundations and Step-by-Step Guide for Applications. Scientific computation. Springer Verlag, Dordrecht ; New York.
- Chen, C., Li, Y., and Yuan, F.-G. (2013). Development of time-reversal method for impact source identification on plate structures. Shock and Vibration, 20(3):561–573.
- Chen, P., Jordan, T. H., and Zhao, L. (2007). Full three-dimensional tomography: A comparison between the scattering-integral and adjoint-wavefield methods. Geophysical Journal International, 170(1):175–181.
- Christensen, P. W. and Klarbring, A. (2009). An Introduction to Structural Optimization. Number 153 in Solid mechanics and its applications. Springer, Dordrecht.
- Claerbout, J. F. (1985). Imaging the Earth’s Interior. Blackwell Scientific Publications, Oxford [England] ; Boston.

- Conn, A. R., Scheinberg, K., and Vicente, L. N. (2009). Introduction to Derivative-Free Optimization. Number 8 in MPS-SIAM series on optimization. Society for Industrial and Applied Mathematics/Mathematical Programming Society, Philadelphia.
- Courant, R., Friedrichs, K., and Lewy, H. (1928). Über die partiellen Differenzengleichungen der mathematischen Physik. Mathematische Annalen, 100(1):32–74.
- Courboux, F., Virieux, J., Deschamps, A., Gibert, D., and Zollo, A. (1996). Source investigation of a small event using empirical Green’s functions and simulated annealing. Geophysical Journal International, 125(3):768–780.
- Curtis, A. (2004). Theory of model-based geophysical survey and experimental design: Part 1—Linear problems. The Leading Edge, 23(10):997–1004.
- Deneuve, A., Druault, P., Marchiano, R., and Sagaut, P. (2010). A coupled time-reversal/complex differentiation method for aeroacoustic sensitivity analysis: Towards a source detection procedure. Journal of Fluid Mechanics, 642:181.
- Dessa, J.-X. and Pascal, G. (2003). Combined traveltimes and frequency-domain seismic waveform inversion: A case study on multi-offset ultrasonic data. Geophysical Journal International, 154(1):117–133.
- Dhawan, A. P. (2011). Medical Image Analysis. Wiley-IEEE, Hoboken, N.J.
- Dimri, V. (1992). Deconvolution and Inverse Theory: Application to Geophysical Problems. Elsevier Science, Burlington.
- Dominguez, N. and Gibiat, V. (2010). Non-destructive imaging using the time domain topological energy method. Ultrasonics, 50(3):367–372.
- Dominguez, N., Gibiat, V., and Esquerre, Y. (2005). Time domain topological gradient and time reversal analogy: An inverse method for ultrasonic target detection. Wave Motion, 42(1):31–52.
- Drinkwater, B. W. and Wilcox, P. D. (2006). Ultrasonic arrays for non-destructive evaluation: A review. NDT & E International, 39(7):525–541.
- Duczek, S., Joulaiian, M., Düster, A., and Gabbert, U. (2013). Simulation of Lamb waves using the spectral cell method. In Proc. SPIE 8695, Health Monitoring of Structural and Biological Systems 2013, volume 86951U, San Diego, California, United States.
- Durrant, D. R. (1999). Numerical Methods for Wave Equations in Geophysical Fluid Dynamics. Springer, New York.
- Errico, R. M. (1997). What Is an Adjoint Model? Bulletin of the American Meteorological Society, 78(11):2577–2591.
- Etgen, J. T. and O’Brien, M. J. (2007). Computational methods for large-scale 3D acoustic finite-difference modeling: A tutorial. GEOPHYSICS, 72(5):SM223–SM230.

- Fichtner, A. (2011). Full Seismic Waveform Modelling and Inversion. Advances in Geophysical and Environmental Mechanics and Mathematics. Springer, Heidelberg.
- Fichtner, A., Kennett, B. L. N., Igel, H., and Bunge, H.-P. (2009). Full seismic waveform tomography for upper-mantle structure in the Australasian region using adjoint methods. Geophysical Journal International, 179(3):1703–1725.
- Fichtner, A., Trampert, J., Cupillard, P., Saygin, E., Taymaz, T., Capdeville, Y., and Villasenor, A. (2013). Multiscale full waveform inversion. Geophysical Journal International, 194(1):534–556.
- Fink, M. (1992). Time reversal of ultrasonic fields. I. Basic principles. IEEE transactions on ultrasonics, ferroelectrics, and frequency control, 39(5):555–566.
- Fink, M. (1997). Fink, M., "Time-reversal acoustics ," Physics Today, Vol. 50, No. 3, 34-40. Physics Today, 50(3):34–40.
- Fink, M. (1999). Time-Reversed Acoustics. Scientific American, 281(5):91–97.
- Fink, M., Cassereau, D., Derode, A., Prada, C., Roux, P., Tanter, M., Thomas, J.-L., and Wu, F. (2000). Time-reversed acoustics. Reports on Progress in Physics, 63(12):1933–1995.
- Fletcher, R. (2008). Practical Methods of Optimization. Wiley, Chichester.
- Gauger, N. R. (2002). Aerodynamic Shape Optimization. J.Aero.Soc.of India, 54(3):246–254.
- Giles, M. and Ulbrich, S. (2010a). Convergence of linearized and adjoint approximations for discontinuous solutions of conservation laws. Part 1: Linearized approximations and linearized output functionals. SIAM Journal on Numerical Analysis, 48(3):882–904.
- Giles, M. and Ulbrich, S. (2010b). Convergence of Linearized and Adjoint Approximations for Discontinuous Solutions of Conservation Laws. Part 2: Adjoint Approximations and Extensions. SIAM Journal on Numerical Analysis, 48(3):905–921.
- Giles, M. B., Duta, M. C., Müller, J.-D., and Pierce, N. A. (2003). Algorithm developments for discrete adjoint methods. AIAA journal, 41(2):198–205.
- Giles, M. B. and Pierce, N. A. (1997). Adjoint equations in CFD: Duality, boundary conditions and solution behaviour. AIAA journal, 97:1850.
- Giles, M. B. and Pierce, N. A. (2000). An introduction to the adjoint approach to design. Flow, turbulence and combustion, 65(3-4):393–415.
- Givoli, D. (2014). Time Reversal as a Computational Tool in Acoustics and Elastodynamics. Journal of Computational Acoustics, 22(03):1430001.
- Givoli, D. and Turkel, E. (2012). Time reversal with partial information for wave refocusing and scatterer identification. Computer Methods in Applied Mechanics and Engineering, 213-216:223–242.

- Griewank, A. (2012). Who Invented the Reverse Mode of Differentiation? Documenta Mathematica, Extra Volume ISMP, pages 389–400.
- Haber, E., Chung, M., and Herrmann, F. (2012). An Effective Method for Parameter Estimation with PDE Constraints with Multiple Right-Hand Sides. SIAM Journal on Optimization, 22(3):739–757.
- Hartmann, F. and Katz, C. (2002). Statik mit finiten Elementen. Springer, Berlin, Heidelberg.
- Hinze, M., editor (2009). Optimization with PDE Constraints. Number 23 in Mathematical modelling. Springer, Dordrecht.
- Hounsfield, G. N. (1973). Computerized transverse axial scanning (tomography): Part 1. Description of system. The British Journal of Radiology, 46(552):1016–1022.
- Husen, S. and Kissling, E. (2001). Local earthquake tomography between rays and waves: Fat ray tomography. Physics of the earth and Planetary Interiors, 123(2):127–147.
- Huthwaite, P. (2014). Evaluation of inversion approaches for guided wave thickness mapping. Proceedings of the Royal Society A: Mathematical, Physical and Engineering Sciences, 470(2166):20140063–20140063.
- Huthwaite, P. and Simonetti, F. (2011). High-resolution imaging without iteration: A fast and robust method for breast ultrasound tomography. The Journal of the Acoustical Society of America, 130(3):1721–1734.
- Huthwaite, P. and Simonetti, F. (2013). High-resolution guided wave tomography. Wave Motion, 50(5):979–993.
- Igel, H. (2016). Computational Seismology - a Practical Introduction. Oxford University Press, New York, NY, 1st edition.
- Joulaian, M., Duczek, S., Gabbert, U., and Düster, A. (2014). Finite and spectral cell method for wave propagation in heterogeneous materials. Computational Mechanics, 54(3):661–675.
- Karbhari, V. M. (2013). Non-Destructive Evaluation (NDE) of Polymer Matrix Composites: Techniques and Applications. Number 43 in Woodhead Publishing series in composites science and engineering. Woodhead Pub, Cambridge, UK ; Philadelphia, PA.
- Kocur, G. K. (2012). Time Reverse Modeling of Acoustic Emissions in Structural Concrete. PhD thesis, ETH Zürich.
- Kocur, G. K., Saenger, E. H., Grosse, C. U., and Vogel, T. (2015). Time reverse modeling of acoustic emissions in a reinforced concrete beam. Ultrasonics.
- Komatitsch, D. and Tromp, J. (2002). Spectral-element simulations of global seismic wave propagation-II. Three-dimensional models, oceans, rotation and self-gravitation. Geophysical Journal International, 150(1):303–318.

- Komatitsch, D. and Vilotte, J.-P. (1998). The spectral element method: An efficient tool to simulate the seismic response of 2D and 3D geological structures. Bulletin of the seismological society of America, 88(2):368–392.
- Krautkrämer, J. and Krautkrämer, H. (1983). Ultrasonic Testing of Materials. Springer Berlin Heidelberg, Berlin, Heidelberg.
- Krebs, J. R., Anderson, J. E., Hinkley, D., Neelamani, R., Lee, S., Baumstein, A., and Lacasse, M.-D. (2009). Fast full-wavefield seismic inversion using encoded sources. GEOPHYSICS, 74(6):WCC177–WCC188.
- Kremers, S., Fichtner, A., Brietzke, G. B., Igel, H., Larmat, C., Huang, L., and Käser, M. (2011). Exploring the potentials and limitations of the time-reversal imaging of finite seismic sources. Solid Earth, 2(1):95–105.
- Kumar, A., Jayakumar, T., Raj, B., and Ray, K. (2003). Characterization of solutionizing behavior in VT14 titanium alloy using ultrasonic velocity and attenuation measurements. Materials Science and Engineering: A, 360(1-2):58–64.
- Kunze, H. (2008). Iterative Rekonstruktion in der medizinischen Bildverarbeitung. Number 17 in Erlanger Berichte aus Informations- und Kommunikationstechnik. Shaker, Aachen.
- Larmat, C. S., Guyer, R. A., and Johnson, P. A. (2010). Time-reversal methods in geophysics. Phys. Today, 63(8):31–35.
- Leonard, K. R., Malyarenko, E. V., and Hinders, M. K. (2002). Ultrasonic Lamb wave tomography. Inverse problems, 18(6):1795.
- Leutenegger, T. and Dual, J. (2002). Detection of defects in cylindrical structures using a time reverse method and a finite-difference approach. Ultrasonics, 40(1-8):721–725.
- LeVeque, R. J. (2007). Finite Difference Methods for Ordinary and Partial Differential Equations: Steady-State and Time-Dependent Problems. Society for Industrial and Applied Mathematics, Philadelphia, PA.
- Liu, B.-d., Zeng, L., and Ji, D. J. (2008). Algebraic reconstruction technique class for linear scan CT of long object. In Proceedings of the 17th World Conference on Nondestructive Testing, Shanghai, China. Citeseer.
- Long, Q., Motamed, M., and Tempone, R. (2015). Fast Bayesian optimal experimental design for seismic source inversion. Computer Methods in Applied Mechanics and Engineering, 291:123–145.
- Loris, I., Nolet, G., Daubechies, I., and Dahlen, F. A. (2007). Tomographic inversion using l1-norm regularization of wavelet coefficients. Geophysical Journal International, 170(1):359–370.
- Mao, J., Wu, R.-S., and Wang, B. (2012). Multiscale full waveform inversion using GPU. In SEG Technical Program Expanded Abstracts, pages 1–7. Society of Exploration Geophysicists.

- Marchuk, G., Shutyaev, V., and Bocharov, G. (2005). Adjoint equations and analysis of complex systems: Application to virus infection modelling. Journal of Computational and Applied Mathematics, 184(1):177–204.
- Marchuk, G. I. (1995). Adjoint Equations and Analysis of Complex Systems. Springer, Dordrecht.
- Martens, J. (2010). Deep learning via Hessian-free optimization. In Proceedings of the 27th International Conference on Machine Learning (ICML-10), pages 735–742.
- Martiartu, N. K., Boehm, C., Vinard, N., Balic, I. J., and Fichtner, A. (2017). Optimal experimental design to position transducers in ultrasound breast imaging. In SPIE Medical Imaging, pages 101390M–101390M. International Society for Optics and Photonics.
- Meier, U., Curtis, A., and Trampert, J. (2007). Global crustal thickness from neural network inversion of surface wave data. Geophysical Journal International, 169(2):706–722.
- Meyendorf, N. G. H., Nagy, P. B., Rokhlin, S. I., Hull, R., Osgood, R. M., Parisi, J., and Warlimont, H., editors (2004). Nondestructive Materials Characterization, volume 67 of Springer Series in Materials Science. Springer, Berlin, Heidelberg.
- Moczo, P., Bystricky, E., Kristek, J., Carcione, J. M., and Bouchon, M. (1997). Hybrid modeling of P-SV seismic motion at inhomogeneous viscoelastic topographic structures. Bulletin of the seismological Society of America, 87(5):1305–1323.
- Moczo, P., Kristek, J., and Gális, M. (2014). The Finite-Difference Modelling of Earthquake Motions: Waves and Ruptures. Cambridge University Press, New York.
- Moczo, P., Kristek, J., Galis, M., Pazak, P., and Balazovjeh, M. (2007). The finite-difference and finite-element modeling of seismic wave propagation and earthquake motion. Acta physica slovacica, 57(2).
- Nakahata, K., Kawamura, G., Yano, T., and Hirose, S. (2015). Three-dimensional numerical modeling of ultrasonic wave propagation in concrete and its experimental validation. Construction and Building Materials, 78:217–223.
- Newman III, J. C., Taylor III, A. C., Barnwell, R. W., Newman, P. A., and Hou, G. J.-W. (1999). Overview of Sensitivity Analysis and Shape Optimization for Complex Aerodynamic Configurations. Journal of Aircraft, 36(1):87–96.
- Nocedal, J. and Wright, S. J. (1999). Numerical Optimization. Springer series in operations research. Springer, New York.
- Ohtsu, M. (2016). Innovative AE and NDT Techniques for On-Site Measurement of Concrete and Masonry Structures. Springer Berlin Heidelberg, New York, NY.
- Oliveira, E. F., Melo, S. B., Dantas, C. C., Vasconcelos, D. A., and Cadiz, F. (2011). Comparison among tomographic reconstruction algorithms with a limited data. In International Nuclear Atlantic Conference-INAC 2011.

- Othmer, C. (2014). Adjoint methods for car aerodynamics. Journal of Mathematics in Industry, 4(1):1–23.
- Park, H. W., Sohn, H., Law, K. H., and Farrar, C. R. (2007). Time reversal active sensing for health monitoring of a composite plate. Journal of Sound and Vibration, 302(1-2):50–66.
- Pearlmutter, B. A. (1994). Fast Exact Multiplication by the Hessian. Neural Computation, 6(1):147–160.
- Peter, D., Komatitsch, D., Luo, Y., Martin, R., Le Goff, N., Casarotti, E., Le Loher, P., Magnoni, F., Liu, Q., Blitz, C., Nissen-Meyer, T., Basini, P., and Tromp, J. (2011). Forward and adjoint simulations of seismic wave propagation on fully unstructured hexahedral meshes: SPECFEM3D Version 2.0 ‘Sesame’. Geophysical Journal International, 186(2):721–739.
- Pironneau, O. (1974). On optimum design in fluid mechanics. Journal of Fluid Mechanics, 64(01):97–110.
- Plessix, R.-E. (2006). A review of the adjoint-state method for computing the gradient of a functional with geophysical applications. Geophysical Journal International, 167(2):495–503.
- Polak, E. (1997). Optimization: Algorithms and Consistent Approximations. Number 124 in Applied mathematical sciences. Springer, New York.
- Prassianakis, I. and Prassianakis, N. (2004). Ultrasonic testing of non-metallic materials: Concrete and marble. Theoretical and Applied Fracture Mechanics, 42(2):191–198.
- Pratt, R. G., Shin, C., and Hick, G. J. (1998). Gauss–Newton and full Newton methods in frequency–space seismic waveform inversion. Geophysical Journal International, 133(2):341–362.
- Quarteroni, A., Sacco, R., and Saleri, F. (2000). Numerical Mathematics. Number 37 in Texts in applied mathematics. Springer, New York.
- Rao, J., Ratassepp, M., and Fan, Z. (2016a). Guided Wave Tomography Based on Full Waveform Inversion. IEEE transactions on ultrasonics, ferroelectrics, and frequency control, 63(5):737–745.
- Rao, J., Ratassepp, M., and Fan, Z. (2016b). Limited-view ultrasonic guided wave tomography using an adaptive regularization method. Journal of Applied Physics, 120(19):194902.
- Rao, J., Ratassepp, M., and Fan, Z. (2017). Investigation of the reconstruction accuracy of guided wave tomography using full waveform inversion. Journal of Sound and Vibration, 400:317–328.
- Ravaut, C., Operto, S., Improta, L., Virieux, J., Herrero, A., and Dell’Aversana, P. (2004). Multiscale imaging of complex structures from multifold wide-aperture seismic data by frequency-domain full-waveform tomography: Application to a thrust belt. Geophysical Journal International, 159(3):1032–1056.
- Rumelhart, D. E., Hinton, G. E., and Williams, R. J. (1986). Learning representations by back-propagating errors. Nature, 323(6088):533–536.

- Sandhu, G. Y., Li, C., Roy, O., Schmidt, S., and Duric, N. (2015). Frequency domain ultrasound waveform tomography: Breast imaging using a ring transducer. Physics in Medicine and Biology, 60(14):5381–5398.
- Sandhu, G. Y., West, E., Li, C., Roy, O., and Duric, N. (2017). 3D frequency-domain ultrasound waveform tomography breast imaging. page 1013909.
- Sandhu, G. Y. S., Li, C., Roy, O., West, E., Montgomery, K., Boone, M., and Duric, N. (2016). Frequency-domain ultrasound waveform tomography breast attenuation imaging. page 97900C.
- Sandoz, J. L., Benoit, Y., and Demay, L. (2000). Wood testing using acousto-ultrasonic. In 12th International Symposium on Nondestructive Testing of Wood, pages 97–104.
- Schiebold, K. (2015). Zerstörungsfreie Werkstoffprüfung - Ultraschallprüfung: mit 100 Tabellen. Springer Vieweg, Berlin, 1. aufl edition.
- Schiemenz, A. and Igel, H. (2013). Accelerated 3-D full-waveform inversion using simultaneously encoded sources in the time domain: Application to Valhall ocean-bottom cable data. Geophysical Journal International, 195(3):1970–1988.
- Schraudolph, N. N. (2002). Fast Curvature Matrix-Vector Products for Second-Order Gradient Descent. Neural Computation, 14(7):1723–1738.
- Seidl, R. and Rank, E. (2016). Iterative time reversal based flaw identification. Computers & Mathematics with Applications, 72(4):879–892.
- Taffe, A., Wiggenhauser, H., and Raupach, M. (2008). Validierung zerstörungsfreier Prüfverfahren im Bauwesen. Beton- und Stahlbetonbau, 103(12):828–836.
- Tarantola, A. (1984). Inversion of seismic reflection data in the acoustic approximation. GEOPHYSICS, 49(8):1259–1266.
- Tromp, J., Komattisch, D., and Liu, Q. (2008). Spectral-element and adjoint methods in seismology. Communications in Computational Physics, 3(1):1–32.
- Tromp, J., Tape, C., and Liu, Q. (2004). Seismic tomography, adjoint methods, time reversal and banana-doughnut kernels: Seismic tomography, adjoint methods, time reversal and banana-doughnut kernels. Geophysical Journal International, 160(1):195–216.
- Ulbrich, M. and Ulbrich, S. (2012). Nichtlineare Optimierung. Springer Basel, Basel.
- van der Hilst, R. D. and de Hoop, M. V. (2005). Banana-doughnut kernels and mantle tomography. Geophysical Journal International, 163(3):956–961.
- van Laarhoven, P. J. M. and Aarts, E. H. L. (1992). Simulated Annealing: Theory and Applications. Number 37 in Mathematics and its applications. Kluwer, Dordrecht, reprint edition.

- Vigh, D. and Starr, E. W. (2008). Comparisons for waveform inversion, time domain or frequency domain? In SEG Technical Program Expanded Abstracts, pages 1890–1894. Society of Exploration Geophysicists.
- Virieux, J. and Operto, S. (2009). An overview of full-waveform inversion in exploration geophysics. GEOPHYSICS, 74(6):WCC1–WCC26.
- VonNeumann, J. and Richtmyer, R. D. (1950). A Method for the Numerical Calculation of Hydrodynamic Shocks. Journal of Applied Physics, 21(3):232–237.
- Warner, M., Stekl, I., and Umpleby, A. (2008). 3D wavefield tomography: Synthetic and field data examples. In SEG Technical Program Expanded Abstracts 2008, pages 3330–3334. Society of Exploration Geophysicists.
- Werner, D. (2007). Funktionalanalysis. Springer-Lehrbuch. Springer Berlin Heidelberg.
- Wolfe, P. (1982). Checking the calculation of gradients. ACM Transactions on Mathematical Software (TOMS), 8(4):337–343.
- Xu, B. and Giurgiutiu, V. (2007). Single Mode Tuning Effects on Lamb Wave Time Reversal with Piezoelectric Wafer Active Sensors for Structural Health Monitoring. Journal of Nondestructive Evaluation, 26(2-4):123–134.
- Yedlin, M. J. and Van Vorst, D. (2010). Tutorial on the continuous and discrete adjoint state method and basic implementation.
- Yoon, K., Marfurt, K. J., and Starr, W. (2004). Challenges in reverse-time migration. In SEG Technical Program Expanded Abstracts, pages 1057–1060. Society of Exploration Geophysicists.
- Zelenyak, A.-M., Oster, R., Mosch, M., Jahnke, P., and Sause, M. G. (2016). Numerical Modeling of Ultrasonic Inspection in Fiber Reinforced Materials with Explicit Microstructure. In Proc. 19th World Conference on Non-Destructive Testing, Munich, DGZfP.
- Zhang, Y. and Sun, J. (2009). Practical issues of reverse time migration: True amplitude gathers, noise removal and harmonic-source encoding. In 70th EAGE Conference, pages 204–204. Society of Exploration Geophysicists.